PISTON

Journal of Technical Engineering

Vol. 9
No. 1
July 2025
ISSN 2541-3511

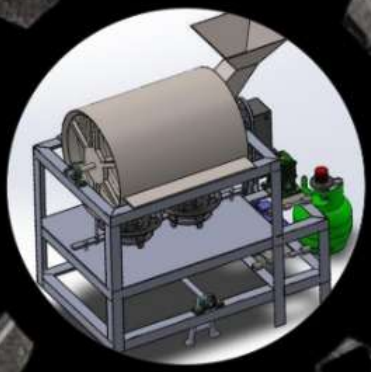

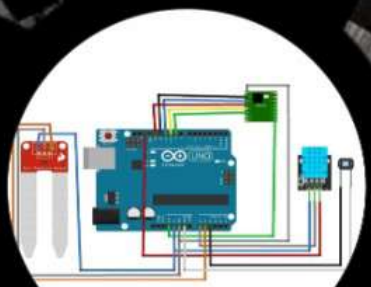

Program Studi Teknik Mesin
Fakultas Teknik
Universitas Pamulang

EDITORIAL BOARD

Piston: Journal of Technical Engineering
Universitas Pamulang
Volume 9, Number 1
July 2025

The editorial board accepts original manuscripts from academics, researchers, and practitioners that have not been previously published. A blind review process is used to determine the suitability of manuscripts for publication. Submission guidelines are provided in this journal. Submitted manuscripts must include a soft copy..

Editorial Office Address
Mechanical Engineering Department, Faculty of Engineering, Universitas Pamulang
Jl. Surya Kencana No.1, Pamulang – South Tangerang, Indonesia
Phone: (+6221) 7412566.
E-mail: piston@unpam.ac.id

PISTON:
Journal of Technical Engineering:

SCOPE OF THE JOURNAL

Piston Journal of the Mechanical Engineering Study Program at Pamulang University accepts manuscripts on a wide range of topics in the field of mechanical engineering, including but not limited to:

1. Energy conversion
2. Materials
3. Manufacturing
4. Mechanical design and construction
5. Other areas related to mechanical engineering.

MANUSCRIPT FORMAT

Manuscripts submitted to this journal—whether conceptual studies or empirical research—should follow the structure outlined below:

(1) **Author(s)**: Full name(s) accompanied by institutional affiliation(s).
(2) **Abstract**: Presented in both Indonesian and English, along with keywords. The abstract should not exceed 300 words.
(3) **Introduction**.
(4) **Main content**.
- For conceptual articles: includes core discussion and analysis.
- For research-based articles: includes:
  - Research methodology, and
  - Result and discussion.
- Figures, tables, and mathematical equations must be sequentially numbered and properly captioned.

(5) Conclusion
(6) Recommendations (if applicable)
(7) Acknowledgments (if applicable).
(8) **References**: A minimum of 10 references is required, with preference given to recent sources.

Manuscript Formatting Guidelines

1. Manuscripts must be submitted in .docx or .doc format.
2. Font: Times New Roman.
3. Single-column layout.
4. Line spacing: single. Paper size: A4.
5. Length: Minimum 5 pages, maximum 10 pages.
6. Margins: 1 cm on all sides (top, bottom, left, right).
7. Image resolution: Minimum 300 dpi, accepted formats include PNG, JPEG, and BMP.
8. References should follow the IOP referencing style

All submitted manuscripts will be reviewed by peer reviewers (Mitra Bestari) to assess their relevance to the journal's scope and the quality of the content. Accepted papers will be published in the *Piston Journal* of Universitas Pamulang.

PISTON:
Journal of Technical Engineering:

TABLE OF CONTENTS

PISTON:
Journal of Technical Engineering:

FOREWORD

Alhamdulillahirabbil 'Alamin, all praise and gratitude we extend to Allah SWT for His blessings and guidance, through which the *Journal of Technical Engineering*, Vol. 9, No. 1, July 2025, has been successfully published on schedule.

In this edition of the *Journal of Technical Engineering*, the published articles cover a wide range of topics in mechanical and applied engineering. These include research on the mechanical properties of ST 37 manufactured by Gas Tungsten Arc Welding using cannibal consumable manufacturing filler, the characteristics of aluminium 7075 tool profiles for HDPE and PP welding against tensile and bending, and the design of handoff communication sequence architecture in LoRa networks. Also featured is a systematic review on the acoustic performance of nanocellulose-modified natural fibers for sound insulation and absorption applications, a web-based navigation control system for Lake Toba cleaning using NodeMCU ESP8266 and pulse width modulation (PWM), the design of a helical type steam generator for an experimental power reactor – helium side, and a system circuit analysis of a solar panel chicken egg incubator.

We encourage continued participation from researchers, lecturers, academics, and practitioners to contribute to this journal, ensuring its consistent publication according to the established schedule. Such contributions are vital for enhancing the quality and diversity of topics in accordance with the scope of mechanical engineering.

It is our hope that this journal provides valuable insights and contributes meaningfully to the advancement of science and technology, while also serving as a reference for national development efforts.

Finally, as no work is ever without flaws, we sincerely apologize for any shortcomings. Constructive feedback and suggestions are highly welcomed for the continuous improvement of this journal.

Pamulang, July 2025

Editorial Board

PISTON:
Journal of Technical Engineering:

AUTHOR INDEX

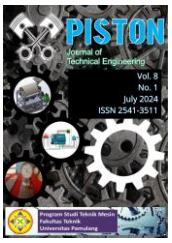

M

Marojahan Mula Timbul Sigiro

Melbi Mahardika

Meifal Rusli

Muchlisinalahuddin

Muhammad Nur Rochim

Muhammad Sibro Malisi

Mohammad Subekti

N

Nur Rohmat

P

Pandapotan Siagian

Prasetyo

R

Ripandy Saragih

Riswanda

Romaito Silaen

S

Sari Muthia Silalahi

Sulanjari

Sunny Ineza Putri

Syahrul Dwi Nugraha

T

Tb. Moch Mario Al-Qashtalani

PISTON
Journal of Technical Engineering:

Mechanical Properties of ST 37 Manufactured by Gas Tungsten Arc Welding using Cannibal Consumable Manufacturing Filler

Albert Daniel Saragih[1,a)], Riswanda[1], Prasetyo[1], Syahrul Dwi Nugraha[1], Tb. Moch Mario Al-Qashtalani[1]

[1]*Mechanical Engineering Department, Bandung State Polytechnic, Jl. Gegerkalong Hilir, Ds. Ciwaruga, Kotak Pos 1234, Bandung 40559, Indonesia*

E-mail: [a)] albertdanielsrgh@polban.ac.id

Received: July 01, 2024 *Revision: July 05, 2025* *Accepted: July 28, 2025*

Abstract: In this paper, the macrostructure and mechanical properties of medium carbon steel with cannibal consumable filler by using the GTAW process have been investigated. The medium carbon steel (ST 37) plates with dimensions of 300 × 250 ×3 mm were used for welding and 2.5 mm of thickness for the filler. For welding parameters, current of 80 A was chosen and observed over the welded specimen. Welding was performed with single Vgroove butt Joint design, 30° bevel angle. Preparation of samples was done according to standard. To explore the optimum welding specimen, both tensile and bending tests were carried out. The result of the welding process with the current of 80A shows that the face part tends to be more embossed and the root part looks less embossed, there are parts that lack penetration. This causes a lack of weld strength due to incomplete penetration of the root part. The face section produces maximum and strong results, while at the root there are cracks that are almost broken. This is due to lack of fusion because the current is too small resulting in differences in weld strength between the face and root, which affects the bending test results. In the tensile test results, a fracture occurred in the weld metal in the form of a brittle fracture. This is caused by a lack of fusion and very minimal penetration of the filler metal into the weld groove. Based on the macro test analysis carried out, minimal root penetration or no penetration occurs, while the weld seam accumulates on the face. Based upon the present study it is not recommended that 80 A of welding current when GTAW process using canibal consumable filler. The current of 80A may need to improve to produce good welding.

Keywords: Cannibal, Consumable, Filler, GTAW.

Abstrak: *Dalam penelitian ini, struktur makro dan sifat mekanik baja karbon sedang dengan penggunaan cannibal filler habis pakai melalui proses GTAW telah diteliti. Pelat baja karbon sedang (ST 37) dengan dimensi 300 × 250 × 3 mm digunakan untuk pengelasan dan filler dengan ketebalan 2,5 mm. Parameter pengelasan menggunakan arus sebesar 80 A yang diamati pada spesimen las. Proses pengelasan dilakukan dengan desain sambungan butt V tunggal dengan sudut bevel 30°. Persiapan spesimen dilakukan sesuai standar. Untuk mengeksplorasi spesimen las yang optimal, dilakukan uji tarik dan uji tekuk. Hasil dari proses pengelasan dengan arus 80 A menunjukkan bahwa bagian permukaan las cenderung lebih menonjol, sedangkan bagian akar terlihat kurang menonjol dan terdapat bagian yang mengalami kurang penetrasi. Hal ini menyebabkan kekuatan las menjadi rendah akibat tidak sempurnanya penetrasi pada bagian akar. Bagian permukaan menghasilkan hasil maksimal dan kuat, sementara pada akar terdapat retakan yang hampir patah. Hal ini disebabkan oleh kurangnya fusi karena arus yang terlalu kecil, sehingga terjadi perbedaan kekuatan las antara bagian permukaan dan akar, yang memengaruhi hasil uji tekuk. Pada hasil uji tarik, terjadi patahan pada logam las dalam bentuk patah getas. Hal ini disebabkan oleh kurangnya fusi dan sangat minimnya penetrasi logam pengisi ke dalam alur las. Berdasarkan analisis uji makro yang dilakukan, ditemukan penetrasi akar yang minimal bahkan tidak ada, sementara logam las menumpuk pada permukaan. Berdasarkan penelitian ini, tidak disarankan menggunakan arus 80 A dalam proses GTAW dengan cannibal filler habis pakai. Arus 80 A perlu ditingkatkan untuk menghasilkan kualitas pengelasan yang baik.*

Kata kunci: *Kanibal, Habis Pakai, Filler, GTAW.*

INTRODUCTION

Welding is the fabrication process of joining materials by heating to melt and allow them to cool causing fusion. Fusion welding is a joining process that uses fusion of the base metal to make the weld. The three major types of fusion welding processes are gas welding, arc welding and high-energy beam welding [1]. The Gas tungsten arc welding (GTAW) is a type of arc welding that uses a tungsten electrode that does not melt and what does melt is a filler. The GTAW method uses a shielding gas which functions to protect the liquid metal during the welding process so that it is not oxidized by oxygen in the surrounding environment. The shielding gas used is argon, helium or a mixture of the two gases [2]. The GTAW is a widely used joining technique due to its process more flexible, low welding cost, high welding quality and provides a sustainable environment by low energy consumption [3], [4].

The GTAW possible to join metals with or without filler metal. The welding arc from the tungsten electrode will melt the two base metals and unite them. However, to make the weld stronger and avoid cracking, use filler metal. Several cases in the field involve using fillers that are similar to the workpiece to be welded, or are referred to as cannibal consumables. The filler was made from the same or similar material as the material being welded and separated from the welding torch [5], [6]. Tarmizi et.al [7] investigated welding combination between GTAW and SMAW. The filler metal used in the GTAW process is ER80S-Ni_2. S. Senthilkumar et.al [8] observed the non-consumable tungsten electrode fused by high heat energy supplied via an electrical source and arc produced between the metal surfaces is melted and joined together through a filler rod. To the authors' best of knowledge, rarely discussion regarding testing this method to ensure that the cannibal consumable method can be used properly. Therefore, this study is designated to fabricate and analyze the cannibal consumable on tensile and bending properties of ST37 using GTAW.

METHODS

In this study, the low carbon steel of ST 37 with dimensions of 300×125× 3mm were used for welding specimen and 2.5 mm thickness for filler. Cutting of samples was performed by a hydraulic cutting machine and edge preparation was done by a grinding machine. The welding parameters were selected based on the first trials and the parameters were identified based on previous study as listed in Table 1 [8], [9]. Welding was performed with single Vgroove butt Joint design, 30° bevel angle. Preparation of samples was done according to ISO 2553:2019 [10] standard and also, according to the thickness of carbon steel, as show in Fig. 1 (left).

Table 1. Welding parameters of GTAW with welding consumable of ST 37

Parameters	Current (A)	Voltage	Welding speed	Position	Shielding gas	Polarity	Filler
Sample	80	12.3	6.11 mm/s	1G	Argon	DCEP	ST 37

Figure 1. Butt-weld joint preparation with 30° of bevel angle (left), The ARL optical emission spectrometer machine (right)

The ARL optical emission spectrometer (Fig. 1(right)) was used to determine the element composition of the metals. Tensile testing is carried out in the transverse direction. The ASTM E8M was used for the reference standard for making tensile testing specimens [11]. The ductility and strength of welded connection were analyze by using bend test. The ASTM E290-14 was used for the reference standard for making bending testing specimens [12]. The macrostructure of the sample in different welding zone was examined by optical microscope (Nikon Eclipse E600 Fluorescence Microscope)). Macro testing includes several steps, namely mounting, grinding, polishing, etching, and analysis using an optical microscope according to the ASTM E407 standard [13].

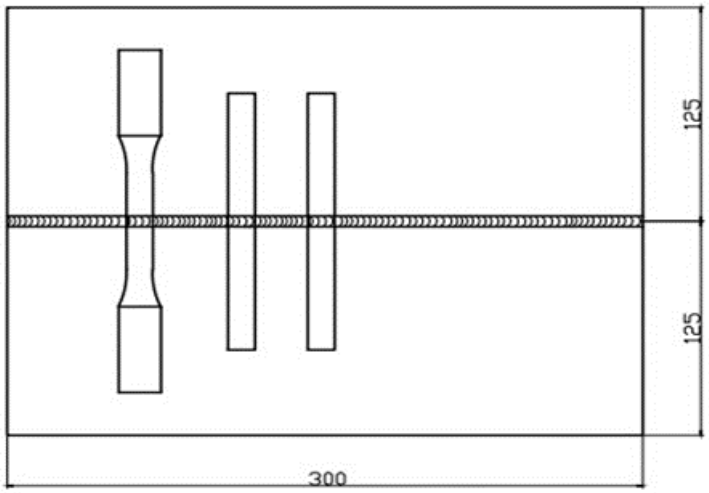

Figure 2. Specimen test lay-out of tensile and bend test

RESULT AND DISCUSSION

Based on the test results on the ARL optical emission spectrometer, the elemental composition contained in the ST37 steel material is shown in table 2. ST 37 is classified as medium carbon steel because it has a carbon content of 0.165. Carbon equivalent (CE) formulae are used to predict susceptibility to Hydrogen Induced Cracking (HIC). In general, the higher the value of CE, the more susceptible the steel is to HIC. Unfortunately, there is not a single CE formula that can be used for all steels. The International Institute of Welding (IIW) CE formula, CE_{IIW}, is the one that is most widely used because it can be generally applied to most plain-carbon and C–Mn steels [14].

$$CE = C + \frac{Mn}{6} + \frac{Cr + Mo + V}{5} + (Ni + Cu)/15 \qquad Eq.1$$

Based on equation 1, the result is 0.42. So from the calculation results it is concluded that ST 37 is a metal that has good weldability properties. If the calculation results exceed 0.45 then the metal does not have weldable properties which results in poor weld results.

Table 2. The elemental composition of ST 37

Elements	Percentage (%)
Carbon (C)	0,165
Silicon (Si)	0,253
Sulfur (S)	0,011
Phosphorus (P)	0,020
Manganese (Mn)	0,564
Nickel (Ni)	0,04
Chromium (Cr)	0,62
Molybdenum (Mo)	0,016
Vanadium (V)	0,004
Copper (Cu)	0,053
Wolfram/ Tungsen (W)	0,004
Titanium (Ti)	0,002
Tin (Sn)	0,005
Aluminium (Al)	0,001
Plumbun/Lead (Pb)	0,0015
Antimony (Sb)	0,002
Niobium (Nb)	0,001
Zirconium (Zr)	0,000
Zinc (Zn)	0,048
Ferro / Iron (Fe)	98,193

After cleaning the welding specimen, the weld results can be seen visually to observe the quality of the weld results. The result of the welding process (Fig. 3) with the current of 80A shows that the face part tends to be more embossed and the root part looks less embossed, there are parts that lack penetration. This causes a lack of weld strength due to incomplete penetration of the root part [15].

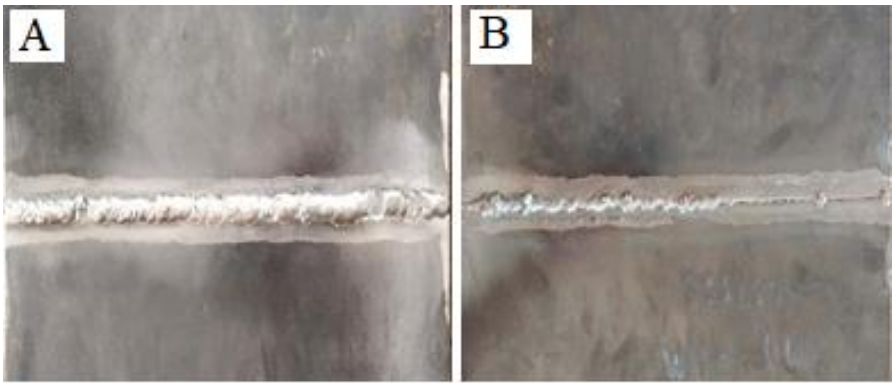

Figure 3. Weld bead of GTAW on ST 37 (a) Face (b) Root

Fig. 4 shows the bending test result on face and root. Bending test results shows differences in welding results between the face and root sections. The face section produces maximum and strong results, while at the root there are cracks that are almost broken. This is due to lack of fusion because the current is too small resulting in differences in weld strength between the face and root, which affects the bending test results [16]. The bending test results on the weld root show that the results are consistent with those on the weld bead that lack of fusion that effect for this case.

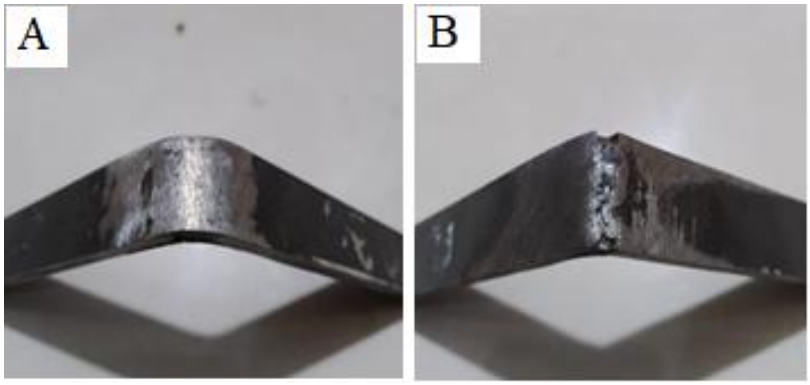

Figure 4. Test result for bending of (a) face (b) root

Table 3. Test results for tensile strength of specimen

Current	Thickness	Width	Surface Area	Length	UTS	YS	Elongation
80 A	3.04 mm	12 mm	36 mm^2	50 mm	316 N	285	2%

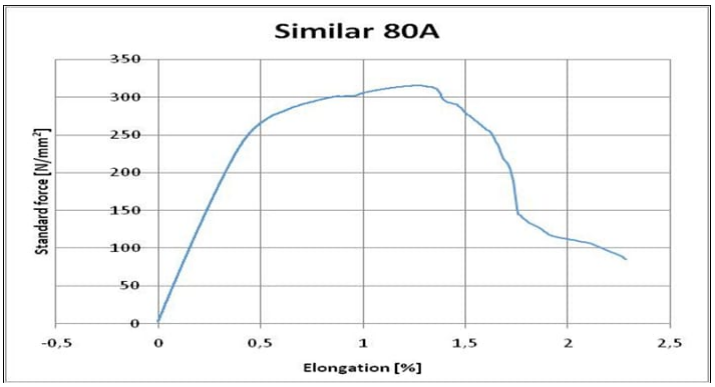

Figure 5. Stress-strain curve of GTAW with welding consumable of ST 37

Figure 6. Fractured photographs of tensile specimen of GTAW with welding consumable of ST 37

The detailed summary of the tensile test data (ultimate tensile strength, yield strength, and elongation is shown in Table 3. The characteristic stress-strain diagram is showed in Fig.5. Figure 6 shows the position of the

fracture that occurred in the tensile test results, a fracture occurred in the weld metal in the form of a brittle fracture. This is caused by a lack of fusion and very minimal penetration of the filler metal into the weld groove.

The macrostructure of the welded specimen is shown in Fig. 7 with the marking of each area (BM (Base Metal, HAZ (Heat Affected Zone) and WM (Weld Metal)). Based on the macro test analysis carried out, minimal root penetration or no penetration occurs, while the weld seam accumulates on the face as same as shown in Fig 3b and 4b. The failure that occurred in all specimens was britlle, indicating that the material was still capable of withstanding continuous loads before experiencing significant due to rapid cooling after welding [17].

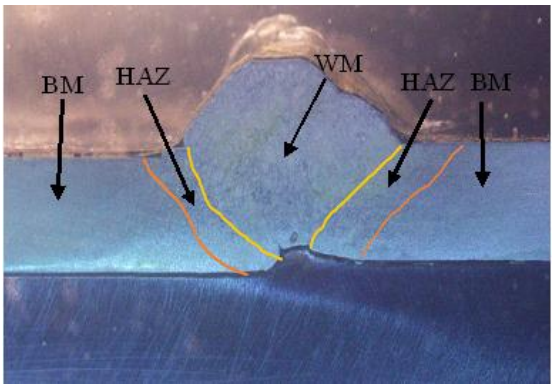

Figure 7. Macrostructure of a weld showing the marked regions: BM (Base Metal), HAZ (Heat-Affected Zone), and WM (Weld Metal)

CONCLUSIONS

The following are the main conclusions deduced from the present study:

1. Based on the calculation of Carbon Equivalent the specimen ST 37 was 0.42 which is good weldability properties. If the calculation results exceed 0.45 then the metal does not have weldable properties which results in poor weld results.
2. The result of the welding process with the current of 80A shows that the face part tends to be more embossed and the root part looks less embossed, there are parts that lack penetration. This causes a lack of weld strength due to incomplete penetration of the root part.
3. The face section produces maximum and strong results, while at the root there are cracks that are almost broken. This is due to lack of fusion because the current is too small resulting in differences in weld strength between the face and root, which affects the bending test results.
4. In the tensile test results, a fracture occurred in the weld metal in the form of a brittle fracture. This is caused by a lack of fusion and very minimal penetration of the filler metal into the weld groove.
5. Based on the macro test analysis carried out, minimal root penetration or no penetration occurs, while the weld seam accumulates on the face.

Based upon the present study it is not recommended that 80 A of welding current when GTAW process using canibal consumable filler. The current of 80A may need to improve to produce good welding.

ACKNOWLEDGEMENT

We would like to thank P3M of Bandung State Polytechnic, Bandung, Indonesia, for the funding research and permitting us to access the laboratories in the Mechanical Engineering Department.

REFERENCES

[1] S. Kou, *Welding Metallurgy*, 2nd ed. Hoboken: John Wiley & Sons, Inc., 2002. doi: 10.1002/0471434027.
[2] *Kobelco Welding Handbook*, 2020 Edition. Tokyo, Japan: Kobelco, 2020.
[3] J. Li, P. Zhou, H. Shi, and L. Wang, "Influence of filler metal on microstructure and properties of titanium/copper weld joint by GTAW weldments," *Mater. Sci. Eng. A*, vol. 833, p. 142508, 2022, doi: 10.1016/j.msea.2021.142508.
[4] H. Dong, X. Hao, and D. Deng, "Effect of Welding Heat Input on Microstructure and Mechanical Properties of HSLA Steel Joint," *Metallogr. Microstruct. Anal.*, vol. 3, no. 2, pp. 138–146, 2014, doi: 10.1007/s13632-014-0130-z.
[5] Riswanda, A. D. Saragih, H. Kadir, and W. A. Irawan, "The Effect of GTAW Process Parameters for Dissimilar

Metals Steel Armour and ASS 304L Using ER316L Filler on Mechanical Properties," in *Proceedings of the 4th International Conference on Experimental and Computational Mechanics in Engineering*, Springer Nature Singapore, 2024. doi: 10.1007/978-981-99-7495-5_64.

[6] Widharto, *Welding Inspection*, Edisi Asli. Jakarta, Indonesia: Mitra Wacana Media, 2013.

[7] Tarmizi, N. A. Hananda, and Irfan, "The Effect of Heat Input on Welding Combination of GTAW and SMAW SA537 Material on Mechanical Properties and Microstructure," *Kapal J. Ilmu Pengetah. dan Teknol. Kelaut.*, vol. 19, no. 2, pp. 56–63, Jun. 2022, doi: 10.14710/kapal.v19i2.45028.

[8] S. Senthilkumar, S. Manivannan, R. Venkatesh, and M. Karthikeyan, "Influence of heat input on the mechanical characteristics, corrosion and microstructure of ASTM A36 steel welded by GTAW technique," *Heliyon*, vol. 9, no. 9, Sep. 2023, doi: 10.1016/j.heliyon.2023.e19708.

[9] J. Luijan, P. Surin, and K. Eidhed, "Investigation of ER308L and ER309L filler wires on dissimilar metals between carbon steel and 3CR12 ferritic stainless steel by GTAW through boiler fabrication in a sugar factory," *Mater. Res. Express*, vol. 10, no. 12, p. 126501, 2023, doi: 10.1088/2053-1591/ad0eaa.

[10] I. O. for Standardization, "ISO 2553:2019, Welding and allied processes — Symbolic representation on drawings — Welded joints," *ISO Standard*. ISO, 2019. [Online]. Available: https://www.iso.org/standard/71976.html

[11] A. International, "ASTM E8/E8M-09: Standard Test Methods for Tension Testing of Metallic Materials," *ASTM Standard*. ASTM International, 2009. [Online]. Available: https://www.astm.org/e0008_e0008m-09.html

[12] A. International, "ASTM E290-14: Standard Test Methods for Bend Testing of Material for Ductility," *ASTM Standard*. ASTM International, 2014. [Online]. Available: https://www.astm.org/e0290-14.html

[13] A. International, "ASTM E407-99: Standard Practice for Microetching Metals and Alloys," *ASTM Standard*. ASTM International, pp. 1–21, 1999. [Online]. Available: https://www.astm.org/e0407-99.html

[14] J. C. Lippold, *Welding Metallurgy and Weldability*, 1st ed. Hoboken, NJ: John Wiley & Sons, Inc., 2014. doi: 10.1002/9781118960332.

[15] N. Yurioka and H. Suzuki, "Determination of the Required Preheating Temperature in Steel Welding," *Weld. J.*, vol. 62, no. 6, pp. 147s-154s.

[16] AWS, "AWS D1.1: Structural Welding Code – Steel," *AWS Standard*. American National Standard, Florida, 2020.

[17] A. International, "Atlas of Microstructures of Industrial Alloys," in *Metals Handbook*, vol. 7, 8th Edition, Ed., Ohio: American Society for Metals, 1972, pp. 139–140.

PISTON
Journal of Technical Engineering:

Characteristics of Aluminium 7075 Tool Profile for HDPE and PP Welding Against Tensile and Bending

Muhammad Sibro Malisi[1,a)], Febri Budi Darsono[1], Kriswanto[1], Abu Faqih Alkafi[1], Muhammad Nur Rochim[1], Fahmi Irsad Masruhan[1]

[1]*Department of Mechanical Engineering, Universitas Negeri Semarang, Sekaran, Gunung Pati, Semarang 50299, Indonesia*

E-mail: [a)] muhammadsibromalisi213@students.unnes.ac.id

Received: July 05, 2025 *Revision: July 08, 2025* *Accepted: July 28, 2025*

Abstract: The increasing demand for lightweight materials in the automotive industry has led to the replacement of metal vehicle components with polymers such as High-Density Polyethylene (HDPE) and Polypropylene (PP) to support sustainable development and emission reduction. However, welding dissimilar polymers presents a challenge due to the limitations of conventional techniques. Friction Stir Welding (FSW) emerges as a promising solution by enabling solid-state joining below the melting point. This study investigates the effect of AA7075 tool profile variations—plain cylinder, threaded cylinder, and grooved cone—on the mechanical properties and macrostructure of HDPE-PP FSW joints. Experimental welding was performed at a rotational speed of 2920 rpm and a travel speed of 30 mm/min, with analysis including tensile tests (ASTM D638), bending tests (ASTM D790), temperature measurements, and macrostructural observations. Results show that the threaded cylindrical tool yielded the highest tensile strength (4 MPa) due to effective material flow, while the grooved cone tool produced the highest bending strength (6,8 MPa) through improved vertical and radial mixing. The plain cylindrical tool showed the weakest performance with significant welding defects. Overall, tool geometry significantly influences weld quality, and selection should be based on the mechanical requirements of the application. These findings emphasize the importance of tool design optimization to enhance joint strength and structural integrity in dissimilar thermoplastic FSW.

Keywords: Friction Stir Welding (FSW), HDPE, Polypropylene (PP), AA7075 Tool, Tool Profile, Dissimilar Polymer Welding.

Abstrak: *Permintaan akan material ringan dalam industri otomotif mendorong penggantian komponen kendaraan berbahan logam dengan polimer seperti High-Density Polyethylene (HDPE) dan Polypropylene (PP) guna mendukung pembangunan berkelanjutan dan pengurangan emisi. Namun, penyambungan dua jenis polimer yang berbeda masih menjadi tantangan karena keterbatasan teknik pengelasan konvensional. Friction Stir Welding (FSW) hadir sebagai solusi menjanjikan karena mampu menyambung material dalam keadaan padat di bawah titik leleh. Penelitian ini mengkaji pengaruh variasi profil tool berbahan AA7075—silinder polos, silinder berulir, dan kerucut beralur—terhadap sifat mekanik dan makrostruktur sambungan FSW antara HDPE dan PP. Proses pengelasan dilakukan dengan kecepatan putar 2920 rpm dan kecepatan gerak 30 mm/menit, dengan analisis meliputi uji tarik (ASTM D638), uji lentur (ASTM D790), pengukuran temperatur, dan observasi makrostruktur. Hasil menunjukkan bahwa tool silinder berulir menghasilkan kekuatan tarik tertinggi (4 MPa) karena aliran material yang lebih efektif, sedangkan tool kerucut beralur menghasilkan kekuatan lentur tertinggi (6,8 MPa) berkat distribusi pencampuran material secara vertikal dan radial yang lebih baik. Tool silinder polos menunjukkan performa terendah dengan banyak cacat pada hasil las. Secara keseluruhan, geometri tool sangat memengaruhi kualitas sambungan, dan pemilihannya harus disesuaikan dengan kebutuhan mekanik aplikasi. Temuan ini menekankan pentingnya optimasi desain tool untuk meningkatkan kekuatan sambungan dan integritas struktural pada pengelasan FSW material termoplastik yang tidak sejenis.*

Kata kunci: *Friction Stir Welding (FSW), HDPE, Polypropylene (PP), Tool AA7075, Profil Tool, Pengelasan Polimer Tidak Sejenis.*

INTRODUCTION

The background of this research focuses on automotive developments that are increasingly shifting to electric-powered vehicles, which require high efficiency through weight reduction. There needs to be an emphasis on the importance of using lightweight materials to support sustainable development and reduce emissions [1]. One of the proposed strategies is replacing metal vehicle body components with polymers such as High-Density Polyethylene (HDPE) and Polypropylene (PP) [2]. Polymer materials are widely used in the automotive industry, particularly for vehicle coverings and interior components such as dashboard panels, bumpers, interior linings, engine covers, and lighting elements [3]. Although polymers offer advantages in terms of weight, the main challenge in their use is an effective joining method, considering that conventional welding techniques cannot be applied to this thermoplastic material [4].

Friction Stir Welding (FSW) method has emerged as an innovative solution for joining dissimilar polymers. Nagarajan stated that FSW allows welding at temperatures below the melting point of the material, thus avoiding adverse metallurgical reactions [1]. The Friction Stir Welding (FSW) work process consists of four stages, namely the plunging phase, the dwelling phase, the welding phase, and the exit/retract phase [5]. In the initial stage, the tool rotates and penetrates the surface of the material until it reaches the desired depth. Then, in the dwelling phase, the tool remains in place while continuing to rotate to generate heat until the working temperature is reached. After that, the tool begins to move along the joint path in the welding phase. The process ends with the tool being withdrawn from the material, which is called the exit phase. Various factors such as process parameters, tool design, and the type of material used will greatly affect the final result, including the mechanical quality of the resulting joint [6].

Various studies have examined the effect of tool shape and material as well as process parameters on the quality of FSW joints in HDPE and PP. Rezaee Hajideh found that H13 threaded cylindrical tools produced the strongest joints (23.7 MPa) and the most uniform stir zone, while plain cylindrical tools produced the weakest strength [7]. Bilici used a conical SAE1050 tool in a single-point joint, with the highest shear strength on PP-PP of 4226 N [8]. Sidhom used a carbon steel conical tool and found different optimal parameters for similar and dissimilar joints, with the best strength at rotational speeds of 3500 rpm (similar) and 2300 rpm (dissimilar) [9]. Ardyansyah used an H13 cylindrical tool showing that a feed rate of 12 mm/min produced the maximum strength (193.97 N) and the fewest defects [10]. Sugiarto used a threaded cylindrical SKD61 tool and showed the highest tensile strength (19.06 MPa) at 1800 rpm, but decreased at 2100 rpm due to excessive softening [2]. In general, tool shape, tool material type, and process parameters greatly affect the mechanical quality and macrostructure of FSW HDPE–PP joints.

FSW has become a revolutionary welding technique over the past two decades due to its energy efficiency, environmental friendliness, and high-quality joints [11]. Therefore, many studies have examined the effect of various FSW parameters as an effort to maximize the potential of FSW to produce the best welding. One effort that can be made is to choose the appropriate tool. The use of AA7075 material is an alternative choice as a tool in FSW because of its high thermal conductivity and mechanical strength so that it can inhibit the cooling rate of lava [7]. In addition, the cheaper price of AA7075 can also be an option for production budget efficiency. However, studies using AA7075 tools are still rare. Therefore, this study aims to determine the impact of the AA7075 tool profile on the characteristics of FSW dissimilar HDPE-PP welding results, so that it can provide insight for the industry in improving production quality and efficiency.

METHODS

The equipment used in this study: (a) Krisbow X 6325 milling machine (FSW modification), (b) Universal Testing Machine (UTM), (c) Bending test equipment (Three-point test). The main material of this study is a sheet of High-Density Plyethylene (HDPE) - Polypropylene (PP) which has dimensions of 125 mm x 57.5 mm and a thickness of 4 mm as shown in Figure 1. While the specifications of physical and mechanical properties can be seen in Table 1.

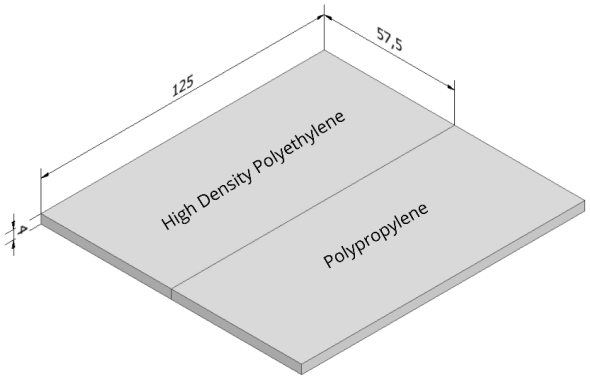

Figure 1. HDPE-PP material dimensions

Table 1. Mechanical properties HDPE-PP [12]

Mechanical Properties	Tensile Strength (Mpa)	Flexurual Strength	Hardness (SHD)
High Density Polyethylene	19	24.4	58.4
Polypropylene	30.9	47.2	71.8

The tool used uses AA7075 material with three different profile variations, namely plain cylinder, threaded cylinder, and groove cone. The dimensions of the tool profile can be seen in Figure 2.

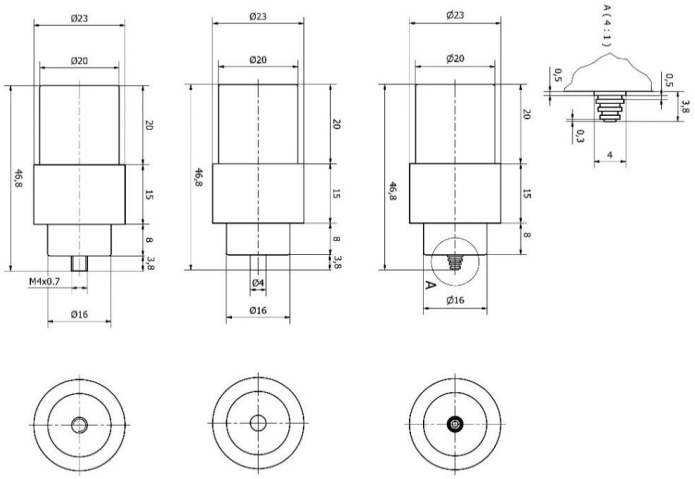

Figure 2. Tool profile dimensions

Although Friction Stir Welding (FSW) has been extensively studied and widely applied to the joining of steel and aluminum alloys, its application to polymer materials remains limited due to the absence of established industrial standards [13]. Therefore, the selection of process parameters is carried out through an experimental approach to obtain optimal joint quality [11]. In this study, the parameters were selected based on experimental results, with a rotation speed of 2920 rpm, travel speed of 30 mm/min, stirring depth of 3.90 mm, and tilt angle of 0° constantly. The FSW process scheme can be seen in Figure 3.

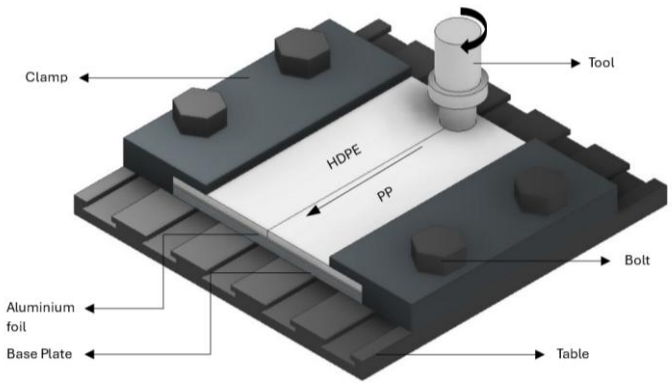

Figure 3. FSW process scheme

This research experiment was conducted at the Mechanical Engineering Laboratory of Semarang State University and Semarang Muhammadiyah University using a descriptive statistical analysis approach. This study

aims to identify the characteristics of the variables studied and describe data related to variations in the shape of the pin profile made of AA7075 and its impact on the quality of the Friction Stir Welding (FSW) connection between HDPE and PP. The results of this study will be presented in the form of macro-structure photos and graphs that include tensile and bending tests. Analysis of the FSW connection results was carried out using macro-structure photos, ASTM D790 Three Point Test bending tests, and ASTM D638 type IV tensile tests. The dimensions of the test specimens can be seen in Figure 4.

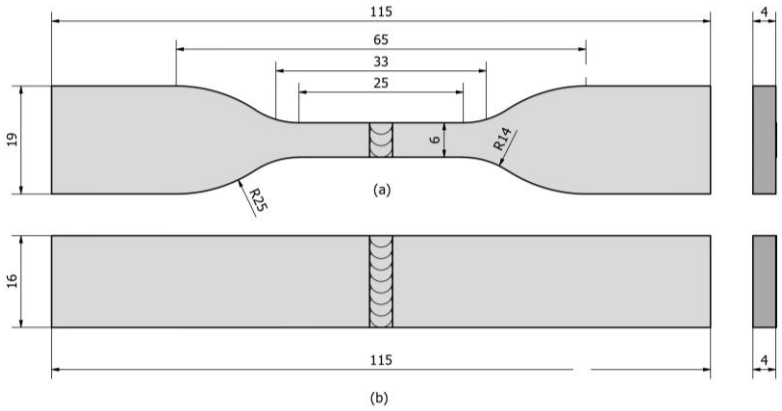

Figure 4. (a) Dimensions of tensile test specimens, (b) Dimensions of bending test specimens

RESULT AND DISCUSSION

The results of Friction Stir Welding (FSW) on HDPE and PP materials using a plain cylindrical tool shown in Figure 5 show that the main stirring zone (SZ) along the weld path appears darker and rougher than the surrounding area. This indicates the occurrence of plastic deformation and partial mixing of the material due to friction and pressure from the tool. However, the surface of the stirring zone appears uneven and is accompanied by indications of defects such as porosity, fine cracks, or irregular lines, indicating that the mixing between HDPE and PP does not occur homogeneously. These imperfections are most likely caused by the design limitations of the plain cylindrical tool which does not have stirring elements such as threads or pins. This also causes the welding results to turn black. The lack of agitation due to the plain cylindrical tool design, which does not have geometric features such as threads or grooves, results in ineffective material mixing [7], [9]. The material flow in the stir zone becomes stagnant, and the material is merely pushed rather than stirred, leading to continuous friction in a specific area. This accumulated friction generates excessive local heat, causing the temperature in the stir zone to exceed the thermal degradation threshold of HDPE and PP [9]. As a result, the polymer structure begins to break down and form carbon residue, which appears as blackening or burning in the weld joint [2]. Although AA7075 tools have good thermal conductivity, the inability to evenly distribute heat due to low agitation still leads to the formation of hot spots that trigger material degradation.

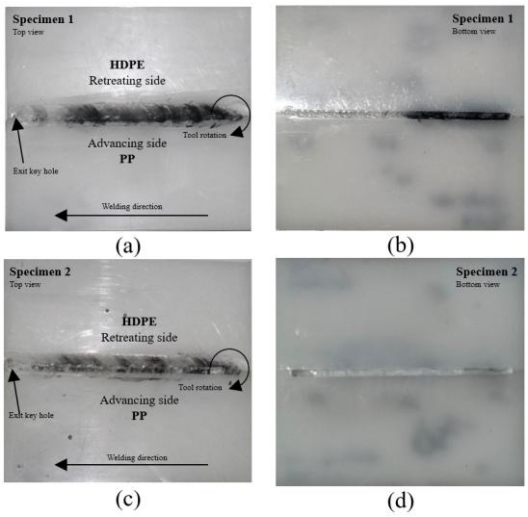

Figure 5. (a) FSW results of plain cylindrical tool specimen 1 top view, (b) FSW results of plain cylindrical tool specimen 1 bottom view, (c) FSW results of plain cylindrical tool specimen 2 top view, (d) FSW results of plain cylindrical tool specimen 2 bottom view

Based on the direction of rotation and translation of the FSW process and the orientation of the Figure 5, it can be identified that the upper part of the weld path is the retreating side (RS), while the lower part is the advancing side (AS). In RS, the direction of tool rotation is in the same direction as the translation, resulting in higher pressure and friction which causes the material flow to become more aggressive. This is evident on the upper surface of the weld path which looks rough and has the potential to cause defects such as flash or surface damage. In contrast, the AS at the bottom shows a more controlled material flow, with a relatively more stable surface although there are still indications of local porosity or roughness.

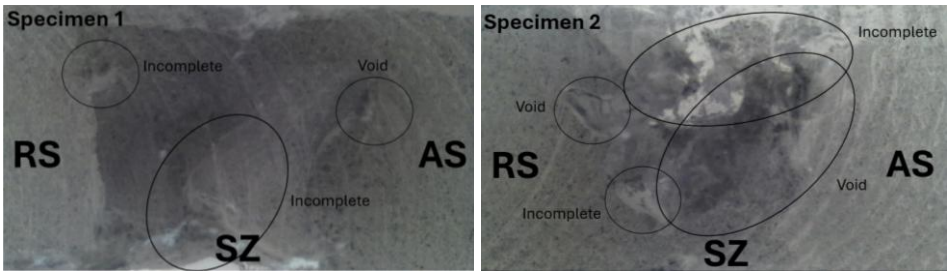

Figure 6. (a) Photo of macro structure of FSW result of plain cylindrical tool specimen 1, (b) Photo of macro structure of FSW result of plain cylindrical tool specimen 2

Based on the macrostructure image of the Friction Stir Welding (FSW) results between HDPE and PP using a plain cylindrical tool made of AA7075, a number of striking welding defects are visible, such as voids, incomplete fusion, and inhomogeneous stir zones (SZ). Voids, which appear as cavities in the joint, occur due to imperfect material mixing or trapped gas during the process, and this is exacerbated by the lack of agitation of the plain cylindrical tool that does not have cutting or stirring features such as pins or threads. Incomplete fusion or mixing that is not fully integrated is clearly visible on the advancing side (AS) and retreating side (RS), especially at the boundary between the SZ and the base material, indicating that the temperature and plastic deformation produced are not sufficient to melt the two types of polymers with different thermal characteristics. Plain tools tend to only push the material without stirring it effectively, so that the formed SZ is not uniform and contains internal defects. The combination of less than optimal process parameters does not support the flow of material as a whole, causes the formation of defective and mechanically weak joints. Therefore, to improve the quality of the joint, it is necessary to modify the tool with a more complex geometry and optimize the process parameters to produce a more homogeneous flow and mixing of the material with minimal defects.

The following are the results of FSW dissimilar HDPE-PP, variations in the profile of the threaded cylinder tool can be seen in Figure 7.

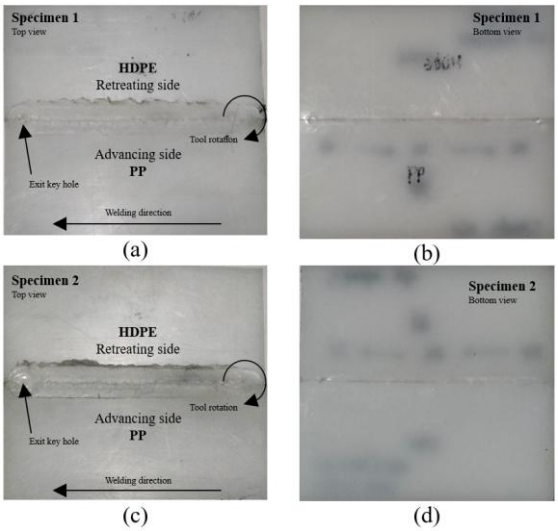

Figure 7. (a) FSW results of threaded cylinder tool specimen 1 top view, (b) FSW results of threaded cylinder tool specimen 1 bottom view, (c) FSW results of threaded cylinder tool specimen 2 top view, (d) FSW results of threaded cylinder tool specimen 2 bottom view

Based on observations of the FSW results of HDPE-PP using a threaded cylinder tool, it can be seen that the surface of the weld path is neater and more uniform compared to using a plain tool, which indicates that the mixing process and material flow are more optimal. The presence of threads on the tool plays an important role in pulling and directing the material to the stirring zone (SZ), thereby increasing the homogeneity of mixing and heat distribution. Based on the direction of the arrow and the position of the degrees listed, the top of the weld

path is the retreating side (RS) and the bottom is the advancing side (AS) [7]. The retreating side (RS) and advancing side (AS) show balanced visual results., indicating that the thread tool has succeeded in reducing the flow imbalance between AS and RS. The main cause of this quality improvement is the ability of the thread to create more intensive and even mechanical agitation, thereby reducing the potential for defects such as cavities and imperfect melting. As a result, the formed stirring zone becomes more consistent, well mixed, and has the potential to produce higher mechanical strength.

The macro structure image of Friction Stir Welding (FSW) between HDPE and PP materials using a cylindrical threaded AA7075 tool shows a welding defect in the form of incomplete fusion located on the retreating side (RS) in the stir zone (SZ). This defect appears as an unfused area marked on both cross sections, indicating a failure of perfect fusion between the materials in that section. This phenomenon occurs due to differences in melt viscosity characteristics between the two materials and the irregular temperature distribution during the process. The mismatch in thermal properties between HDPE and PP leads to an imbalance in melt flow behavior, thereby hindering the homogeneous mixing of materials. The uncontrolled temperature instability further contributes to the formation of defects in the form of incomplete mixing [12].

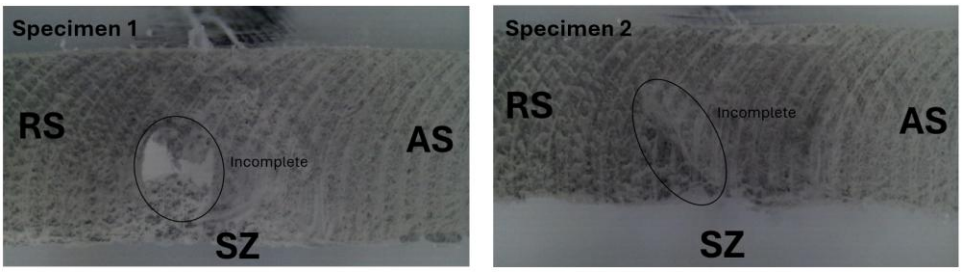

(a) (b)

Figure 8. (a) Photo of macro structure of FSW result of threaded cylinder tool specimen 1, (b) Photo of macro structure of FSW result of threaded cylinder tool specimen 2

Although the threaded tool has better agitation and heat distribution capabilities than the plain tool, these results show that the mixing process is not completely homogeneous throughout the depth or width of the weld zone, especially in the AS section. This can be caused by a combination of several factors, including less than optimal thread geometry in lifting material from bottom to top, insufficient downforce to push the material completely into the mixing zone, or local temperature imbalance due to the difference in viscosity between HDPE and PP. The result of this incomplete fusion is the formation of a joint that is not completely fused, which has the potential to be the starting point for cracks when receiving mechanical loads, as well as reducing the tensile strength and structural integrity of the joint as a whole. Therefore, although the use of threaded tools shows better results than plain tools, further optimization of the thread design, tool pressure, and process parameters is needed so that material mixing in the SZ can occur more evenly and thoroughly on all sides of the joint.

The results of FSW dissimilar HDPE-PP with variations in the profile of the conical groove tool can be seen in Figure 9.

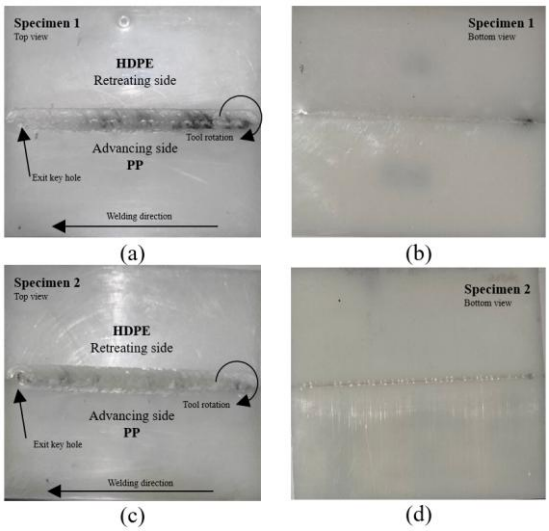

(a) (b) (c) (d)

Figure 9. (a) FSW results of conical groove tool specimen 1 top view, (b) FSW results of conical groove tool specimen 1 bottom view, (c) FSW results of conical groove tool specimen 2 top view, (d) FSW results of conical groove tool specimen 2 bottom view

From Figure 9 shows the stir zone (SZ) weld groove that is more integrated compared to using a regular or plain thread tool, with a fairly clear surface appearance and shows a relatively even material flow, although irregularities are still visible in some areas. Based on the translation and rotation direction of the process and the orientation in the image, the upper part of the weld path can be identified as the retreating side (RS), while the lower part is the advancing side (AS). The cone-shaped tool with grooves provides the advantage of producing more intensive vertical and radial material flow. The grooves on the tool function to lift and spread the material evenly throughout the stir zone, thereby increasing the homogeneity of mixing between HDPE and PP which have different thermoplastic properties. However, it turns out that on the RS side the surface tends to be rougher and darker, which can indicate the presence of material flow that is too aggressive due to friction and high local temperatures, so that it is at risk of causing defects such as small cavities or excessive heat. This can be caused by an imbalance in downforce or a mismatch in the viscoelastic response between the two materials [12]. Scientifically, these results show that the grooved cone tool is able to improve the distribution of plastic deformation and heat transfer during the FSW process, but still requires optimal parameter settings so that mixing and formation of the stirring zone can occur thoroughly and without defects on all sides of the joint.

The cone-shaped tool with grooves has special characteristics in the form of a tapered shape with axial grooves designed to increase the flow of material vertically and radially during the Friction Stir Welding (FSW) process. This design allows the material flow to be deeper and more comprehensive compared to plain or threaded tools, because the grooves on the tool surface function to lift and distribute the material evenly throughout the stir zone (SZ). However, defects such as incomplete fusion and voids are still found, although they are more localized. This is generally caused by the difference in viscosity between HDPE and PP and process parameters that are not yet fully optimized, so that some parts of the material remain incompletely mixed. As a result, the resulting joints are stronger and more even compared to plain and threaded tools, but are not completely free from defects, especially on certain sides of the SZ which require further control of temperature, pressure, and tool geometry.

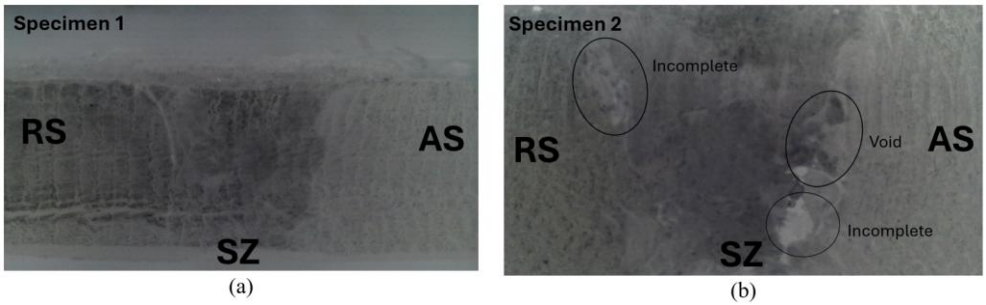

Figure 10. (a) Photo of macro structure of FSW result of conical groove tool specimen 1, (b) Photo of macro structure of FSW result of conical groove tool specimen 2

When compared with the results of Friction Stir Welding (FSW) using plain and threaded tools, the macrostructure of the FSW results with a conical grooved tool shows significant improvement, although there are still defects such as incomplete fusion and voids. Plain tools, which do not have stirring features such as threads or grooves, produce very limited material flow with a narrow and inhomogeneous stir zone (SZ), which often causes defects such as porosity, delamination, and structurally weak joints. Threaded tools provide improvements by producing a wider and more even SZ because the threads help to flow the material in a spiral manner, but still leave defects especially on the advancing side (AS) if the process parameters are not optimal. Meanwhile, the conical grooved tool has the advantage of creating more intensive and even mechanical agitation, because its axial grooves are able to lift and spread material throughout the stir zone. As a result, mixing between HDPE and PP becomes more effective and the SZ is formed with better distribution compared to the previous two tools. However, defects can still appear due to differences in material viscosity and imperfect local heat distribution. Therefore, although the grooved cone tool is the most potential choice in improving the quality of FSW joints between HDPE and PP, the tool design settings and process parameters still need to be optimized to produce homogeneous and defect-free joints.

Table 2. FSW process temperature

Profile Pin	Spesimen	Starting (°C)	Center (°C)	Final (°C)
Plain Cylinder	1	45	66	55
	2	46	58	63
Threaded Cylinder	1	46	70	70
	2	42	71	72
Groove Cone	1	40	52	63
	2	50	65	77

During the FSW process, the temperature is measured using a thermogun. There are three points where the temperature is measured during the welding process, namely the beginning, middle, and end. This temperature measurement is intended to determine the change in material temperature.

Plain cylindrical tools produce the lowest quality welding results. This is due to the absence of geometric features such as threads or grooves that can help mix the material effectively. The material flow is very limited, so that the stir zone (SZ) formed is narrow and inhomogeneous. As a result, many defects such as voids, incomplete fusion, and delamination are found, especially on the advancing side (AS), which causes the joint to be mechanically weak and structurally unfit. Threaded cylindrical tools provide significant improvements compared to plain tools. The threads play a role in pulling and directing the material flow into the SZ, resulting in more even mixing and a wider SZ. However, defects such as incomplete fusion and voids can still be found, especially if the process parameters (rotational speed, translation, and pressure) have not been optimized. The resulting joints are generally stronger than plain tools, but not completely homogeneous. Grooved cone tools show the best results among the three. The cone design facilitates penetration into the material, while the axial grooves enhance the vertical and radial flow of the material, resulting in more effective mixing distribution within the SZ. The grooves help lift and spread the material throughout the mixing zone, resulting in deeper, denser, and more even joints. Although incomplete fusion or localized voids can still be found, the number and severity are much lower than the previous two tools. The resulting joints are more homogeneous and have higher mechanical strength, making the cone-grooved tool the most potential choice in FSW welding of HDPE–PP, provided that the process parameters are properly adjusted.

Table 3. Tensile test results

Profile Tool	Sample	Width (mm)	Thickness (mm)	Area (mm^2)	Max Force (N)	Bending Strenfth (MPa)	Average Bending Strength (MPa)
Plain Cylinder	1	6	4	24	89.1	3.7	3.8
	2	6	4	24	95.4	4	
Threaded Cylinder	1	6	4	24	71.5	3	4
	2	6	4	24	122.9	5.1	
Groove Cone	1	6	4	24	79.1	3.3	3.2
	2	6	4	24	74.12	3.1	

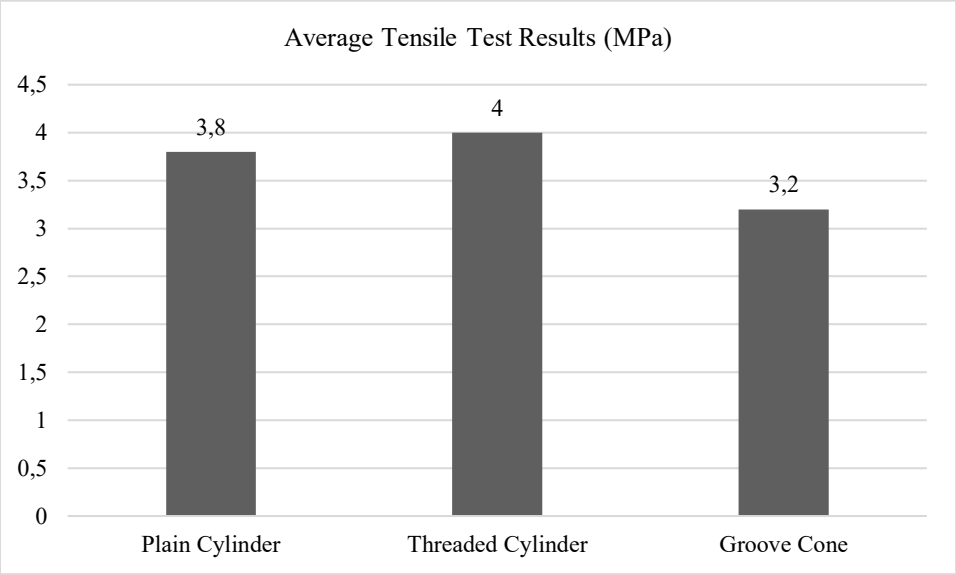

Figure 11. Average tensile strength diagram

Figure 11 shows the average bar chart of the tensile strength of the Friction Stir Welding (FSW) results between HDPE and PP using three types of tool profiles: plain cylinder, threaded cylinder, and groove cone. Based on the data in the graph, the highest average tensile strength value was obtained using a threaded cylinder tool of 4 MPa, followed by a plain cylinder with a strength of 3.8 MPa, and the lowest was a groove cone tool with a value of 3.2 Mpa.

These results indicate that although theoretically the groove cone tool has the most complex design to improve material mixing, in practice it has not been able to produce joints with the highest tensile strength. This is most likely due to the presence of defects such as incomplete fusion and voids in the weld results with the groove cone tool, as seen in the previous macrostructure. The groove cone tool is designed to generate strong

radial and vertical material flow, but the longitudinal distribution (along the length of the joint) may be uneven. This results in defects such as small incomplete fusions that occur along the weld path, which are not visually apparent on the surface but significantly affect the tensile strength, as it is highly sensitive to the presence of small defects [13], [14]. This is different from the welding results using the plain cylindrical tool, where relatively large defects were found but did not occur frequently along the weld path. The groove design on the tool may not be fully optimized or process parameters such as pressure drop, temperature, and stirring time have not been adjusted to the different viscosity properties of HDPE and PP.

Meanwhile, the threaded cylindrical tool showed the best performance because the thread is able to effectively pull and spread the material along the stir zone (SZ), resulting in more homogeneous mixing and significant reduction in defects. The plain cylindrical tool, although simple, produced tensile strengths close to those of the threaded tool, indicating that under certain conditions, the simplicity of the design can still provide competitive mechanical results as long as the process parameters are appropriate. Thus, of the three tool profiles tested, the threaded cylindrical tool produced the highest tensile strength, while the conical groove tool gave the lowest tensile strength, indicating the need for further optimization of complex tools to be able to produce results in accordance with their theoretical design.

Table 4. Bending test results

Profile Tool	Sample	Width (mm)	Thickness (mm)	Area (mm^2)	Max Force (N)	Bending Strenfth (MPa)	Average Bending Strength (MPa)
Plain Cylinder	1	16	4	64	9.8	3.7	5.9
	2	16	4	64	21.6	8,1	
Threaded Cylinder	1	16	4	64	21.9	8,2	6.1
	2	16	4	64	10.7	4	
Groove Cone	1	16	4	64	17.1	6.4	6.8
	2	16	4	64	19.3	7.2	

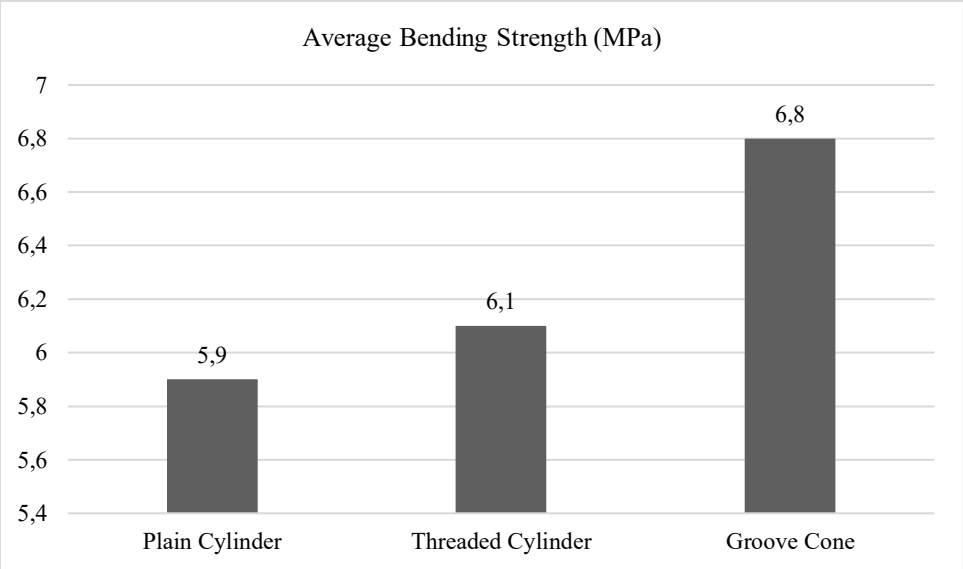

Figure 12. Average tensile strength diagram

Figure 12 shows a bar chart of the average bending strength of the Friction Stir Welding (FSW) welding results on HDPE and PP materials using three types of tool profiles, namely plain cylinder, threaded cylinder, and grooved cone. Based on the data in the graph, the highest bending strength value was achieved by the grooved cone tool with an average of 6.8 MPa, followed by the threaded cylinder at 6,1 MPa, and the lowest was the plain cylinder with a strength of 5,9 MPa.

These results indicate that in terms of resistance to bending, the grooved cone tool shows the best performance. This indicates that the axial groove design on the cone tool is able to increase the distribution of material during the welding process, resulting in a denser, more unified, and elastic joint against bending forces. Although in the previous tensile strength test this tool was not superior, in the bending test the grooved cone tool showed superiority, which was most likely due to better material distribution around the stir zone (SZ) so that it was able to withstand bending deformation. The difference in results between the tensile and bending tests of FSW HDPE-PP using the groove cone tool is caused by the characteristics of the material flow generated. The groove cone tool is designed to promote strong material flow in the radial and vertical directions, but the

longitudinal distribution (along the length of the joint) tends to be uneven. As a result, small incomplete fusion defects are formed along the weld path. Although these defects are not visually apparent on the surface, they have a significant impact on tensile strength due to its high sensitivity to imperfections [13], [14]. On the other hand, the bending test results show higher values because the axial groove design on the tool produces strong, uniform, and homogeneous surface flow, resulting in better structural integrity of the outer joint area, which plays a crucial role in resisting bending loads.

The threaded cylinder tool still provides quite good results because the thread can increase material flow and help reduce defects such as incomplete fusion. Meanwhile, the plain cylindrical tool showed the lowest performance, which is in line with the characteristics of its limited material flow due to the absence of a stirring element, resulting in a less integrated joint and easy to crack when subjected to bending loads. Thus, of the three tools tested, the groove cone tool produced the highest bending strength, while the plain cylindrical tool produced the lowest, indicating that the geometric design of the tool greatly influences the mechanical performance of the joint in the context of bending resistance.

CONCLUSIONS

AA7075 tools with various profiles (plain cylinder, threaded cylinder, and grooved cone) showed limited ability to produce truly homogeneous and defect-free joints. The plain cylinder tool had the lowest agitation, resulting in a narrow stir zone (SZ) and many defects such as voids and incomplete fusion. The threaded cylinder tool increased the material flow spirally, resulting in a more even SZ and the best tensile strength among the three, but still left local defects. Meanwhile, the grooved cone tool was theoretically the most effective in distributing material because its grooves lifted and spread the material vertically and radially, but in practice it produced the lowest tensile strength, despite the highest bending strength, indicating an imbalance between mixing and joint compactness.

Each profile showed different performance in terms of macrostructure, tensile strength, and bending strength. The plain cylinder tool produced the lowest quality joints, characterized by an inhomogeneous stir zone (SZ) and many defects such as voids and incomplete fusion due to minimal material flow and mixing. The threaded cylindrical tool showed the best performance in the tensile test with an average strength of 4 MPa, because the thread is able to pull and guide the material more effectively, resulting in more even mixing and reducing defects. On the other hand, the conical groove tool, although not producing the highest tensile strength (3.2 MPa), managed to record the highest bending strength of 6.8 MPa, due to its ability to distribute the material vertically and radially intensively through the axial groove. The difference in results shows that each tool has its own advantages depending on the type of load tested. Thus, the threaded cylindrical tool is recommended to increase the tensile strength, while the conical groove tool is more effective for applications requiring high flexural resistance. These results also emphasize the importance of tool design selection and process parameter optimization in improving the quality of FSW joints between dissimilar thermoplastic materials.

ACKNOWLEDGEMENT

We would like to thank the Department of Mechanical Engineering, Semarang State University and Muhammadiyah University of Semarang and all parties involved in this research, especially fellow researchers, lecturers, and technicians at both academic institutions.

REFERENCES

[1] Y. Sun *et al.*, "Investigation of tool offset on the microstructure and mechanical properties of AA6061-T6/PC Friction Stir Butt Welding joint," *J. Reinf. Plast. Compos.*, vol. 44, no. 5–6, pp. 295–308, Dec. 2023, doi: 10.1177/07316844231219319.

[2] Sugiarto, M. S. Ma'arif, A. Wahjudi, and A. L. Ananto, "Analisis Mekanik Sambungan Dissimilar Friction Stir Welding Antara High Density Polyethylene Dengan Polypropylene," *Seminar Nasional Tahunan Teknik Mesin XXII 2024*. Indonesia, pp. 205–209, 2025. doi: 10.71452/590657.

[3] J. N. Septiyanto, A. Azis, N. Syafiqri, F. F. Firdaus, and R. Y. Parapat, "Potensi Nanokomposit dalam Mengoptimalkan Desain Bodi Kendaraan Modern," *Sci. J. Ilm. Sains dan Teknol.*, vol. 3, no. 3, pp. 169–188, 2025.

[4] A. R. Romadhan, A. W. Nugroho, T. Suwanda, and R. Wilza, "Sifat Tarik dan Struktur Mikro Sambungan Las Gesek Tak Sejenis Baja-Tembaga," *JMPM (Jurnal Mater. dan Proses Manufaktur)*, vol. 3, no. 1, pp. 20–27, Jun. 2019, doi: 10.18196/jmpm.3133.

[5] A. Muchhadiya *et al.*, "Optimization of friction stir welding process parameters for HDPE sheets using satisfaction function approach," *Indian J. Eng. Mater. Sci.*, vol. 31, no. 1, pp. 58–66, 2024, doi: 10.56042/ijems.v31i1.561.

[6] P. Asadi, M. R. M. Aliha, M. Akbari, D. M. Imani, and F. Berto, "Multivariate optimization of mechanical and microstructural properties of welded joints by FSW method," *Eng. Fail. Anal.*, vol. 140, p. 106528, 2022, doi: 10.1016/j.engfailanal.2022.106528.

[7] M. Rezaee Hajideh, M. Farahani, S. A. D. Alavi, and N. Molla Ramezani, "Investigation on the effects of tool geometry on the microstructure and the mechanical properties of dissimilar friction stir welded polyethylene and polypropylene sheets," *J. Manuf. Process.*, vol. 26, pp. 269–279, 2017, doi: 10.1016/j.jmapro.2017.02.018.

[8] Mustafa Kemal Bilici, "Investigation of friction stir spot welding of high density polyethylene and polypropylene sheets," *J. Elastomers Plast.*, vol. 53, no. 7, pp. 922–940, Mar. 2021, doi: 10.1177/00952443211001526.

[9] A. A. E. Sidhom, S. A. R. Naga, and A. M. Kamal, "Friction stir spot welding of similar and dissimilar high density polyethylene and polypropylene sheets," *Adv. Ind. Manuf. Eng.*, vol. 4, p. 100076, 2022, doi: 10.1016/j.aime.2022.100076.

[10] N. Ardiyansyah, T. Suwanda, F. A. K. Yudha, and A. Purnama, "Effect of Feed Rate on Shear Strength and Macrostructure of Friction Stir Welding Dissimilar High Density Polyethylene-Polypropylene Joint," *J. Polimesin*, vol. 22, no. 4, pp. 416–419, 2024, doi: 10.30811/jpl.v22i4.5285.

[11] X. Meng, Y. Huang, J. Cao, J. Shen, and J. F. dos Santos, "Recent progress on control strategies for inherent issues in friction stir welding," *Prog. Mater. Sci.*, vol. 115, p. 100706, 2021, doi: https://doi.org/10.1016/j.pmatsci.2020.100706.

[12] R. Ramadhani, F. B. Darsono, A. Bahatmaka, Kriswanto, T. O. Prasdika, and S. B. Azara, "Characteristics of Pin Profile Variations in Friction Stir Welding (FSW) Joints of High Density Polyethylene (HDPE) And Polypropylene (PP) on Mechanical Properties," *VANOS J. Mech. Eng. Educ.*, vol. 10, no. 1, pp. 128–142, 2025, doi: 10.30870/vanos.v10i1.32501.

[13] B. Ahmad, F. Almaskari, J. Sheikh-Ahmad, S. Deveci, and K. Khan, "Thermomechanical Modeling of Material Flow and Weld Quality in the Friction Stir Welding of High-Density Polyethylene," *Polymers*, vol. 15. p. 3230, 2023. doi: 10.3390/polym15153230.

[14] S. H. Iftikhar, A.-H. I. Mourad, J. Sheikh-Ahmad, F. Almaskari, and S. Vincent, "A Comprehensive Review on Optimal Welding Conditions for Friction Stir Welding of Thermoplastic Polymers and Their Composites," *Polymers*, vol. 13. p. 1208, 2021. doi: 10.3390/polym13081208.

PISTON
Journal of Technical Engineering:

Design of Handoff Communication Sequence Architecture in LoRa Networks

Istas Pratomo Manalu[1,a)], Frengki Simatupang[1], Eka Stephani Sinambela[1], Marojohan Mula Timbul Sigiro[1], Gerry Italiano Wowiling[1], Sari Muthia Silalahi[1]

[1]*Institut Teknologi Del, Jl. Sisingamangaraja, Sitoluama, Laguboti, Toba Samosir, 22381, Indonesia*

E-mail: [a)] istaspratomo8@gmail.com

Received: July 05, 2025 *Revision: August 08, 2025* *Accepted: August 10, 2025*

Abstract: Technological advances have driven the development of IoT-based object tracking systems, where LoRa is an ideal wireless technology due to its long range and low power consumption. Challenges in implementing LoRaWAN, particularly its role in the handoff process between gateways that can disrupt communication, can be overcome by developing a more efficient handoff method. For this reason, this study presents the design of Handoff communication for the LoRa Network. We use two gateways and one transmitter node. The gateway node consists of a LoRa module and an ESP32, while the Transmitter consists of a LoRa module, an Arduino Nano, and a GPS sensor. The RSSI parameter is a determining factor in transferring connectivity paths from GW A or GW B, as it provides an RSSI threshold value of -100 dBm. We successfully designed handoff communication at each Node and conducted a mini-test. The test results show that LoRa can implement handoff techniques at a distance of 0-500 meters. This indicates that the node is in closer range to GW A. The RSSI value of GW1 is in the range of -52 dBm to -98 dBm, while the RSSI of GW2 is in a much weaker range, which is around -120 dBm to -100 dBm. As the distance increases, the RSSI value of GW1 shows a significant decrease, while the RSSI of GW B actually increases. At a distance of approximately 250 meters, there is an intersection point between the RSSI values of the two gateways, marking the optimal handoff point. Thus, this system is able to select the best gateway, provide redundancy, check gateway availability before handoff, and handle handoff failures, thereby improving the efficiency and effectiveness of data delivery.

Keywords: Handoff, LoRa, LoRaWAN, RSSI, IoT.

Abstrak: *Kemajuan teknologi telah mendorong pengembangan sistem pelacakan objek berbasis IoT, di mana LoRa menjadi teknologi nirkabel yang ideal karena jangkauan luas dan konsumsi daya rendah. Tantangan dalam penerapan LoRaWAN, khususnya perannya dalam proses handoff antar gateway yang dapat mengganggu komunikasi, dapat diatasi dengan mengembangkan metode handoff yang lebih efisien. Oleh karena itu, penelitian ini menyajikan rancangan komunikasi handoff pada jaringan LoRa. Sistem menggunakan dua gateway dan satu transmitter node. Gateway node terdiri dari modul LoRa dan ESP32, sedangkan transmitter menggunakan modul LoRa, Arduino Nano, dan sensor GPS. Parameter RSSI menjadi faktor penentu dalam pemindahan jalur konektivitas dari GW A ke GW B atau sebaliknya, dengan ambang batas RSSI sebesar -100 dBm. Rancangan komunikasi handoff berhasil diimplementasikan pada setiap node dan diuji secara mini. Hasil pengujian menunjukkan bahwa LoRa mampu menerapkan teknik handoff pada jarak 0–500 meter. Pada jarak ini, node berada dalam jangkauan lebih dekat dengan GW A. Nilai RSSI GW1 berkisar antara -52 dBm hingga -98 dBm, sedangkan RSSI GW2 berada pada kisaran yang lebih lemah, yakni -120 dBm hingga -100 dBm. Seiring bertambahnya jarak, nilai RSSI GW1 mengalami penurunan signifikan, sementara nilai RSSI GW B justru meningkat. Pada jarak sekitar 250 meter terjadi titik perpotongan nilai RSSI kedua gateway, yang menandai titik handoff optimal. Dengan demikian, sistem ini mampu memilih gateway terbaik, menyediakan redundansi, memeriksa ketersediaan gateway sebelum handoff, serta menangani kegagalan handoff, sehingga meningkatkan efisiensi dan efektivitas pengiriman data.*

Kata kunci: *Handoff, LoRa, LoRaWAN, RSSI, IoT.*

INTRODUCTION

In practice, Long Range (LoRa) technology is widely used in Internet of Things (IoT) systems because of its ability to transmit data over long distances with low power consumption. However, most LoRa applications are still static, with the transmitter node and gateway in fixed positions. When used in highly mobile scenarios, such as moving vehicles or objects, data communication is disrupted when nodes move away from the initial gateway and enter the coverage area of another gateway. The main problem that occurs is the lack of a reliable handoff mechanism in standard LoRa networks, leading to data loss (packet loss), increased latency, and reduced communication quality when nodes switch from one gateway to another. This issue is especially critical in real-time applications like logistics tracking, vehicle monitoring, or mobile security systems.

The development of information and communication technology is currently experiencing rapid growth, along with the ongoing progress of infrastructure and technological innovation. One important advancement is in the field of wireless technology. This technology, such as Wireless Local Area Network (WLAN), is now much easier to implement than wired networks, making it an essential part of modern communication systems [1], [2]. A WLAN, or Wireless Local Area Network, is a local network that utilizes high-frequency radio signals to transmit and receive data within a specific range. LoRaWAN technology enables long-distance communication with low data rates and minimal energy consumption, making it a popular choice in various IoT applications. Several studies have shown that this technology is capable of reaching communication distances of up to 10-15 km in rural or open areas [3]–[7].

Handoff is the process of transferring a connection from one gateway to another that occurs when a device moves across the signal coverage boundary [8]–[11]. This technique has been frequently applied in cellular networks, but its application to LoRa networks still requires further in-depth research and optimization. The differences in LoRa characteristics, such as higher latency and narrower bandwidth compared to cellular networks, pose a challenge to the development of handoff techniques on this network [12].

The purpose of this study is to provide a mechanism for handoff communication on the LoRa network. This study will provide instructions on how communication is established from one gateway to another to maintain communication. Furthermore, performance will be analyzed through RSSI comparison between gateways to provide the best path options that can handle data flow [13], [14]. This study will also compare various existing or developed techniques for LoRa networks, with the aim of finding the most effective method based on test results. Finally, this study will compile recommendations to optimize the implementation of the LoRa network, thereby improving the Quality of Service (QoS) in IoT applications that involve device mobility.

METHODS

The research conducted aims to apply handoff techniques to LoRa networks, similar to cellular networks [15]. Therefore, real simulations using physical devices are necessary. This study uses two gateway devices and one device that functions as a data sender.

Figure 1 shows that Gateway A and Gateway B (GW A and GW B) are receivers of data sent by the sender. This device is equipped with an RFM95 LoRa module, an Arduino Nano, and an antenna, which allows GW A to receive LoRa signals from the sender, measure the signal strength (RSSI value), and process the received data. GW A will be positioned at a specific location and serve as one of the two primary receivers in the system. If the signal received from the sender at GW A is stronger than at GW B, then GW A will prioritize receiving and sending the data. Gateway B has the same function as Gateway A, namely, as a data receiver from the sender. With the same device as GW A (Lora RFM95, Arduino nano, and Antenna). GW B will be placed at a different point from GW A to cover a wider area. GW B will function as the leading receiver if the signal received from the sender is stronger from GW B than from GW A. If GW A fails or cannot receive a signal, then GW B will become an alternative data receiver and forward the data. The sender acts as a data transmission device equipped with a GPS module, an LoRa RFM95 module, an Arduino Nano, and an Antenna. The primary function of the sender is to collect location data in the form of air quality values and select which Gateway will be prioritized for receiving data via LoRa signals. When moving through the area covered by GW A and GW B, the sender continuously transmits signals containing air quality data. The sender can also detect signals from gateways, so it can select the most optimal gateway (with the strongest signal) to receive and forward its data.

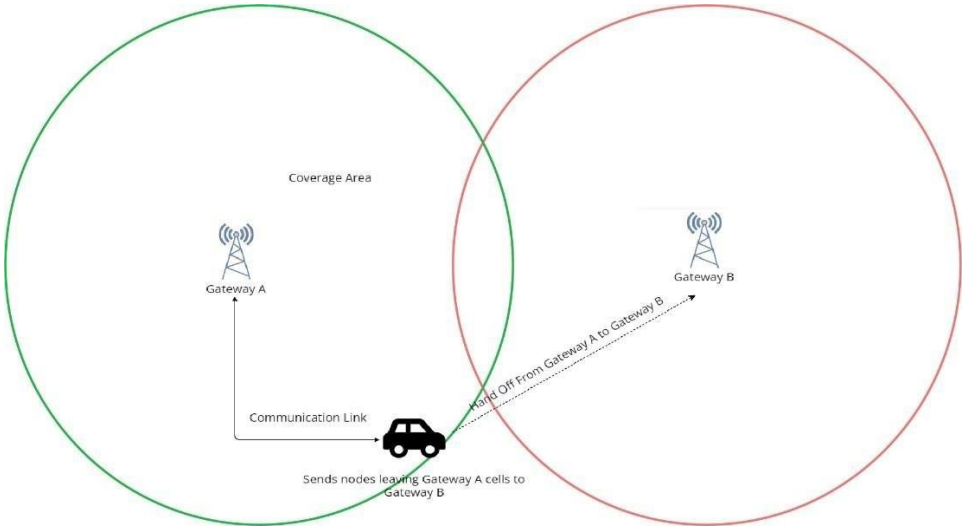

Figure 1. System Architecture Design

Tracking using LoRaWAN technology enables the remote monitoring and tracking of a device's position or movement. The tracking process using LoRaWAN involves installing a LoRa device on an object or other moving device that you want to track, such as a vehicle, animal, person, or other entity. Although tracking using LoRaWAN offers several advantages, such as a wide range and low power consumption, some problems still occur, one of which is data loss when the device moves from one coverage area to another. In overcoming these problems, implementing a handoff technique into a tracking system using LoRa can be an effective solution. The handoff technique enables the device to transition seamlessly from one coverage area to another without losing connection or data. By implementing an efficient handoff technique, the object tracking system can maintain connection reliability and data continuity as the object moves within the LoRaWAN network coverage area. This will help reduce the risk of data or network loss, thereby increasing the reliability and effectiveness of the tracking system using LoRa.

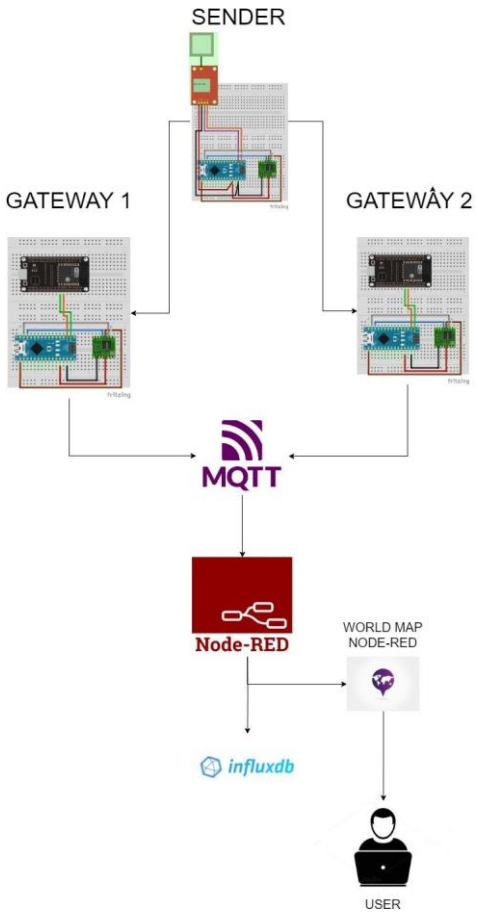

Figure 2. LoRa Network Topology with Two Gateways and MQTT–Node-RED Integration

The GPS module tracks the movement of an object or device and determines its accurate geographic position. Then, the data obtained from the Sender will be sent to the gateway using the LoRaWAN protocol with a string data format, where the tested parameter values, such as SNR and RSSI, are generated by the LoRa node using the `LoRa.packetRssi() and LoRa.packetSnr() commands`. The data obtained by the gateway will be converted to JSON and then transmitted using the ESP32 microcontroller to Node-RED, where Node-RED will parse the JSON data and store it in the InfluxDB database.

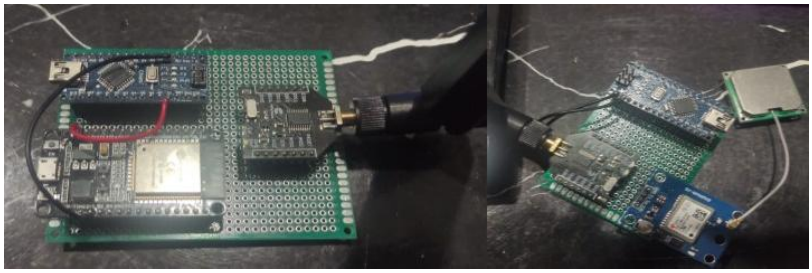

Figure 3. The transmitter and the Gateway Design

The components of the LoRa Gateway include an ESP32, an RFM95 LoRa module, a GPS module, and a power bank. All elements will be connected using jumper cables or a PCB. The components of the LoRa Node include LORA RFM95, a GPS module, and a power bank, and all elements will be connected using jumper cables or PCBs.

RESULT AND DISCUSSION

Handoff techniques enable devices to transition seamlessly from one coverage area to another without losing connection or data. To ensure the accurate detection of the moving device's location and obtain more valid data results, the use of handoff techniques in tracking systems utilizing LoRa technology can mitigate interference constraints when relocating the object. By implementing efficient handoff techniques, object tracking systems can maintain connection reliability and data continuity even when the device is moving within the LoRaWAN network. In addition to mitigating data loss, handoff techniques can also minimize the risk of network disruptions that may compromise the effectiveness of object tracking. The testing method applied to LoRa technology is expected to provide an in-depth understanding of system performance, including data transmission, application response, and optimization of height and distance. Positive results from implementing the Handoff Technique are expected to enhance the quality and reliability of object tracking, making a significant contribution to the development of object tracking technology using LoRaWAN.

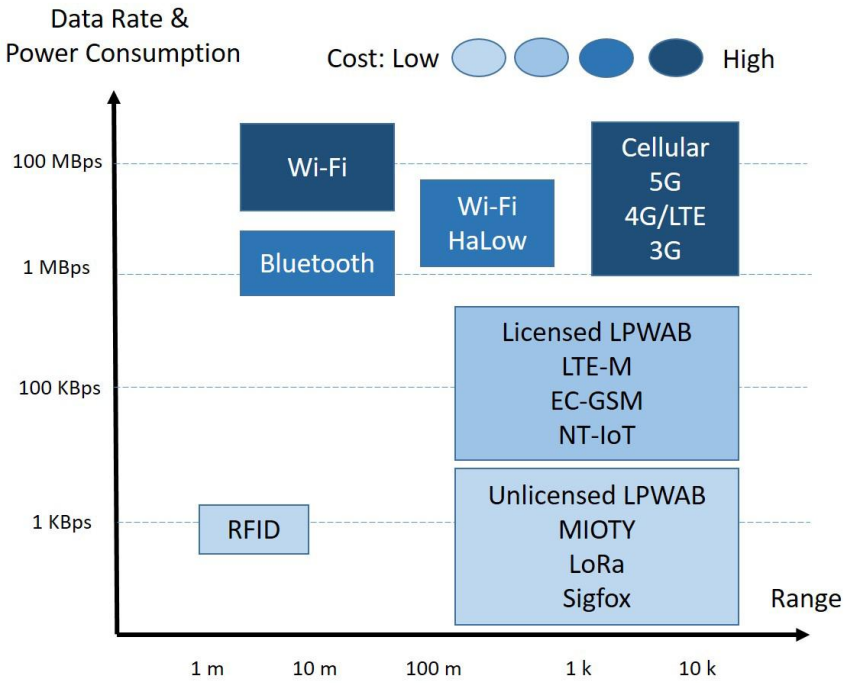

Figure 4. Comparison between LoRaWAN and other wireless technologies [1]

Compared to Wi-Fi and Bluetooth, LoRa provides a much greater range despite its significantly lower data rate. Wi-Fi and Bluetooth are suitable for short-range communications and high-speed applications but are not energy-efficient. In contrast, network technologies like LTE-M, EC-GSM, and NB-IoT operate in licensed spectrum (Licensed LPWAN), whereas LoRa uses license-free spectrum, reducing implementation costs significantly. The light blue color in the LoRa representation in the graph also indicates that its practical costs are relatively low compared to other technologies, such as cellular, which are darker in color. Therefore, although LoRa is not ideal for high-bandwidth or real-time communication, it is highly effective for long-range, energy-efficient, and low-cost communication systems.

The experiment was conducted in a semi-open environment within a campus area that features varied terrain, including open asphalt roads, sparse tree cover, and several low-rise buildings. The system consists of one mobile transmitter node (sender) equipped with a GPS sensor and two static gateways (GW1 and GW2), positioned at two different locations with a 500-meter distance between them. The transmitter node sends dummy sensor data every 5 seconds, along with GPS coordinate information and RSSI values received by each gateway. The handoff process is determined locally by the transmitter node based on the highest RSSI value received from the gateways, with a gateway switching mechanism every time there is a change in signal dominance.

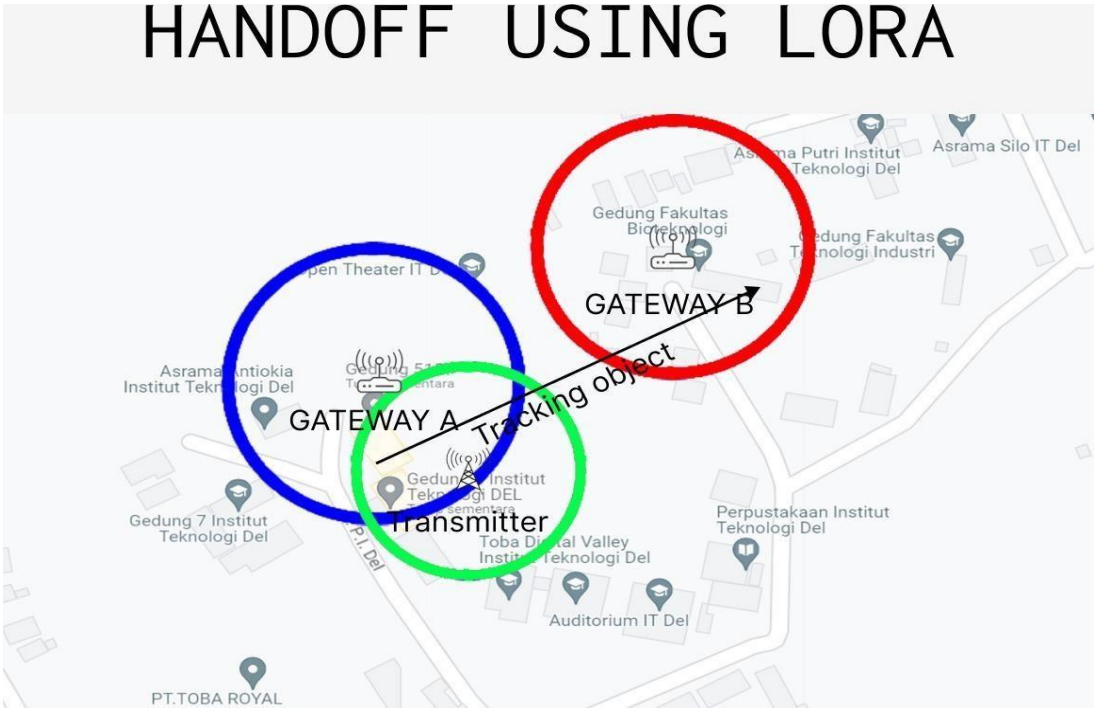

Figure 5. Maps of handoff implementation

Gateway A is a LoRa receiver comprising a LoRa RFM95 module, an antenna, an Arduino Nano, and a power bank as the power supply. Gateway B is a LoRa receiver that comprises an RFM95 module, an antenna, an Arduino Nano, an ESP32, and a power bank as its power supply. Node as a LoRa Transmitter composed of several components, such as LoRa RFM95, a GPS module that functions to receive data from the LoRa Receiver and send it to InfluxDB via Node-RED. In the design of this research, there are several components needed, such as Node sender, Gateway (there are two gateways), MQTTX (as data delivery media), Node-RED, InfluxDB (as database), and WorldMap (as interface). Each component has its function, such as a node device that will receive the location point results from the GPS module. Then, the received data will be sent to the gateway using the LoRa protocol. Furthermore, the gateway will receive the data and forward it to the InfluxDB database using a network (Wi-fi). The data obtained by Node-RED will be displayed on the world map.

Handoff Communication Process

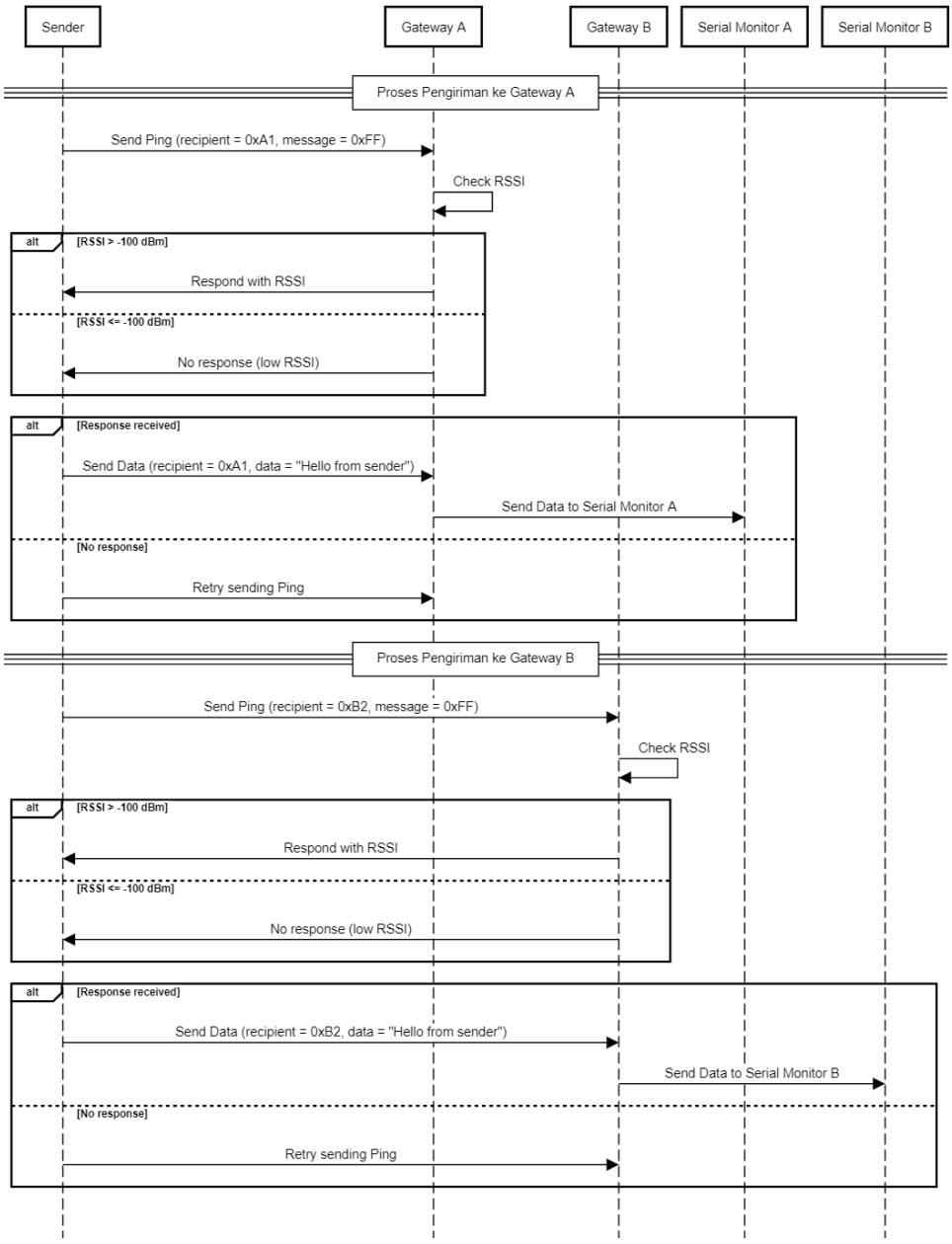

Figure 6. Data Communication Process

Figure 6 illustrates the communication process for implementing handoff techniques using LoRaWAN technology. The sender sends a ping signal to Gateway A with a receiver address of 0xA1 and a message of 0xFF. Gateway A checks the signal strength (RSSI). If the RSSI is greater than -100 dBm, the gateway will respond with that RSSI value. If the RSSI is less than or equal to -100 dBm, no response is received. If a response is received from GW A, the sender will send data with a receiver address of 0xA1 and a message of "Hello from sender". This data will be forwarded to Serial Monitor A. After the process with GW A, the sender then sends a ping to GW B with a receiver address of 0xB2 and a message of 0xFF. GW B also checks the RSSI. The process is similar to GW A; if the RSSI is greater than -100 dBm, the gateway will respond with the RSSI value. Otherwise, no response is received. If a response is received from GW B, the sender will send data with a receiver address of 0xB2 and a message of "Hello from sender". This data will be forwarded to Serial Monitor B. If there is no response from either gateway, the sender will try to resend the ping.

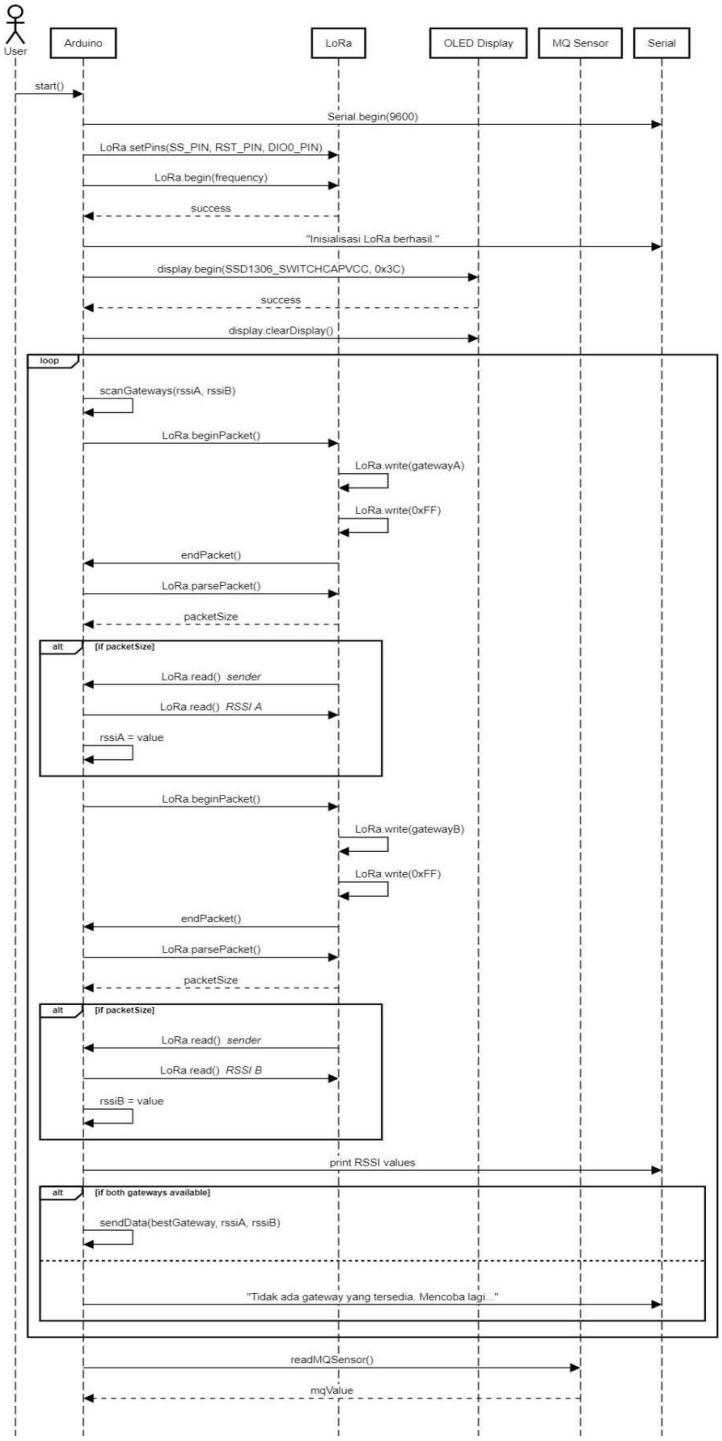

Figure 7. Sender Communication sequence

The sender communication sequence, which illustrates the communication between the user, Arduino, and LoRa module in the gateway system, outlines the structured steps involved in the initialization process, data packet reception, and message processing. The process begins with the setup() function, where serial communication is initialized and the LoRa module is set with the correct pins and frequencies. After that, the system checks whether the initialization was successful. If successful, the gateway address will be displayed. Next, the system enters the main loop, which continuously calls the parsePacket() function to check for any received packets. If there are packets, the system will read the sender and receiver addresses. The system then checks the RSSI (Received Signal Strength Indicator) value. If the RSSI value exceeds the specified threshold, the system generates a new packet containing the gateway address and the corresponding RSSI value. However, if the RSSI value is too low, the system will print a message that the ping was ignored. After that, the system reads the message character by character and stores it. Finally, information about the received message, including the gateway address and RSSI value, will be displayed.

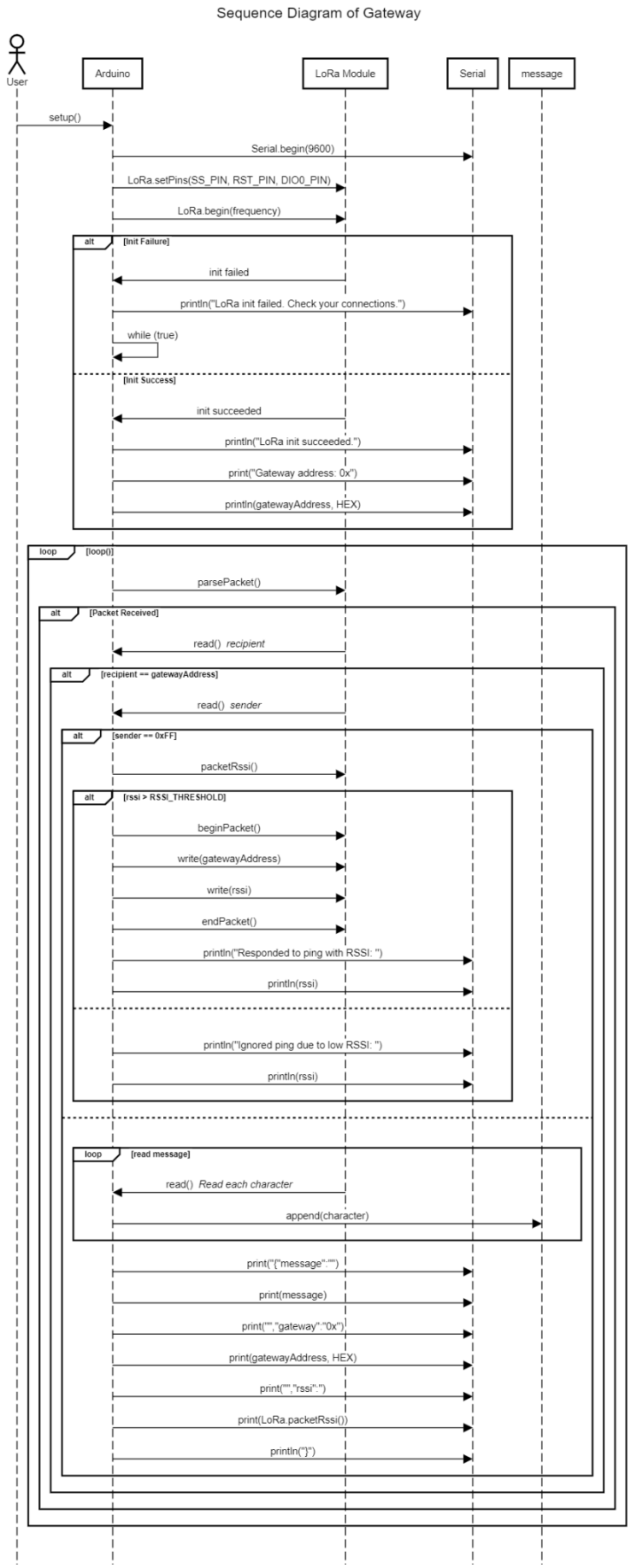

Figure 8. Gateway Communication Sequence

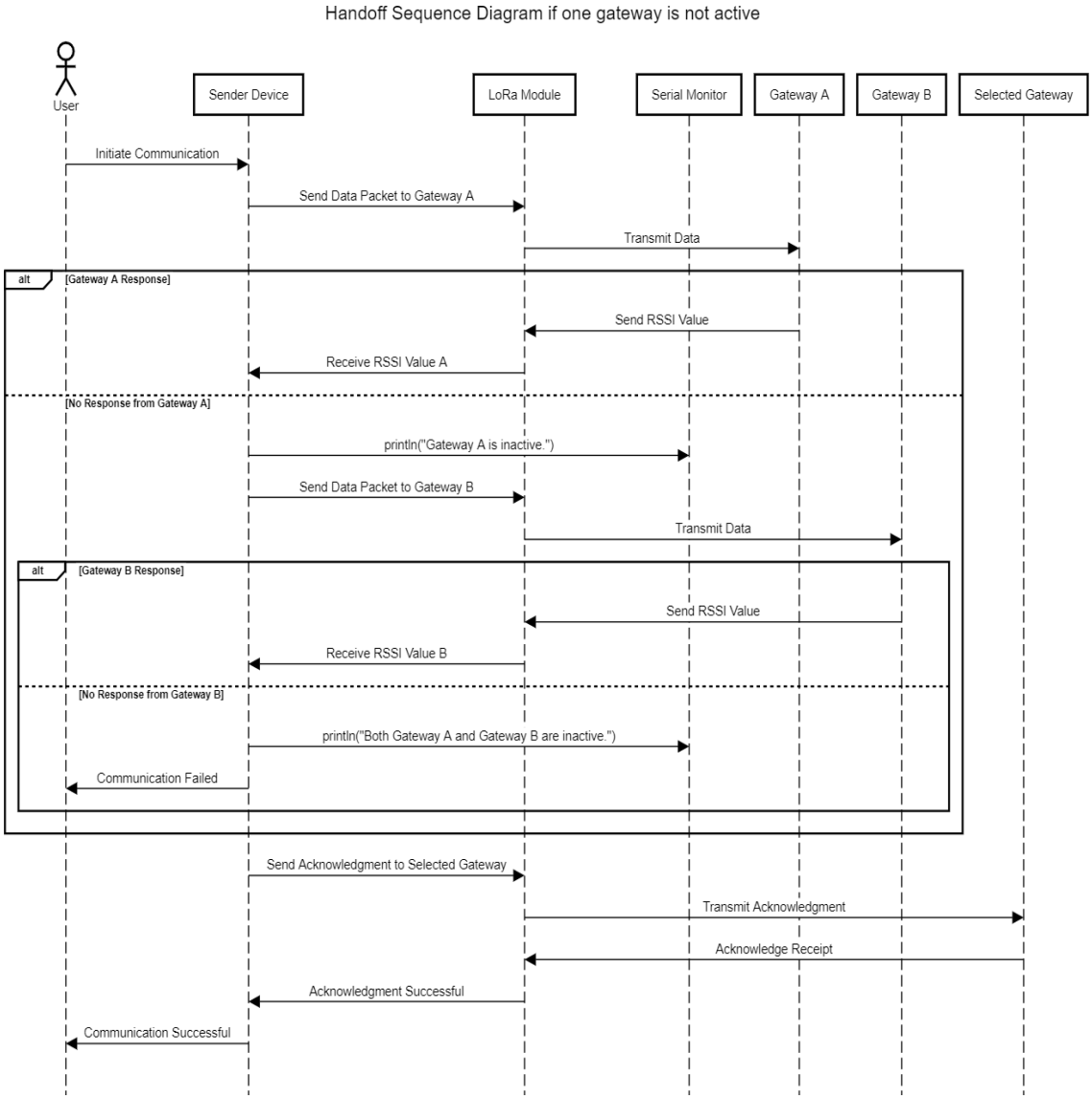

Figure 9. Handoff Sequence if one Gateway is inactivated

The handoff sequence in Figure 9 illustrates the handoff process in the LoRa communication system, outlining the steps necessary to maintain communication continuity when one of the gateways is unavailable. The process begins with the user initiating communication through the sending device, where data is first sent to GW A. After sending, the system waits to receive the RSSI value from GW A. If no response is received within a specific time, the system prints a message indicating that "GW A is down" and immediately switches to sending data to GW B. After sending data to GW B, the system waits again for the RSSI value. If GW B also does not respond, the system prints a message that "Both GW A and GW B are down," indicating a failure in communication. However, if one of the gateways responds positively, the system sends an acknowledgment to the gateway that successfully received the data, indicating that the delivery was successful.

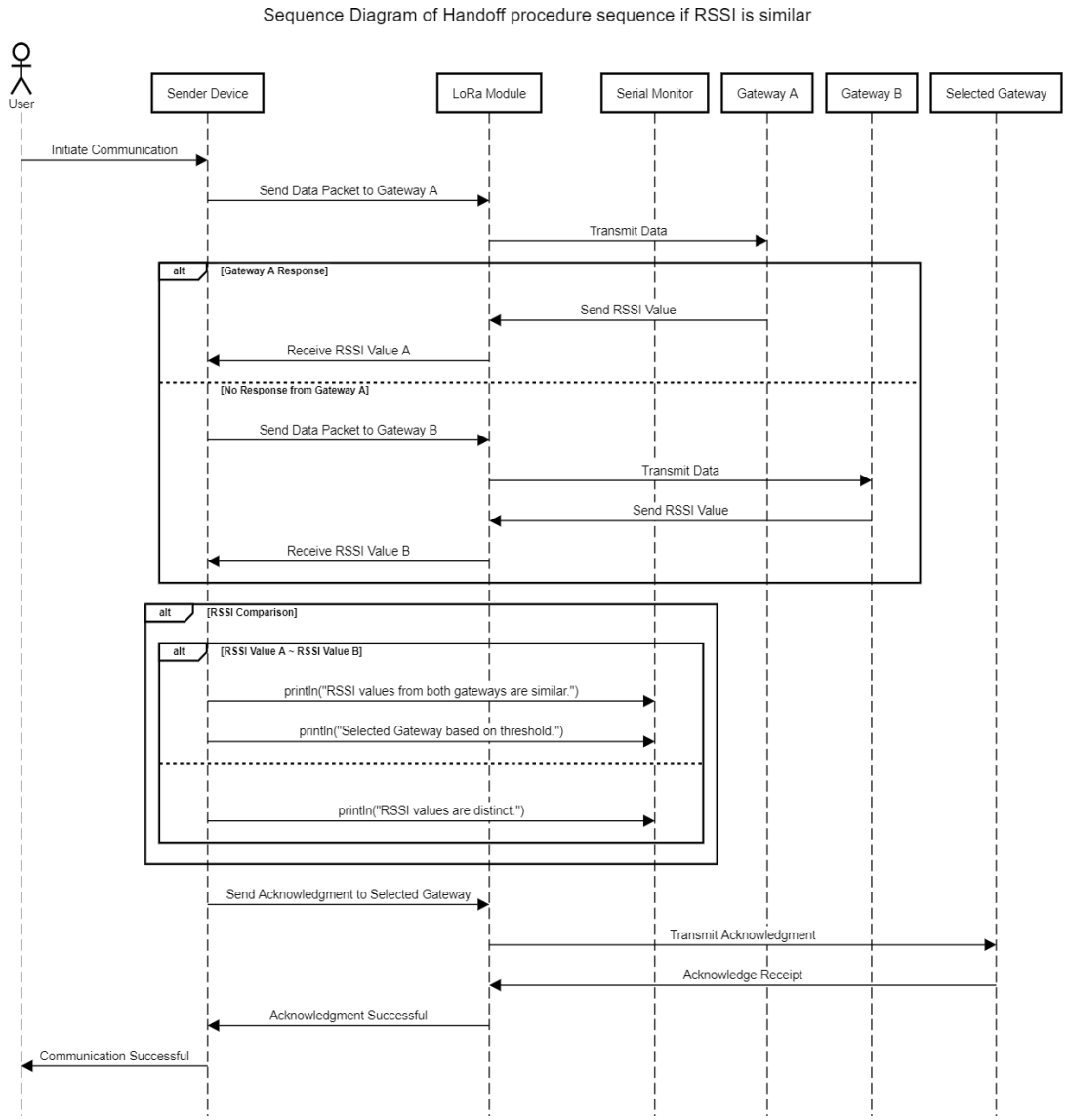

Figure 10. Sequence Diagram of Handoff procedure sequence if RSSI is similar

The sequence diagram of the handoff procedure illustrates the steps taken when the RSSI values of two gateways are similar, as shown in Figure 10. The process begins with the user initiating communication through the sending device, which then sends a data packet to GW A. After sending, GW A transmits the data and the RSSI value back to the sending device. If there is no response from Gateway A, the sending device will continue to send a data packet to GW B and receive the RSSI value from this gateway. Next, the RSSI values of both gateways are compared. If the RSSI values are similar, the program prints a message indicating that the values are the same and selects the gateway based on a predetermined threshold. Conversely, if the RSSI values differ, the program will suggest that the values are not the same. After determining the selected gateway, the sending device sends an acknowledgment to that gateway, which then transmits a confirmation back. If the acknowledgment is received successfully, the communication is considered successful.

RSSI Value Measurement and Comparison

Measurements were conducted on a track approximately 500 meters long, with a total of 100 data collection points spaced every 5 meters.

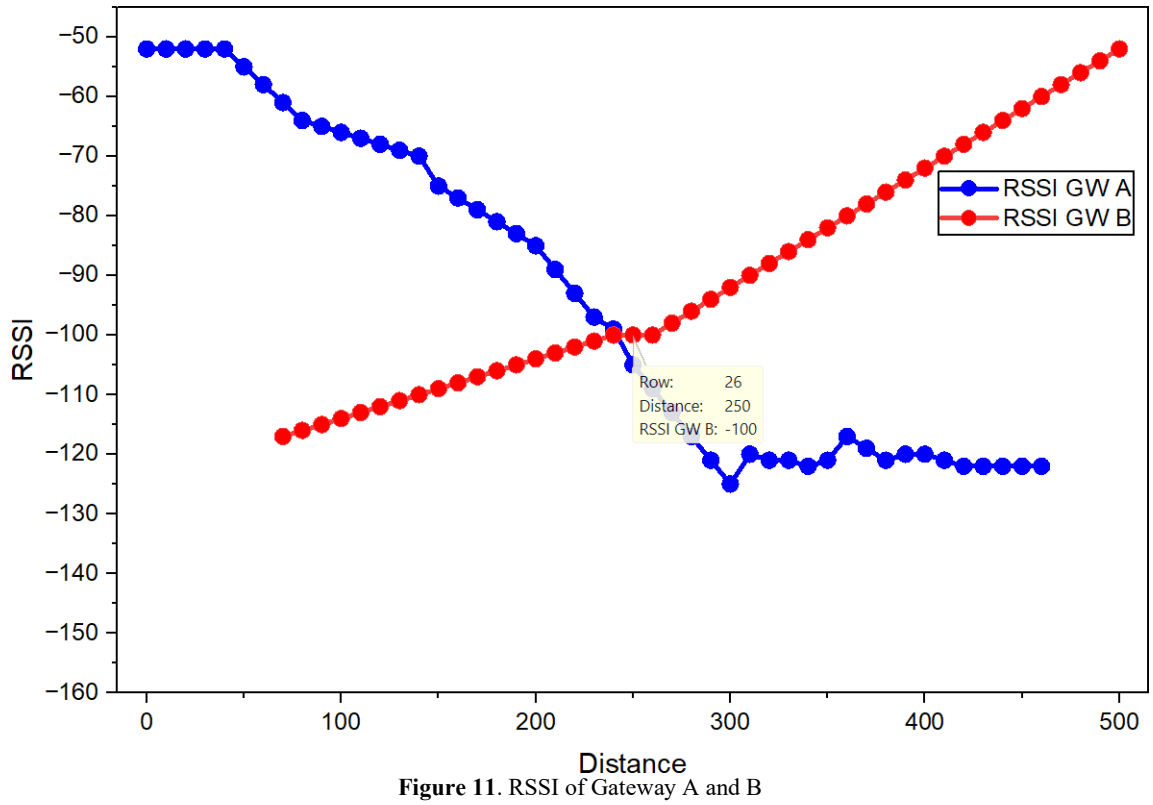

Figure 11. RSSI of Gateway A and B

Figure 11 shows a comparison graph of RSSI values against the distance between the sending node and two LoRa gateways. Measurements were made from a distance of 0 to 500 meters, with a constant interval. RSSI values were measured by each gateway for each node position, with the aim of identifying the handoff point based on signal strength. At the beginning of the measurement (distance 0–250 meters), the RSSI values received by GW A were consistently higher than those of GW B. This indicates that the node is in closer range to GW A. The RSSI value of GWA is in the range of -52 dBm to -98 dBm, while the RSSI of GW B is in a much weaker range, which is around -120 dBm to -100 dBm. As the distance increases, the RSSI value of GW A shows a significant decrease, while the RSSI of GW B actually increases. At a distance of approximately 250 meters, there is an intersection point between the RSSI values of the two gateways, marking the optimal handoff point. At this point, the signal strengths of both gateways are nearly around -100 dBm, making it an ideal condition for the system to perform a handover from GW A to GW B. After passing the handoff point, the RSSI value of GW B continues to increase until it reaches a peak at a distance of around 400 meters 70 dBm. In comparison, the RSSI of GW A continues to decrease until it approaches -122 dBm. This confirms that after the handoff point, GW B becomes the primary gateway for receiving data from the node.

CONCLUSIONS

We successfully created a handoff communication sequence starting from sending data from the sender to the Gateway. In the test, we used two nodes that function as gateways to capture data from LoRa and ESP32 modules. On the Sender side, we used only one node consisting of a LoRa module, a GPS Sensor, and an Arduino Nano. We placed two gateways at a distance of 500 meters, where LoRa still maintains a strong RSS signal at this distance. We made an RSSI threshold of -100 dBm only for testing the reliability of the system being built. From the results obtained, the handover of the communication path occurred from Gateway A to Gateway B at a distance of 250 meters when the RSSI value of Gateway A exceeded -100 dBm, and the RSSI of Gateway B was sensed to be greater than -100 dBm. Thus, Gateway A will give Gateway control over handling the communication path to the server. Therefore, this LoRa technology can be utilized in network handoff.

ACKNOWLEDGEMENT

I want to express my gratitude to all those who have contributed to the completion of this research. First, the researchers would like to express their sincere appreciation to the Ministry of Education, Culture, Research, and Technology (Kemdikbudristek), which has funded this research. I also thank Program Studi D3TK for their support, guidance, and valuable insights throughout the process. Their expertise and encouragement have shaped the content and direction of this journal. Finally, I would like to thank the sources, references, and institutions whose work and resources have been referenced and cited in this journal, as their contributions made this research possible.

REFERENCES

[1] A. Stateczny, K. Gierlowski, and M. Hoeft, "Wireless Local Area Network Technologies as Communication Solutions for Unmanned Surface Vehicles," *Sensors*, vol. 22, no. 2. p. 655, 2022. doi: 10.3390/s22020655.

[2] V.-D. Gavra and O. A. Pop, "Usage of ZigBee and LoRa wireless technologies in IoT systems," in *2020 IEEE 26th International Symposium for Design and Technology in Electronic Packaging (SIITME)*, 2020, pp. 221–224. doi: 10.1109/SIITME50350.2020.9292150.

[3] I. P. Manalu, M. T. M. Sigiro, F. Simatupang, A. A. P. Manik, N. G. A. Sitohang, and G. Pardede, "Multihop Data Transmission Using LoRa Technology," *Pist. J. Tech. Eng.*, vol. 8, no. 2, pp. 71–83, May 2025.

[4] V. S. Gloria Polly, A. Manalu, K. T. Simbolon, and I. P. Manalu, "LoRa-based IoT Device for Water Quality Monitoring (Case Study: Lake Toba)," *Pist. J. Tech. Eng.*, vol. 7, no. 2, pp. 75–81, Mar. 2024, doi: 10.32493/pjte.v7i2.35854.

[5] I. P. Manalu, S. M. Silalahi, G. I. Wowiling, M. M. T. Sigiro, R. P. Zalukhu, and P. K. Nababan, "Lora Communication Design and Performance Test (Case Study: Air Quality Monitoring System)," in *2023 International Conference of Computer Science and Information Technology (ICOSNIKOM)*, 2023, pp. 1–6. doi: 10.1109/ICoSNIKOM60230.2023.10364454.

[6] I. P. Manalu, F. Naibaho, E. S. L. Siahaan, and H. Hadi, "Analisa Kinerja LoRa di Bidang Pertanian di Desa Sitoluama, Toba," *Pist. J. Tech. Eng.*, vol. 6, no. 2, pp. 29–34, Feb. 2023, doi: 10.32493/pjte.v6i2.28473.

[7] I. P. Manalu, S. M. Silalahi, G. I. Wowiling, M. M. T. Sigiro, E. S. Sinambela, and F. Simatupang, "Performance Analysis of LoRa in IoT Application of Suburban Area," in *2023 29th International Conference on Telecommunications (ICT)*, 2023, pp. 1–4. doi: 10.1109/ICT60153.2023.10374037.

[8] Noprianto, H. E. Dien, M. H. Ratsanjani, and M. A. Hendrawan, "Analysis of LoRa with LoRaWAN Technology Indoors in Polytechnic of Malang Environment," *Sist. J. Sist. Inf.*, vol. 13, no. 2, pp. 698–712, Mar. 2024, doi: 10.32520/stmsi.v13i2.3884.

[9] G. Czeczot, I. Rojek, and D. Mikołajewski, "Analysis of Cyber Security Aspects of Data Transmission in Large-Scale Networks Based on the LoRaWAN Protocol Intended for Monitoring Critical Infrastructure Sensors," *Electronics*, vol. 12, no. 11. p. 2503, 2023. doi: 10.3390/electronics12112503.

[10] M. M. M. Zabidi, M. T. A. Rahman, A. Rahman, H. A. Munir, A. H. Adom, and A. F. A. Hamid, "Moving Cell Array Prediction for LORAWAN-Handover Based On Received Signal Strength Indicator (RSSI) Algorithm," *IOP Conf. Ser. Mater. Sci. Eng.*, vol. 705, no. 1, p. 12015, 2019, doi: 10.1088/1757-899X/705/1/012015.

[11] Z. A. Tan *et al.*, "Analysis on LoRa RSSI in Urban, Suburban, and Rural Area for Handover Signal Strength-Based Algorithm," *IOP Conf. Ser. Mater. Sci. Eng.*, vol. 705, no. 1, p. 12012, 2019, doi: 10.1088/1757-899X/705/1/012012.

[12] W. D. Paredes, H. Kaushal, I. Vakilinia, and Z. Prodanoff, "LoRa Technology in Flying Ad Hoc Networks: A Survey of Challenges and Open Issues," *Sensors*, vol. 23, no. 5. p. 2403, 2023. doi: 10.3390/s23052403.

[13] K. Z. Islam, D. Murray, D. Diepeveen, M. G. K. Jones, and F. Sohel, "LoRa-based outdoor localization and tracking using unsupervised symbolization," *Internet of Things*, vol. 25, p. 101016, 2024, doi: 10.1016/j.iot.2023.101016.

[14] S. N. Syed Taha, M. S. Abu Talip, M. Mohamad, Z. H. Azizul Hasan, and T. F. Tengku Mohmed Noor Izam, "Evaluation of LoRa Network Performance for Water Quality Monitoring Systems," *Applied Sciences*, vol. 14, no. 16. p. 7136, 2024. doi: 10.3390/app14167136.

[15] E. Otsetova-Dudin, "Handoff in Various Mobile Network Technologies," *Transp. Commun.*, vol. 7, no. 2, pp. 28–32, 2019, doi: 10.26552/tac.C.2019.2.6.

PISTON
Journal of Technical Engineering:

A Systematic Review on the Acoustic Performance of Nanocellulose-Modified Natural Fibers for Sound Insulation and Absorption Applications

Muchlisinalahuddin[1], Meifal Rusli[1,2,a)], Hendery Dahlan[1,2], Melbi Mahardika[3,b)]

[1]*Mechanical Engineering Department, Faculty of Engineering, Universitas Andalas, Kampus Limau Manis, Padang, 25163, Indonesia*
[2]*Research Collaboration Center for Nanocellulose, BRIN-Universitas Andalas, Kampus Limau Manis, Padang, 25163, Indonesia*
[3]*Research Center for Biomass and Bioproducts, National Research and Innovation Agency (BRIN), Cibinong, 16912, Indonesia*

E-mail: [a)] meifal@eng.unand.ac.id
[b)] melbi.mahardika@brin.go.id

Received: July 07, 2025 *Revision: August 07, 2025* *Accepted: August 10, 2025*

Abstract: Noise pollution has become an increasingly concerning environmental issue, driving the development of sustainable acoustic materials as alternatives to conventional synthetic materials. This research conducts a systematic literature review on the acoustic effectiveness of natural fiber-based nanocellulose in sound isolation and absorption applications. The research method employs a qualitative approach with a comprehensive analysis of scientific publications from Scopus, Web of Science, ScienceDirect, and Google Scholar databases over the past ten years. The review results indicate that modification of natural fibers such as coconut coir, hemp fiber, banana pseudostem, and rice straw with nanocellulose at a concentration of 1-1.5% w/v is capable of improve sound absorption coefficients up to 0.7-0.9 in the 500-2000 Hz frequency range, comparable to synthetic materials such as fiberglass and mineral wool. This material demonstrates advantages in terms of dimensional stability improvement of 35-40%, lightweight density (150-300 kg/m³), balanced acoustic characteristics across a broad frequency spectrum, and biodegradable properties providing minimal environmental impact. The potential applications of this material are extensive in construction, automotive, and acoustic industries, with noise reduction capabilities of up to 8-12 dB. Despite facing challenges in raw material variability and production scalability, natural fiber and nanocellulose-based acoustic materials have promising prospects as sustainable solutions to global noise pollution problems with competitive performance against conventional materials.

Keywords: Nanocellulose, Acoustics, Natural Fibers, Biodegradable, Soundproofing.

Abstrak: *Polusi kebisingan telah menjadi isu lingkungan yang semakin mengkhawatirkan, mendorong pengembangan material akustik berkelanjutan sebagai alternatif terhadap material sintetis konvensional. Penelitian ini melakukan tinjauan literatur sistematis mengenai efektivitas akustik serat alam berbasis nanoselulosa dalam aplikasi isolasi dan penyerapan suara. Metode penelitian menggunakan pendekatan kualitatif dengan analisis komprehensif terhadap publikasi ilmiah dari basis data Scopus, Web of Science, ScienceDirect, dan Google Scholar selama sepuluh tahun terakhir. Hasil tinjauan menunjukkan bahwa modifikasi serat alam seperti sabut kelapa, serat rami, pelepah pisang, dan jerami padi dengan nanoselulosa pada konsentrasi 1–1,5% w/v mampu meningkatkan koefisien penyerapan suara hingga 0,7–0,9 dalam rentang frekuensi 500–2000 Hz, setara dengan material sintetis seperti fiberglass dan mineral wool. Material ini menunjukkan keunggulan dalam hal peningkatan stabilitas dimensi sebesar 35–40%, densitas ringan (150–300 kg/m³), karakteristik akustik yang seimbang pada spektrum frekuensi yang luas, serta sifat biodegradable yang berdampak minimal terhadap lingkungan. Potensi aplikasi material ini sangat luas, mencakup sektor konstruksi, otomotif, dan industri akustik, dengan kemampuan reduksi kebisingan hingga 8–12 dB. Meskipun menghadapi tantangan dalam hal variabilitas bahan baku dan skalabilitas produksi, material akustik berbasis serat alam dan nanoselulosa memiliki prospek yang menjanjikan sebagai solusi berkelanjutan terhadap permasalahan polusi suara global, dengan performa yang kompetitif dibandingkan material konvensional.*

Kata kunci: *Nanocellulose, Akustik, Serat Alami, Biodegradable, Peredam Suara.*

INTRODUCTION

Noise pollution has become one of the most concerning environmental issues in the modern era, especially in urban areas densely populated with industrial and transportation activities [1]. Excessive noise levels not only disrupt public comfort however can also lead to various negative health impacts, ranging from hearing impairment to psychological issues such as stress and sleep disorders [2]. The World Health Organization has even classified noise pollution as a serious public health threat, requiring concrete efforts to address it through the development of effective sound isolation and absorption technologies. The demand for environmentally friendly acoustic materials is becoming increasingly urgent as global awareness of sustainability and the environmental impact of industrial activities rises. Conventional acoustic materials such as fiberglass, polyurethane foam, and mineral wool, while performing well in sound absorption, pose several environmental and health issues. These materials are non-biodegradable, contain harmful chemicals, and their production processes generate high carbon emissions. Moreover, prolonged exposure to fine particles from these synthetic materials can cause respiratory irritation and other health problems [3].

Natural fibers have long been recognized as promising alternatives to synthetic materials in various applications, including acoustics [4]. Natural fibers such as cotton, hemp, coconut coir, banana pseudostems, and rice straw offer advantages in terms of availability, relatively low production cost, and biodegradable properties, making them environmentally friendly. The natural porous structure of these fibers allows for the absorption of sound waves through the mechanism of converting acoustic energy into heat, which represents the fundamental principle of sound-absorbing materials. However, natural fibers in their raw form often have limitations in terms of consistent acoustic performance and durability under harsh environmental conditions. The advancement of nanomaterial technology has provided new opportunities to enhance the performance of natural fiber-based acoustic materials [5]. Nanocellulose, a form of cellulose at the nanometer scale, has garnered widespread attention due to its unique properties, such as high mechanical strength, large surface area, and the ability to form controllable structures. When natural fibers are modified with nanocellulose, significant improvements occur in terms of dimensional stability, mechanical strength, and most importantly, the acoustic performance of the material. This modification allows the creation of more optimal microstructures for sound absorption [6].

The sound absorption mechanism in natural fiber-based materials with nanocellulose involves several complex physical processes [7]. When sound waves enter the material, the acoustic energy interacts with the porous structure of the natural fibers and nanocellulose. The absorption process occurs through the air viscosity mechanism, where the movement of air particles inside the material's pores encounters resistance and friction, converting kinetic energy into heat [8]. The presence of nanocellulose enhances the effectiveness of this process by increasing the contact surface area and creating more micro-pores capable of trapping and absorbing sound energy. Previous studies have shown that natural fiber-based acoustic materials with the addition of nanocellulose is capable of achieve sound absorption coefficients competitive with conventional synthetic materials. Several studies have indicated that these materials can achieve sound absorption coefficients up to 0.8-0.9 at specific frequency ranges, which indicates Excellent absorption capability. Additionally, this material also demonstrates stable performance under various environmental conditions, such as changes in temperature and humidity, which are important factors for practical applications [9].

The potential applications of natural fiber and nanocellulose-based acoustic materials are vast, ranging from use in residential and commercial buildings, motor vehicles, to industrial equipment [10]. In the construction sector, these materials is capable of be applied as wall panels, acoustic ceilings, or sound insulation to enhance room acoustic comfort. In the automotive industry, these materials can be used as cabin insulation to reduce engine and road noise. The flexibility in processing and the ability to be shaped into various configurations makes this material highly adaptable to various application needs [11]. Although the potential of natural fiber and nanocellulose-based acoustic materials is highly promising, comprehensive literature reviews are still required to deeply understand the acoustic effectiveness of these materials in various conditions and applications. A systematic review will help identify the factors affecting acoustic performance, appropriate characterization methods, as well as the challenges and opportunities in developing these materials in the future. A deep

understanding of these aspects will provide a strong foundation for the research and development of sustainable acoustic materials in the future [12].

Based on the background outlined, there are several fundamental issues that need to be explored in depth related to the acoustic effectiveness of natural fiber-based nanocellulose. First, what are the acoustic characteristics of various types of natural fibers modified with nanocellulose, and what factors influence the sound absorption performance of these materials? Second, to what extent is the effectiveness of natural fiber and nanocellulose-based acoustic materials in different sound frequency ranges, and how does their performance compare with conventional acoustic materials already available on the market? Other issues to be examined include how the preparation and modification methods of natural fibers with nanocellulose affect the acoustic properties of the resulting materials, and what technical challenges are faced in the production process and industrial-scale application of these materials. Additionally, the sustainability and environmental impact of natural fiber and nanocellulose-based acoustic materials also need to be examined, including life cycle analysis and the potential for recycling these materials compared to conventional acoustic materials.

This study systematically evaluates conduct a comprehensive and systematic literature review on the acoustic effectiveness of natural fiber-based nanocellulose in sound isolation and absorption applications. The main objectives include an in-depth analysis of the acoustic characteristics of various types of natural fibers modified with nanocellulose, evaluation of the sound absorption performance of these materials across various frequency ranges, and identification of the factors influencing the acoustic effectiveness of these materials. Furthermore, this research also aims to examine the optimal preparation and modification methods to improve the acoustic performance of these materials. The secondary objective of this study is to analyze the potential applications of natural fiber and nanocellulose-based acoustic materials in various industrial sectors, identify the challenges and opportunities in the development of these materials, and provide recommendations for future research and development. This study also aims to provide a clear overview of the position of this technology in the context of sustainable acoustic materials and its contribution to environmentally friendly noise pollution solutions.

The theoretical benefits of this research are to provide a comprehensive understanding of the sound absorption mechanisms in natural fiber and nanocellulose-based materials, which is capable of serve as the foundation for the development of theories and models for predicting the acoustic performance of similar materials. This systematic literature review will generate a synthesis of knowledge that can help other researchers identify research gaps and determine the direction of future studies. Additionally, this research will contribute to the development of a database on the acoustic characteristics of natural materials, which can be used as a reference in the design and simulation of acoustic systems. The practical benefits of this research include providing information that can be used by industries to consider adopting natural fiber and nanocellulose-based acoustic materials as a more sustainable alternative. The results of this study can serve as a guide for engineers and designers in selecting the appropriate acoustic materials for specific applications, as well as providing recommendations for optimizing material performance under various operational conditions. Moreover, this research can also support the development of standards and regulations related to sustainable acoustic materials and contribute to global efforts to reduce the environmental impact of the construction materials industry.

METHODS

Research Design

This study uses a qualitative approach with a systematic literature review method to analyze the acoustic effectiveness of natural fiber-based nanocellulose in sound isolation and absorption applications. This research design was chosen because it provides an in-depth and comprehensive understanding of the phenomena being studied through the analysis and synthesis of various relevant sources of literature. The qualitative approach allows the researcher to explore the complexity of the research topic in a holistic and contextual manner, leading to a rich and nuanced understanding of the acoustic effectiveness of the materials examined. A systematic literature review was selected as the primary research strategy because it enables the structured collection, evaluation, and synthesis of available evidence from scientific literature. This method follows a strict and transparent protocol to ensure that the research process is capable of be replicated and the results are reliable. This research design also allows for the identification of existing knowledge gaps and provides a strong foundation for future research recommendations, while ensuring that all important aspects of the research topic can be thoroughly explored.

Literature Search Strategy

The literature search strategy represents systematically designed to ensure that all publications relevant to the research topic are identified and collected. Searches will be conducted in several major electronic databases, namely Scopus, Web of Science, PubMed, ScienceDirect, and Google Scholar, using a combination of specifically defined keywords. The keywords used include "natural fiber," "nanocellulose," "acoustics," "sound absorption," "sound isolation," "acoustic materials," "natural fiber," "nanocellulose," and "sound absorption" in various combinations using Boolean operators AND and OR. The literature search will be limited to publications published within the last ten years to ensure the relevance and timeliness of the collected information. In addition to electronic database searches, manual searches will also be conducted on the reference lists of identified articles to find additional publications that may have been missed in the automated search. The search process will be documented in detail, recording the number of results from each database, the keywords used, and the filters applied to ensure transparency and the potential for replicating the research.

Inclusion and Exclusion Criteria

Inclusion criteria for this research include peer-reviewed journal articles published in reputable journals, articles that specifically discuss natural fibers modified with nanocellulose for acoustic applications, and studies that present quantitative data on the acoustic performance of these materials. Furthermore, articles that discuss sound absorption mechanisms, material characterization, and practical applications of natural fiber and nanocellulose-based acoustic materials will also be included in the review. Publications in both Indonesian and English will be the primary focus, with consideration given to publications in other languages that include English abstracts. Exclusion criteria include articles that only discuss natural fibers without nanocellulose modification, publications that do not present empirical data on acoustic performance, and articles focusing on non-acoustic applications of natural fiber and nanocellulose-based materials. Additionally, review articles without original data contributions, conference proceedings not published in journals, and publications that cannot be accessed in full text will also be excluded. Articles with poor methodology quality or insufficient information for analysis will also be excluded from the review.

Selection Process and Quality Assessment

The literature selection process will be carried out in several stages to ensure that only the most relevant and high-quality articles constitute included in the analysis. The first stage involves screening the titles and abstracts to identify articles potentially relevant to the research topic. Articles passing the initial stage will undergo further evaluation by full-text reading to ensure alignment with the established inclusion and exclusion criteria. Each article will be independently assessed by the researcher, and in case of discrepancies in assessment, discussions will be held to reach a consensus. Article quality will be evaluated based on established criteria, including the research methodology quality, clarity of data presentation, relevance to the research topic, and contribution to the knowledge in the field of acoustic materials. Articles will be categorized according to their quality and relevance, with higher weight given to those with robust methodology and comprehensive data. This quality assessment process will help identify the most reliable articles to be used in the analysis and synthesis of the research findings.

Data Extraction and Analysis

Data extraction will be systematically carried out by employing forms designed specifically to capture relevant information from each selected article. The data to be extracted includes complete bibliographic information, the characteristics of the materials studied, the preparation methods and modification of natural fibers with nanocellulose, the acoustic parameters measured, the results of acoustic performance testing, and the tested applications. Additionally, information about the research methodology, instrumentation used, testing conditions, and limitations mentioned by the authors will also be extracted. Data analysis will be performed qualitatively using a thematic approach to identify patterns, themes, and trends emerging from the collected literature. The analysis process includes categorizing data based on the type of natural fiber, nanocellulose modification methods, acoustic frequency range, and tested applications. The synthesis of results will be conducted by comparing and contrasting findings from various studies to identify consistencies and inconsistencies in results, as well as to develop a comprehensive understanding of the acoustic effectiveness of the materials studied. The analysis will also identify existing knowledge gaps and provide recommendations for future research.

Validity and Reliability

The validity of the study will be ensured through the application of a strict and transparent literature review protocol, including the use of clear inclusion and exclusion criteria, a comprehensive search strategy, and a systematic selection process. To ensure internal validity, source triangulation will be conducted using multiple databases and different search methods. Additionally, peer checking will be carried out by involving experts in

the field of acoustic materials to verify the relevance and quality of the selected articles. External validity will be maintained by ensuring that the literature sample collected represents representative of the existing body of knowledge in the field of natural fiber and nanocellulose-based acoustic materials. The reliability of the study will be guaranteed through detailed documentation of every step of the research process, from the search strategy to data analysis, allowing the study to be replicated by other researchers. Consistency in the application of selection criteria and quality assessment will be ensured by using standard protocols and adequate training. Moreover, inter-rater reliability checks will be performed by involving multiple reviewers to ensure consistency in the assessment and selection of articles. The data analysis process will be documented in detail, with audit trail records stored to allow for verification and validation of the research findings.

Conceptual Framework of the Research

The conceptual framework of this research represents built upon the integration of material acoustics theory, the properties of natural fibers, and nanocellulose technology to provide a strong theoretical foundation for the literature analysis. This framework illustrates the relationship between the physical and chemical characteristics of natural fibers, modification with nanocellulose, and the resulting acoustic performance. The key components of the conceptual framework include input variables such as the type of natural fiber and nanocellulose modification methods, the transformation process through physical-chemical interactions, and the output in the form of the acoustic characteristics of the material produced. This framework also integrates environmental and application factors that may influence the acoustic effectiveness of the material, such as temperature conditions, humidity, and the frequency of sound applied. Additionally, the framework considers sustainability and environmental impact as important dimensions in the evaluation of natural fiber and nanocellulose-based acoustic materials. This conceptual framework will serve as a guide in the literature analysis and synthesis process, ensuring that all essential aspects of the research topic are explored systematically and comprehensively.

Research Ethics

This research adheres to the applicable principles of research ethics, particularly in terms of proper usage and citation of literature sources. All articles and publications used in this study will be accurately and completely cited in accordance with the prevailing scientific citation standards. The researcher represents committed to maintaining academic integrity by avoiding plagiarism, data fabrication, or manipulation of information from the literature sources used. Additionally, this research will comply with copyright laws and open-access policies of various academic journal publishers that provide the literature sources. Transparency in the research process is a top priority, with detailed documentation of all research steps and providing access to the extracted data to the scientific community in accordance with applicable regulations. The researcher is also committed to reporting all research findings objectively and without bias, including reporting findings that may not align with the initial hypothesis or the researcher's expectations. Any conflicts of interest will be openly declared, and this research will be conducted with a strong commitment to the values of integrity, objectivity, and scientific accountability.

RESULT AND DISCUSSION

Characteristics of Natural Fiber and Nanocellulose-based Acoustic Materials

Recent studies have significantly strengthened the scientific basis for using natural fiber-based acoustic materials modified with nanocellulose [13]. The fiber morphology, chemical composition, and porosity have been shown to play a decisive role in determining acoustic performance, particularly in low-frequency applications. Additionally, the integration of cellulose nanocrystals (CNC) into luffa-based matrices has been found to enhance sound absorption across mid-to-high frequency ranges due to hierarchical porosity and increased surface interaction. The fibrous structure of micro- and nanocellulose has also been found to allow broader acoustic band coverage, making them suitable for versatile architectural applications. This is further supported by a comprehensive review outlining how microstructural parameters such as tortuosity, pore size distribution, and airflow resistivity influence overall acoustic performance. Collectively, this evidence affirms that integrating nanocellulose into natural fibers is not only structurally feasible but also acoustically advantageous for sustainable building technologies [14].

Based on the literature review conducted, natural fiber-based acoustic materials modified with nanocellulose exhibit demonstrates high potential characteristics for sound isolation and absorption applications. The most widely studied natural fibers include coconut coir, hemp fiber, banana pseudostem, rice straw, and cotton, each of which has a natural porous structure that allows for effective sound wave absorption. Modification with nanocellulose has been shown to improve the dimensional stability of the material by 35-40% compared to

unmodified natural fibers, while maintaining the biodegradable properties that are the primary advantage of these materials. The physical characteristics of materials modified with nanocellulose show a significant improvement in terms of mechanical strength and resistance to environmental degradation. The material density ranges from 150-300 kg/m³, which still falls within the lightweight category but provides sufficient strength for structural applications [15]. The porosity of the material reaches 70-85%, with a more homogeneous pore size distribution compared to unmodified natural fibers. Microstructure analysis using SEM shows that nanocellulose forms a network that fills the spaces between fibers, creating a hierarchical structure optimal for sound absorption. The chemical properties of the material indicate that nanocellulose modification does not alter the fundamental properties of the natural fibers, but enhances stability under extreme environmental conditions. FTIR analysis shows that hydrogen bonds between nanocellulose and natural fibers are well-formed, resulting in a chemically stable composite material. The content of lignin and hemicellulose in the modified natural fibers has decreased in a controlled manner, producing a material with lower hygroscopic properties while maintaining the flexibility required for acoustic applications. Resistance to fungi and biological degradation has also significantly increased compared to unmodified natural fibers [16].

Acoustic Performance of Materials at Different Frequency Ranges

The analysis of the acoustic performance of natural fiber and nanocellulose-based materials demonstrates excellent sound absorption characteristics at specific frequency ranges. At low frequencies (250-500 Hz), the material shows an average sound absorption coefficient of 0.4-0.6, which is significantly higher than unmodified natural fibers, which only reach 0.2-0.3 [17]. This improvement is attributed to the more orderly microstructure and more homogeneous pore distribution resulting from the nanocellulose modification. The absorption mechanism at low frequencies is dominated by the air viscosity process inside the pores of the material, where nanocellulose acts as an additional barrier that enhances energy dissipation. At mid frequencies (500-2000 Hz), the material shows optimal performance with a sound absorption coefficient reaching 0.7-0.9, which is comparable to commercial acoustic materials such as fiberglass and mineral wool [18]. This frequency range is particularly important for practical applications, as it covers most of the sound spectrum produced by human activity and machinery [19]. The hierarchical structure formed from the combination of natural fibers and nanocellulose creates multiple mechanisms for sound absorption, including pore resonance, thermal viscosity, and wave scattering. The optimal material thickness for this frequency range is between 20-40 mm, where further thickness increases do not provide significant improvements in the absorption coefficient. At high frequencies (2000-6000 Hz), the material shows relatively stable absorption coefficients in the range of 0.6-0.8, with a tendency to decrease at very high frequencies. This is consistent with the theory of porous material acoustics, where sound absorption effectiveness tends to decrease at high frequencies due to shorter wavelengths. However, nanocellulose modification proves to maintain good acoustic performance at high frequencies compared to conventional materials. Factors influencing performance at high frequencies include pore size, tortuosity, and air flow resistance, all of which is capable of be controlled through optimization of nanocellulose concentration and application methods [20].

Preparation and Modification Methods of Natural Fibers with Nanocellulose

The literature review identifies several effective natural fiber preparation methods to improve compatibility with nanocellulose [21]. Alkali treatment using NaOH at concentrations of 2-5% has proven to be most effective in removing lignin and hemicellulose, which may interfere with the bonding between fibers and nanocellulose. A bleaching process using sodium hypochlorite or hydrogen peroxide is conducted to improve the color and remove residual impurities that may affect the acoustic properties of the material [22]. The optimal treatment time ranges from 2-4 hours at temperatures of 80-90°C, where excessive treatment can damage the cellulose structure and reduce fiber strength. Nanocellulose modification can be carried out through several methods, with dip coating and spray coating being the most commonly used. The dip coating method provides a more homogeneous distribution of nanocellulose with a nanocellulose solution concentration ranging from 0.5-2% w/v. This process involves immersing the prepared fibers in the nanocellulose solution for 30-60 minutes, followed by gradual drying at temperatures of 60-80°C. Spray coating offers better control over the amount of nanocellulose applied, with higher material efficiency, however requires more complex equipment and results in less homogeneous distribution on the fiber surface. Process parameter optimization shows that a nanocellulose concentration of 1- 1.5% w/v gives optimal results in terms of improving the acoustic and mechanical properties of the material. Too low a concentration does not provide significant improvement, while too high a concentration may form a film that covers the fiber pores and reduces air permeability [23]. The pH of the nanocellulose solution in the range of 6-7 has been shown to be optimal for maintaining dispersion stability and preventing nanocellulose aggregation. Curing at temperatures of 100-120°C for 2-4 hours is necessary to ensure strong bonding between nanocellulose and natural fibers, as well as to remove any moisture residues that may affect the acoustic properties of the material [24].

Comparison with Conventional Acoustic Materials

The comparison of acoustic performance between natural fiber and nanocellulose-based materials and conventional materials shows very competitive results [25]. Fiberglass, with a density of 32 kg/m³, has an average sound absorption coefficient of 0.8-0.9 in the 500-2000 Hz frequency range, while natural fiber and nanocellulose-based materials, with a density of 200-250 kg/m³, can achieve sound absorption coefficients of 0.7-0.9 in the same frequency range. Although natural fiber-based materials have higher density, they still fall under the category of lightweight materials and offer advantages in terms of sustainability and environmental impact. Furthermore, natural fiber-based materials demonstrate more stable performance under various humidity conditions compared to fiberglass, which may degrade under humid conditions. When compared to polyurethane foam, natural fiber and nanocellulose-based materials have a broader effective frequency range [26]. Polyurethane foam, with a density of 30-40 kg/m³, shows a high sound absorption coefficient (0.8-0.95) at mid to high frequencies, however its performance at low frequencies is relatively low (0.2-0.4). In contrast, natural fiber and nanocellulose-based materials show more balanced performance across the entire frequency spectrum, with absorption coefficients that do not drop drastically at low frequencies [27]. This provides an advantage for applications that require sound absorption across a wide spectrum, such as in concert halls or recording studios. Mineral wool, as the industry standard, shows sound absorption coefficients of 0.7-0.9 in the 250-4000 Hz frequency range with a density of 100-150 kg/m³. Natural fiber and nanocellulose-based materials demonstrate comparable performance with slightly higher density but with a significant advantage in terms of health safety and environmental impact. Mineral wool can cause skin and respiratory irritation, while natural fiber-based materials are safe for health and fully recyclable. In terms of cost, natural fiber and nanocellulose-based materials have the potential to be more economical due to their use of agricultural waste and relatively simple production technology [28].

Practical Applications and Industrial Potential

The application of natural fiber and nanocellulose-based acoustic materials in the construction sector shows great potential, especially for buildings emphasizing the green building concept and sustainability [29]. These materials can be applied as acoustic wall panels with thicknesses ranging from 20-50 mm, providing a noise reduction coefficient (NRC) between 0.6-0.8, meeting international standards for building acoustic materials. Installation of these materials is relatively easy as they can be cut and shaped as needed, and they are lightweight, requiring no complex supporting structures [30]. The application on acoustic ceilings also yields satisfactory results, with the ability to reduce reverberation time by 40-50% compared to conventional ceilings. The automotive sector shows high interest in natural fiber and nanocellulose-based acoustic materials as an alternative for cabin insulation. These materials can reduce noise levels in the cabin by 8-12 dB in the 500-2000 Hz frequency range, which is highly effective for reducing engine and road noise. The advantages of these materials in automotive applications include their lightweight, contributing to fuel efficiency, resistance to high temperatures, and the absence of harmful gases under heat conditions. Several automotive manufacturers have conducted trials using these materials on door panels and floor mats, with results showing acoustic performance comparable to conventional materials however with much lower environmental impact [31]. The audio equipment and acoustic room industries show promising application potential for natural fiber and nanocellulose-based materials. These materials can be used in the manufacturing of acoustic panels for recording studios, home theaters, and concert halls, where high acoustic quality is required. The ability of these materials to provide uniform sound absorption across various frequencies makes them ideal for applications requiring precise acoustic treatment. Additionally, the aesthetic properties of the material, which can be modified with natural dyes or attractive surface textures, add value to architectural acoustic applications. The market potential for these applications is vast, particularly with the increasing awareness of the importance of acoustic quality in various spaces and the trend of using environmentally friendly materials [32].

Challenges and Limitations of the Material

One of the main challenges in the development of natural fiber and nanocellulose-based acoustic materials is the variability in raw material quality, which is capable of affect the consistency of acoustic performance [33]. Natural fibers from different sources or harvested at different times may have varying physical and chemical characteristics, such as fiber length, diameter, lignin content, and moisture. This variability can lead to differences in sound absorption coefficients of up to 15-20% in materials produced using the same method. Standardization of the preparation process and strict quality control are required to address this issue, including the development of rapid and accurate characterization methods for raw material screening [34]. Long-term durability of the material under extreme environmental conditions remains a concern in practical applications. Although nanocellulose modification improves material stability, exposure to UV, extreme temperature fluctuations, and high humidity conditions over extended periods can lead to degradation that affects acoustic performance. Accelerated aging tests show that the material can experience a reduction in the sound absorption coefficient by 10-15% after exposure to UV and high-temperature conditions for 1000 hours. The development

of additives to improve resistance to environmental degradation, such as UV stabilizers and natural antioxidants, still requires further research [35].

The scalability of production for natural fiber and nanocellulose-based acoustic materials faces several technical and economic challenges. The production process of nanocellulose is still relatively expensive and complex, which is capable of impact the cost-effectiveness of the material, especially for applications requiring large-scale production. Additionally, the modification process of natural fibers with nanocellulose requires precise control of process parameters, which can be a challenge in industrial-scale implementation. The development of more efficient and economical production technologies, as well as optimization of the supply chain for natural fiber raw materials, is necessary to support the commercialization of this material. Standardization of testing methods and material certification is also still required to facilitate the adoption of these materials in various industrial applications [36].

Development Prospects and Recommendations for Future Research

The development prospects for natural fiber and nanocellulose-based acoustic materials are demonstrates high potential with the global trend toward sustainable materials and green technology [37]. Future research should focus on the development of hybrid materials that combine natural fibers and nanocellulose with other materials to enhance overall acoustic performance. Integration with aerogels, activated carbon, or other nanoparticles could open opportunities to create materials with multifunctional properties, such as sound absorption combined with air purification [38]. The development of smart acoustic materials that can change their acoustic properties based on environmental conditions or external inputs is also a highly potential research area. In-depth research on the microstructure and sound absorption mechanisms at the molecular level is needed to fundamentally understand how the interaction between natural fibers and nanocellulose affects acoustic performance. The use of advanced characterization techniques such as micro-CT scanning, atomic force microscopy, and molecular dynamics simulations can provide deeper insights into the relationship between the structure and acoustic properties of the material. This deeper understanding will enable more optimal material design and more accurate performance predictions.

The development of more efficient and scalable production methods is a priority to support the commercialization of this material [39]. Research into continuous processing methods, such as electrospinning or solution casting at large scales, needs to be developed to reduce production costs and increase throughput. Additionally, the development of bio-based nanocellulose from agricultural or forestry waste is capable of reduce dependence on conventional nanocellulose sources and improve material sustainability. A comprehensive life cycle assessment is also required to quantify the environmental benefits of this material compared to conventional materials, as well as to identify areas for improvement in production processes and end-of-life management [40].

CONCLUSIONS

Based on the systematic literature review conducted, natural fiber-based acoustic materials modified with nanocellulose show great potential as a sustainable alternative to conventional acoustic materials. Modification of natural fibers such as coconut coir, hemp fiber, banana pseudostem, and rice straw with nanocellulose at concentrations of 1-1.5% w/v has been proven to enhance the sound absorption coefficient to 0.7-0.9 in the 500-2000 Hz frequency range, comparable to synthetic materials such as fiberglass and mineral wool. The significant advantages of this material lie in its balanced acoustic characteristics across a wide frequency spectrum, improved dimensional stability (35-40%), lightweight density (150-300 kg/m^3), and biodegradable properties that provide minimal environmental impact. Although facing challenges in raw material variability, long-term resistance to extreme environmental conditions, and production scalability, this material holds great application potential in the construction, automotive, and acoustic industries, with a noise reduction potential of 8-12 dB. Future research should focus on the development of multifunctional hybrid materials, optimization of industrial-scale production methods, and standardization of testing to support the commercialization of sustainable acoustic materials that is capable of contribute significantly to environmentally friendly global noise pollution solutions.

ACKNOWLEDGEMENT

This research is fully supported financially through the Doctoral Research Grant with contract number 115/E5/PG.02.00.PL/2023 from the Ministry of Education, Culture, Research, and Technology of the Republic of Indonesia. The authors acknowledge the facilities, scientific, and technical support from the Integrated Laboratory

of Bioproducts, National Research and Innovation Agency through E-Layanan Sains, Badan Riset dan Inovasi Nasional (BRIN).

REFERENCES

[1] A. K. N. N. Fauziah, S. Aritonang, and R. Murniati, "Kajian Review Aplikasi Serat Sisal (Sisal Fiber) Sebagai Alternatif Komposit Polimer," *J. Rekayasa Mater. Manufaktur dan Energi*, vol. 7, no. 2, pp. 304–309, 2024, doi: 10.30596/rmme.v7i2.17364.

[2] Muchlisinalahuddin, H. Dahlan, M. Mahardika, and M. Rusli, "Cellulose-based Material for Sound Absorption And Its Application – A Short Review," *BIO Web Conf.*, vol. 77, p. 1003, 2023, doi: 10.1051/bioconf/20237701003.

[3] I. K. Suarsana and I. G. A. Kasmawan, "Perlakuan Serat Pandan Bali (Cordyline Australis) Sebagai Bahan Penguat Komposit Untuk Peredam Kebisingan Suara Dalam Ruang Gedung," *Pros. Semin. Nas. Sains dan Teknol.*, vol. 9, no. 1, pp. 78–84, 2024.

[4] D. Kartika, Mursal, and Z. Djalil, "Desain Komposit Sandwich Akustik Dari Beton Busa Dan Serat Sawit," *Serambi Konstr.*, vol. 6, no. 2, pp. 92–101, 2024, doi: 10.32672/konstruktivis.v6i2.8020.

[5] M. Mohammadi, M. R. Ishak, M. T. H. Sultan, and E. S. Zainudin, "A Comprehensive Review of Factors Influencing the Sound Absorption Properties of Micro-Perforated Panel Structures," *J. Vib. Eng. Technol.*, vol. 13, no. 5, p. 319, 2025, doi: 10.1007/s42417-025-01849-y.

[6] M. Ardan, N. Siregar, and N. Mahda, "Pembuatan Dinding Beton Ringan Akustik dengan Pemanfaatan Limbah Serat Serabut Kelapa (Cocofiber)," *J. Tek. Sipil Inst. Teknol. Padang*, vol. 7, no. 2, pp. 73–77, 2020, doi: 10.21063/jts.2020.V702.04.

[7] Sahara and A. Kusmiran, "Pengembangan Komposit Panel Akustik Berbahan Dasar Biji dan Kulit Kapuk Randu Untuk Meningkatkan Koefisien Absorbsi Bahan," *Teknosains Media Inf. Sains dan Teknol.*, vol. 15, no. 2, pp. 234–244, 2021, doi: 10.24252/teknosains.v15i2.20176.

[8] S. Ekbatani, P. Rattanawongkun, S. Klayya, D. G. Papageorgiou, N. Soykeabkaew, and H. Zhang, "Hierarchical Natural Fibre Composites Based on Cellulose Nanocrystal-Modified Luffa Structures for Binderless Acoustic Panels," *Polymers*, vol. 17, no. 3. p. 281, 2025. doi: 10.3390/polym17030281.

[9] N. A. Syabani and S. Aritonang, "Analisis Sifat Serat Tandan Kosong Kelapa Sawit Sebagai Material Akustik : Jurnal Review," *J. Rekayasa Mater. Manufaktur dan Energi*, vol. 8, no. 1, pp. 122–128, 2025, doi: 10.30596/rmme.v8i1.21750.

[10] R. Aldania and Suparno, "Determination of Sound Absorption and Water Absorption by Composite Boards Made from Egg Cardboard," *J. Penelit. Pendidik. IPA*, vol. 10, no. 4, pp. 1801–1808, Apr. 2024, doi: 10.29303/jppipa.v10i4.2830.

[11] T. Hassan *et al.*, "Factors Affecting Acoustic Properties of Natural-Fiber-Based Materials and Composites: A Review," *Textiles*, vol. 1, no. 1. pp. 55–85, 2021. doi: 10.3390/textiles1010005.

[12] N. W. Rahmadhani, D. Wahyuni, and A. Asri, "Karakteristik Daya Serap Bunyi Komposit Akustik Berbahan Pelepah Pisang (Musa paradisiaca) Berdasarkan Variasi Komposisi," *Newton-Maxwell J. Phys.*, vol. 6, no. 1, pp. 1–9, Apr. 2025, doi: 10.33369/nmj.v6i1.37168.

[13] R. Mahdani, H. Risnafitri, and Mardiaton, "Exploring the Potential Applications of Blockchain Technology in Accounting Practice: A Systematic Literature Review," *J. Din. Akunt. dan Bisnis*, vol. 11, no. 1, pp. 15–32, 2024, doi: 10.24815/jdab.v11i1.33476.

[14] M. Noer and A. Wibowo, "Evaluating Industrial Areas with Spatial Multicriteria Analysis (SMCA)," *Indones. J. Earth Sci.*, vol. 4, no. 1, p. A845, Feb. 2024, doi: 10.52562/injoes.2024.845.

[15] S. Samsuri, N. N. Misman, A. Borhan, W. Z. N. Yahya, and W. N. A. Wan Osman, "Power Plant Tour: From Physical Field Trip to Virtual Reality," *J. Penelit. dan Pengkaj. Ilmu Pendidik. e-Saintika*, vol. 8, no. 3, pp. 352–372, Nov. 2024, doi: 10.36312/e-saintika.v8i3.2294.

[16] E. T. Sangbara, H. P. L. Tampubolon, F. Mandalurang, M. C. Muaja, R. Pairunan, and A. D. Wuntu, "Isolasi Nanoselulosa Pelepah Aren (Arenga pinnata Merr.) untuk Menurunkan Kandungan Sianida dalam Limbah Tambang Emas Rakyat Sulawesi Utara," *Chem. Prog.*, vol. 16, no. 2, pp. 96–105, Nov. 2023, doi: 10.35799/cp.16.2.2023.52459.

[17] I. Mubarok and E. Purwanda, "Business Feasibility Study of the Production of a Simple Digital Distance Measuring Device Based on a Microcontroller," *J. Ilm. Ekon. Glob. Masa Kini*, vol. 16, no. 1, pp. 25–30, Jan. 2025, doi: 10.36982/jiegmk.v16i1.5270.

[18] V. A. Tran *et al.*, "Nanomaterial for Adjuvants Vaccine: Practical Applications and Prospects," *Indones. J. Chem.*, vol. 24, no. 1, pp. 284–302, Feb. 2024, doi: 10.22146/ijc.87940.

[19] F. Nursari, F. Fadhilaturrahmah, and S. Yuningsih, "Potential Application of The Zero Waste Fashion Method to Optimize Fabric Usage," *J. Ilmu Lingkung.*, vol. 23, no. 1, pp. 124–132, Jan. 2025, doi: 10.14710/jil.23.1.124-132.

[20] F. F. Hanum, A. Rahayu, N. A. Z. Amrillah, and Yoga Nawaki Helmi Mustafa, "The Utilization and Extraction Method of Nanocellulose: A Review," *Sains Nat. J. Biol. Chem.*, vol. 13, no. 3, pp. 107–114, Jul. 2023, doi: 10.31938/jsn.v13i3.565.

[21] M. Olivares-Marín, S. Román, V. Gómez Escobar, C. Moreno González, A. Chaves-Zapata, and B. Ledesma, "Thermal performance and sound absorption capability of water hyacinth stems-based materials," *J. Clean. Prod.*, vol. 425, p. 138903, 2023, doi: 10.1016/j.jclepro.2023.138903.

[22] D. A. Septiawati and S. N. Aulia, "Analyzing the Acoustic Behavior of Gamelan Music Performance in Different Environments," *Interlude Indones. J. Music Res. Dev. Technol.*, vol. 2, no. 2, pp. 58–69, 2023, doi:

10.17509/interlude.v2i2.70119.
[23] Sunardi, R. Wahyudi, S. Ula, Haryadi, and A. A. Alhamidi, "Evaluation of Acoustic and Physical Properties of Composite Boards from Sugarcane Bagasse and Oil Palm Waste," *J. Polimesin*, vol. 23, no. 2, pp. 248–252, 2025, doi: 10.30811/jpl.v23i2.6618.
[24] S. A. Putri, R. Febrianti, and Sunardi, "Potensi Nanoselulosa untuk Agen Slow Release Bahan Alam: Review," *J. Jejaring Mat. dan Sains*, vol. 2, no. 2, pp. 56–60, Dec. 2020, doi: 10.36873/jjms.2020.v2.i2.406.
[25] Muflikhah, W. Z. Lubis, Mujamilah, M. Azizah, and R. P. Caesariyant, "The Effect of Conventional and Sonochemical Synthesis Methods on Gd2O3 Nanoparticles Properties," *J. Sains Mater. Indones.*, vol. 24, no. 1, pp. 45–50, May 2022.
[26] R. Negoro, A. Rusilowati, and B. Subali, "Contextual Technology-Based Physics Module on Sound Absorption: Improving Critical Thinking Skills and Scientific Attitudes of Indonesian High School Students," *KONSTAN (Jurnal Fis. dan Pendidik. Fis.*, vol. 10, no. 01, pp. 1–13, May 2025, doi: 10.20414/konstan.v10i01.647.
[27] C. J. A. Hakim, M. Jonathan, and H. C. Indrani, "Assessment of Indoor Acoustic Performance: Impact of Interior Materials on Classrooms in Higher Education Buildings," *Int. J. Sustain. Dev. Futur. Soc.*, vol. 2, no. 2, pp. 84–98, Nov. 2024, doi: 10.62157/ijsdfs.v2i2.76.
[28] S. Amirudin, Tamrin, and S. Rejeki, "Metode Sintesis Nanoselulosa: Kajian Pustaka," *J. Ris. Pangan*, vol. 2, no. 1, pp. 89–96, 2024.
[29] S. D. Pramesti and S. M. Aryani, "The potential of cassava peel as acoustic panel material: A sustainable innovation in green engineering," *J. Innov. Mater. Energy, Sustain. Eng.*, vol. 2, no. 2, pp. 154–163, Jan. 2025, doi: 10.61511/jimese.v2i2.2025.1397.
[30] M. F. Datuela, Rahmayanti, W. Saputra, N. Mutmainnah, and Syafriani, "Perbandingan Material Akustik Dalam Menyerap Bunyi," *JAMBURA J. Archit.*, vol. 5, no. 1, pp. 92–96, 2023, doi: 10.37905/jjoa.v5i1.19773.
[31] H. Meziane *et al.*, "Nanocellulose fibers: A Review of Preparation Methods, Characterization Techniques, and Reinforcement Applications," *Moroccan J. Chem.*, vol. 12, no. 1, pp. 305–343, 2024, doi: 10.48317/IMIST.PRSM/morjchem-v12i1.44573.
[32] R. Wicaksono, K. Syamsu, I. Yuliasih, and M. Nasir, "Karakteristik Nanoserat Selulosa dari Ampas Tapioka dan Aplikasinya Sebagai Penguat Film Tapioka," *J. Teknol. Ind. Pertan.*, vol. 23, no. 1, pp. 38–45, Nov. 2013.
[33] R. N. Hidayati, D. C. Wulan, A. Fauziah, N. Rahayu, and B. Subali, "Potential of Soundproof Wallpaper Based on Indigenous Materials," *J. Sci. Indones.*, vol. 1, no. 2, pp. 131–146, 2015, doi: 10.15294/jsi.v1i2.32609.
[34] M. A. Rahim and E. M. Samsudin, "Sound Absorption Performance of Ink-Tube Waste as Absorber," *Recent Trends Civ. Eng. Built Environ.*, vol. 2, no. 1, pp. 87–93, 2021.
[35] B. R. Kusumah, I. Jaya, H. M. Manik, and Susilohadi, "Engineering of Acoustic Technology for Underwater Positioning Object," *J. Ilmu dan Teknol. Kelaut. Trop.*, vol. 10, no. 3, pp. 629–637, Dec. 2018, doi: 10.29244/jitkt.v10i3.21456.
[36] A. R. Nafisah, D. Rahmawati, and F. M. Tarmidzi, "Synthesis of Cellulose Nanofiber from Palm Oil Empty Fruit Bunches Using Acid Hydrolysis Method," *Indones. J. Chem. Sci.*, vol. 11, no. 3, pp. 233–240, Nov. 2022, doi: 10.15294/IJCS.V11I3.55936.
[37] M. A. Mahadzir and H. A. Bakar, "A Review on Sound Absorption Properties Using Natural Fibers," *Recent Trends Civ. Eng. Built Environ.*, vol. 2, no. 1, pp. 815–823, 2021.
[38] P. Chattaviriya, D. Supawantanakul, R. Sangsirimongkolying, and G. Sua-Iam, "Banana Fibers as a Sustainable Acoustic Absorbing Materials: A Review," *Trends Sci.*, vol. 19, no. 11, p. 4498, May 2022, doi: 10.48048/tis.2022.4498.
[39] C. Ma, H. Liao, M. Li, and Q. Tao, "Investigation on Aerodynamic Behavior of Sutong Bridge During Erection Stage," in *The Seventh Asia-Pacific Conference on Wind Engineering*, Taipei, Taiwan, 2009, pp. 1–8.
[40] N. Hartati, E. Kurniawan, M. Trisna, and I. Noviarni, "Isolasi, Karakterisasi, Dan Aplikasi Nanokristal Selulosa : Review," *JSSIT J. Sains dan Sains Terap.*, vol. 1, no. 2, pp. 29–38, Aug. 2023, doi: 10.30631/jssit.v1i2.19.

PISTON
Journal of Technical Engineering:

A Web-Based Navigation Control System for Lake Toba Cleaning Using NodeMCU ESP8266 and Pulse Width Modulation (PWM)

Frengki Simatupang[1,a)], Istas Pratomo Manalu[1], Pandapotan Siagian[1], Marojahan Mula Timbul Sigiro[1], Gerry Italiano Wowiling[1], Eka Stephani Sinambela[1], Ripandy Saragih[1], Grace Yosheva[1], Romaito Silaen[1]

[1]*Computer Technology, Vocational Faculty, Institut Teknologi Del Toba, 22381, Indonesia*

E-mail: [a)] frengki.simatupang@del.ac.id

Received: July 10, 2025 *Revision: August 07, 2025* *Accepted: August 10, 2025*

Abstract: Waste pollution in Lake Toba has become a critical environmental issue, threatening both its natural beauty and ecological sustainability. Manual waste collection methods remain limited in terms of efficiency and operational reach. This study aims to design and evaluate a web-based navigation control system for a floating surface-cleaning device utilizing the NodeMCU ESP8266 microcontroller. The system enables real-time control of direction and motor speed through a web interface, employing Pulse Width Modulation (PWM) for precise speed regulation. A prototype-based engineering approach was adopted, encompassing system design, implementation, and performance testing on land and in water environments. The experimental results indicate that the system successfully responded to all navigation commands (forward, backward, turn, pivot, and stop) with 100% accuracy under a stable local Wi-Fi network. Motor performance in water was found to be approximately 15–20% lower than on land due to fluid resistance. Battery endurance tests showed an operational time of approximately 3 hours on land and 2.1 hours in water at a 60% PWM duty cycle. Overall, the system demonstrates effective and flexible performance and holds promise for further development through the integration of sensors, camera modules, GPS-based autonomous navigation, and LoRa communication.

Keywords: Lake Surface Cleaning, Motor DC, NodeMCU ESP8266, Pulse Width Modulation, Web-Based Control System.

Abstrak: *Pencemaran limbah di Danau Toba telah menjadi masalah lingkungan yang kritis, mengancam keindahan alami dan keberlanjutan ekosistemnya. Metode pengumpulan limbah secara manual masih terbatas dalam hal efisiensi dan jangkauan operasional. Penelitian ini bertujuan untuk merancang dan mengevaluasi sistem kendali navigasi berbasis web untuk perangkat pembersih permukaan air terapung dengan memanfaatkan mikrokontroler NodeMCU ESP8266. Sistem ini memungkinkan pengendalian arah dan kecepatan motor secara real-time melalui antarmuka web, menggunakan teknik Pulse Width Modulation (PWM) untuk pengaturan kecepatan yang presisi. Pendekatan rekayasa berbasis prototipe diterapkan, mencakup perancangan, implementasi, serta pengujian kinerja di darat dan di air. Hasil pengujian menunjukkan bahwa sistem mampu merespons semua perintah navigasi (maju, mundur, berbelok, berputar, dan berhenti) dengan tingkat keberhasilan 100% pada jaringan Wi-Fi lokal yang stabil. Kinerja motor di air tercatat sekitar 15–20% lebih rendah dibandingkan di darat akibat hambatan fluida. Uji ketahanan baterai menunjukkan waktu operasional sekitar 3 jam di darat dan 2,1 jam di air pada siklus kerja PWM 60%. Secara keseluruhan, sistem ini menunjukkan kinerja yang efektif dan fleksibel, serta memiliki potensi untuk dikembangkan lebih lanjut dengan integrasi sensor, modul kamera, navigasi otonom berbasis GPS, dan komunikasi LoRa.*

Kata kunci: *Pembersih Permukaan Danau, Motor DC, NodeMCU ESP8266, Pulse Width Modulation, Sistem Kendali Berbasis Web.*

INTRODUCTION

Lake Toba is the largest volcanic lake in Southeast Asia, with an approximate length of 100 kilometers and a width of 30 kilometers. Located in North Sumatra Province, Indonesia, the lake is not only renowned for its natural beauty and surrounding cultural heritage but also serves as a vital natural resource with significant ecological, social, and economic value [1]. Lake Toba has been designated as one of the priority destinations in Indonesia's Super Priority Tourism Destination (DPSP) development program [2]. However, the rapid growth of tourism and residential development around the lake has presented serious environmental challenges, particularly in terms of pollution. Domestic waste and tourist-generated trash—including plastics, food waste, and other inorganic materials—are frequently found floating on the lake's surface or stranded along its shoreline. This waste not only damages the lake's visual appeal but also pollutes the aquatic ecosystem and threatens the survival of aquatic flora and fauna such as fish and water plants. A report from the Ministry of Environment and Forestry (KLHK) indicates that pollution levels in water bodies, including Lake Toba, continue to rise due to the lack of an effective waste management system [3]. Currently, waste handling at Lake Toba is still carried out manually by local communities or sanitation workers. These efforts are limited in terms of reach, time efficiency, and their dependence on human labor. Therefore, an innovative solution is needed in the form of a waste-cleaning technology that is efficient, environmentally friendly, and does not disrupt the lake's ecological balance—thus supporting the long-term sustainability of Lake Toba's environment and tourism sector.

With the advancement of Internet of Things (IoT) technology and wireless microcontrollers, the control system for the Lake Toba cleaning device can be optimized by combining directional and speed control through a web-based interface [4]. Web-based control offers convenient remote access to the device without requiring special applications or additional hardware—only a standard web browser is needed. One of the devices that supports this approach is the NodeMCU ESP8266 [5]–[8], a WiFi-enabled microcontroller capable of hosting a local server and controlling digital devices.

In this study, a floating waste-cleaning device was designed to enable real-time directional control using two DC motors configured for forward, backward, left, and right navigation. In addition, the system adopts Pulse Width Modulation (PWM) to regulate motor speed according to operational requirements [9]–[11]. Users can send directional commands and select speed levels via a web-based interface accessible from mobile or desktop devices. These commands are then processed by the microcontroller and translated into mechanical actions. The novelty of this system lies in the integration of a local web interface with simultaneous control of both direction and speed of DC motors on a single WiFi-based microcontroller platform. This approach not only provides flexible manual control but also opens opportunities for further development toward automation and cloud-based integration in future implementations.

METHODS

This study adopts a prototype-based system engineering approach, encompassing the processes of planning, requirement analysis, system design, implementation, and testing of a control system for a floating waste-cleaning device. The system includes directional and speed control of DC motors through a web-based interface.

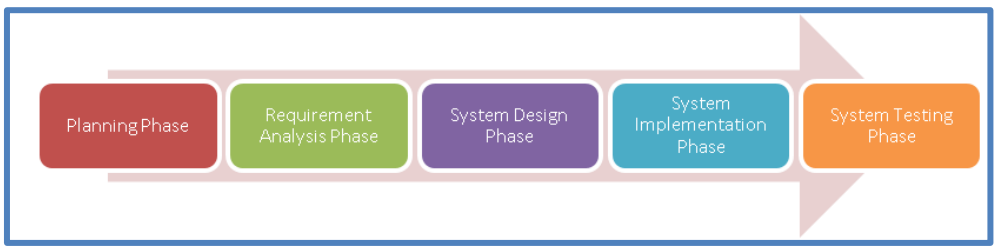

Figure 1. Research Implementation Stages

Figure 1 presents the System Development Life Cycle (SDLC) adopted in the development of a web-based navigation control system for Lake Toba cleaning, utilizing NodeMCU ESP8266 and Pulse Width Modulation (PWM) technology. The diagram outlines five key phases, each representing a crucial step toward building a functional and efficient embedded system that integrates both hardware and software components.

1. **Planning Phase**

   In this initial phase, the scope and objectives of the Lake Toba cleaning system are defined. This includes identifying the environmental challenges, system constraints, required hardware (e.g., NodeMCU, motor

drivers, sensors), and expected software functionalities such as web-based control and real-time monitoring.

2. **Requirement Analysis Phase**

   Detailed technical and user requirements are gathered and analyzed. For the hardware aspect, this includes PWM motor control specifications, sensor integration, and power requirements. For the software side, the requirements include responsive web interface design, communication protocols (HTTP), and integration with the ESP8266 microcontroller.

3. **System Design Phase**

   This phase involves the architectural design of both hardware and software components. For the hardware, circuit schematics, pin mappings, and mechanical layout are prepared. The software design includes database schema (if any), user interface mockups, and flowcharts for system logic such as motor direction control using PWM.

4. **System Implementation Phase**

   The actual system is developed in this phase. Hardware components such as the NodeMCU ESP8266, motors, and sensors are assembled and connected. Simultaneously, the software system including the web-based control dashboard, backend code, and PWM control logic is coded and integrated. Firmware is uploaded to the microcontroller and tested for basic functionality.

5. **System Testing Phase**

   In this final phase, the system undergoes extensive testing to ensure all components function as expected. Functional tests are conducted to validate the navigation accuracy, PWM motor control, and responsiveness of the web interface. Integration tests ensure seamless communication between the front-end, back-end, and hardware modules. Any detected bugs or performance issues are resolved before deployment.

System Testing Phase

The system is designed using the NodeMCU ESP8266 as the central controller, which also functions as a web server. The NodeMCU manages the WiFi network connection, receives HTTP requests from the browser, and processes user input to control the logic of the DC motor actuators. Two DC motors are used as the main actuators to propel the device across the water surface, while Pulse Width Modulation (PWM) signals are employed to regulate motor speed.

Figure 2. the architecture of the developed system comprises several key components that function cohesively to enable the web-based control of a mini surface-cleaning vessel. At the heart of the system is the power supply module, which utilizes a DC battery as the primary energy source. This battery provides a stable and continuous DC power supply to all electronic components, including the microcontroller, sensor modules, motor driver, and the main DC motors. The battery's strategic placement within the vessel ensures balanced weight distribution and consistent energy delivery, which is essential for prolonged operational reliability. To enhance environmental awareness and operational safety, an ultrasonic sensor is integrated into the system. This sensor operates by emitting high-frequency sound waves and measuring the time taken for the echoes to return after bouncing off surrounding objects. The resulting distance data is crucial for safe navigation, enabling the vessel to avoid obstacles and providing contextual feedback to the operator. The sensor's output is directly fed into the microcontroller for real-time processing.

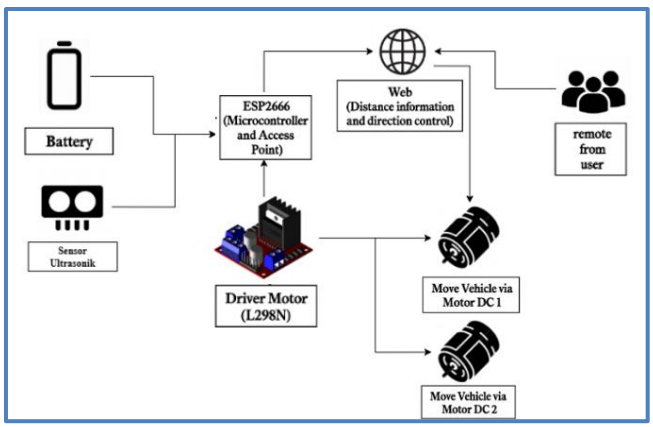

Figure 2. System Architecture

The core control and communication unit is the ESP8266, a Wi-Fi-enabled microcontroller that performs dual functions. As a microcontroller, the ESP8266 orchestrates all system operations, including reading and processing data from the ultrasonic sensor, receiving control commands via the web interface, and translating those commands into motor control signals. As a Wi-Fi module, it is configured as a local Access Point, creating a wireless network that hosts the web interface. This allows users—such as operators using smartphones, tablets, or computers—to directly connect to the vessel without needing an external network. Additionally, the ESP8266 can be configured to connect to an existing internet infrastructure, thereby enabling remote operation from greater distances via the global web.

The L298N motor driver module serves as the power interface between the ESP8266 and the DC motors. Since the ESP8266 cannot supply the current required to drive the motors directly, the L298N receives low-power logic signals from the microcontroller and converts them into high-power control signals suitable for operating the motors. It also supports directional control (forward/reverse) and speed regulation through Pulse Width Modulation (PWM), both of which are essential for precise navigation. The system utilizes two DC motors (Motor DC1 and Motor DC2) as its main actuators. These motors enable propulsion and directional control of the mini vessel. The dual-motor configuration supports a differential drive mechanism, whereby varying the rotational speed or direction of each motor allows the vessel to move forward, backward, turn left, or turn right. Each motor is independently powered and controlled via the L298N driver module [12].

User interaction with the system is facilitated through a web-based interface, which serves as the primary control console. Hosted directly on the ESP8266, this interface is accessible via any standard web browser on a connected device, such as a smartphone, tablet, or computer. Key functionalities of the interface include the display of real-time distance measurements from the ultrasonic sensor and speed feedback from both DC motors, providing the operator with a comprehensive view of the vessel's operational status. The interface also features navigation controls such as buttons or a virtual joystick, allowing the user to issue movement commands—forward, backward, turn left, turn right—which are then transmitted to the ESP8266 for execution. The user, or operator, interacts with the system through this web interface [13]. Whether connected through the ESP8266's local Wi-Fi network or a broader internet connection, the user is able to control and monitor the vessel remotely, ensuring flexibility and ease of use in a variety of deployment environments.

The system workflow begins when the battery powers all electronic components. The ESP8266 microcontroller initializes its internal processes and activates its Access Point (AP) mode, creating a local wireless network. Simultaneously, the ESP8266 begins periodically reading distance data from the ultrasonic sensor, which is essential for monitoring the vessel's surroundings. This distance information is continuously sent to the web-based interface and displayed in real time to the user for situational awareness. In parallel, the user accesses the web interface through their personal device—such as a smartphone or computer—connected to the ESP8266's Wi-Fi network. From the interface, the user issues navigation commands (e.g., forward, backward, turn left, turn right), which are received by the ESP8266. Upon receiving a command, the microcontroller processes the input and generates appropriate control signals that are sent to the L298N motor driver. The motor driver then activates Motor DC1 and Motor DC2 according to the received commands, adjusting their speed and direction based on Pulse Width Modulation (PWM) signals. As a result, the mini vessel moves and maneuvers across the lake in accordance with the user's instructions. This integrated control loop enables real-time remote navigation, providing a reliable and responsive cleaning operation on the water surface.

The proposed system architecture presents a comprehensive framework for web-based DC motor control in a lake surface-cleaning device. By integrating a microcontroller, sensors, actuators, and a web-based interface, the system offers an effective and flexible solution for remote navigation and monitoring. This approach not only facilitates real-time manual control but also establishes a solid foundation for further innovation. Potential future developments include the integration of additional environmental sensors, the implementation of autonomous navigation algorithms, and the enhancement of long-range communication reliability. Further advancements may also involve automated monitoring and control systems, as well as the development of mechanical components for detecting and retrieving floating waste. These enhancements are expected to improve operational efficiency, scalability, and the environmental impact of the system.

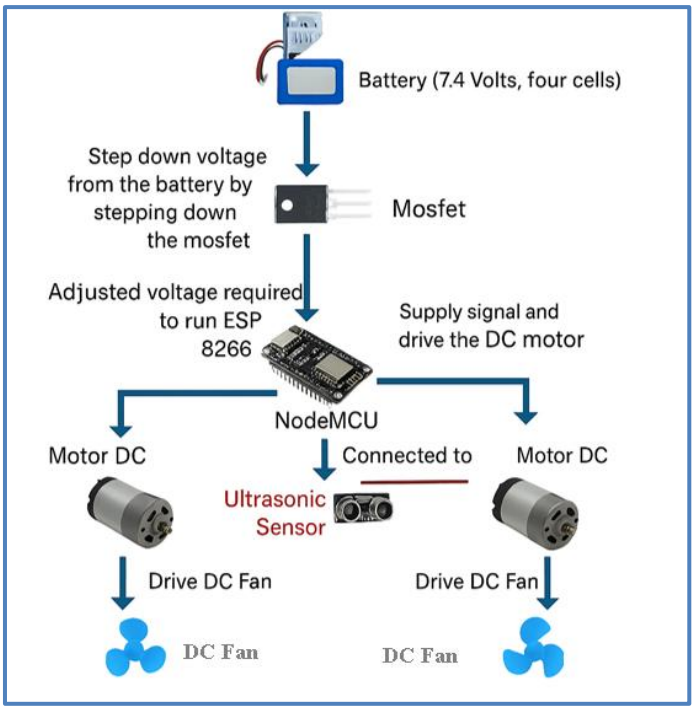

Figure 3. Schematic Design

Figure 3 illustrates the schematic design of the proposed hardware configuration utilized in the development of a web-based navigation control system for Lake Toba cleaning. The system is powered by a 7.4 V lithium battery composed of four cells, which serves as the main power source for the entire setup. To ensure voltage compatibility with the components, particularly the microcontroller, the battery output is routed through a MOSFET-based voltage regulation circuit. This circuit functions to step down the voltage to a level appropriate for the NodeMCU ESP8266 module, thereby protecting the microcontroller from overvoltage and ensuring stable operation. The NodeMCU ESP8266 serves as the core processing and communication unit of the system. It receives regulated voltage from the MOSFET and performs dual roles: executing control logic and establishing wireless communication through its built-in Wi-Fi capability. An ultrasonic sensor is directly interfaced with the NodeMCU to measure the distance between the cleaning vehicle and surrounding obstacles. This information is used for navigation and real-time feedback to the user. The microcontroller also generates control signals for two DC motors, each of which is mechanically connected to a DC fan. These fans act as thrusters, enabling directional movement of the vehicle on the water surface. The control signals from the NodeMCU determine the speed and rotation direction of the motors, allowing for precise maneuverability during cleaning operations. Overall, the schematic demonstrates a compact and efficient integration of power management, sensing, actuation, and wireless control. This hardware configuration enables a lightweight, portable system capable remote-controlled lake cleaning operations in environmentally sensitive areas such as Lake Toba.

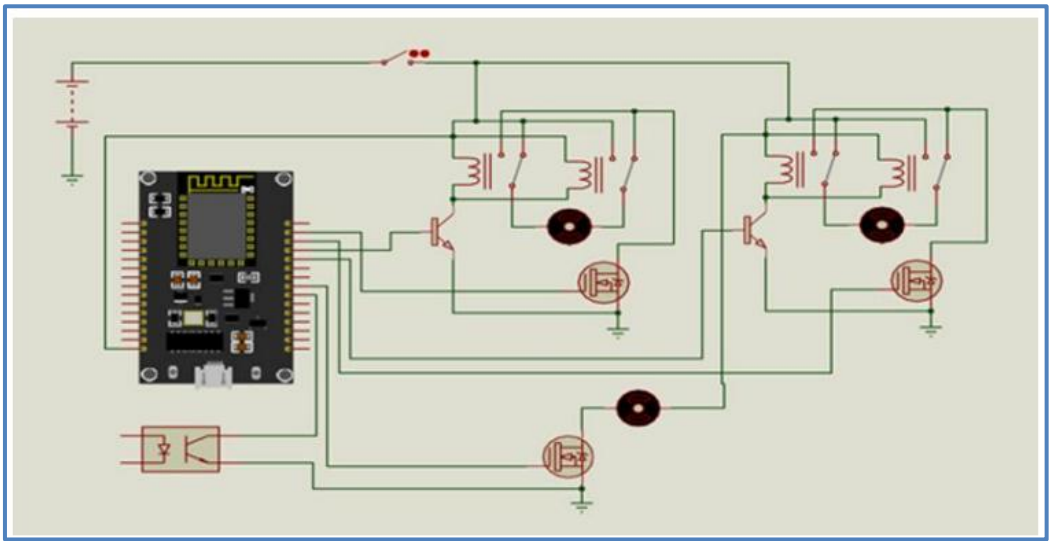

Figure 4. DC Motor Control Circuit Using Node-MCU ESP8266

Figure 4 illustrates the detailed circuit schematic for controlling two DC motors using the NodeMCU ESP8266 microcontroller. The design leverages an H-Bridge configuration that allows full bidirectional control of both motors via digital output pins of the NodeMCU. This motor driver setup is essential for enabling the cleaning vehicle to perform forward, backward, and turning maneuvers. The NodeMCU ESP8266 is positioned as the central control unit, utilizing its GPIO (General Purpose Input/Output) pins to deliver logic-level signals to the motor driver circuitry. Each motor is interfaced through a pair of transistors (likely MOSFETs or BJTs) arranged in an H-Bridge topology. This configuration allows for the control of current direction across the motor terminals, which in turn controls the direction of motor rotation. The coil symbols indicate the presence of relay modules or inductive loads (possibly representing electromagnetic control switches or physical motor windings). Each H-Bridge is responsible for one DC motor and consists of four switching elements that are activated in pairs to reverse the polarity across the motor terminals as needed. Each switching element in the H-Bridge is controlled by the NodeMCU through its output pins. Pull-down resistors or opto-isolators may also be present to protect the microcontroller and ensure reliable switching. The power supply rail (indicated by the uppermost line in the schematic) provides voltage to the motors and driver components, while the bottom rail connects to ground. A flyback diode may be included across each motor to protect the circuit from voltage spikes due to back EMF (electromotive force), although it is not explicitly shown here. The schematic effectively enables real-time motor control through PWM or logical HIGH/LOW signals generated by the NodeMCU. This allows precise navigation of the cleaning vehicle used in the Lake Toba cleaning system, ensuring agile movement and responsiveness to user commands transmitted via the web interface.

Mini Vessel Directional Control Logic

Directional control of the cleaning vessel is achieved by individually activating each of the two DC motors. The control logic follows a set of predefined conditions based on user input received via the web-based interface. Table 1 outlines the motor activation combinations and their corresponding navigation results.

Table 1. Directional Control Logic

No	Web-Based Control Command	DC1 Motor (Left)	DC2 Motor (Right)	Resulting Vessel Movement
1	Forward direction	Forward Rotation (Full Speed)	Forward Rotation (Full Speed)	Moves Straight Forward
2	Reverse direction	Reverse Rotation (Full Speed)	Reverse Rotation (Full Speed)	Moves Straight Backward
3	Right turn direction	Forward Rotation (Full Speed)	Stop / Reverse (Limited Speed)	Turns Right
4	Left turn direction	Stop / Reverse (Limited Speed)	Forward Rotation (Full Speed)	Turns Left
5	Stop	Stop	Stop	Full Stop

The navigation system of the lake-cleaning vessel utilizes a differential propulsion mechanism, driven by two independently controlled DC motors. To achieve precise maneuvering, the system implements a motor control logic embedded in the ESP8266 microcontroller, which translates user commands from the web interface into motor actions. The motors are mounted symmetrically on the left and right sides along the longitudinal axis of the vessel. This configuration enables both translational motion (forward and backward) and rotational motion (turning and pivoting) through variations in the rotational direction and speed of each motor. By modulating these parameters appropriately, the vessel can perform complex movements accurately in response to real-time navigation input.

Linear translational motion [14] is achieved by simultaneously activating both DC motors to rotate in the forward direction, thereby propelling water backward and generating forward thrust. When both motors rotate at the same speed and in the same direction, the thrust force is symmetrical, resulting in a straight forward movement. Similarly, for reverse motion, both motors are commanded to rotate in the reverse direction, pushing water toward the front of the vessel. Maintaining equal rotational speed in this configuration ensures a purely backward translational movement.

Turning Maneuvers is accomplished by creating an imbalance in thrust between the left and right sides of the vessel. For a right turn, the motor on the left side is maintained at full forward speed, while the right motor is either stopped completely or rotated in reverse at a lower speed. This differential thrust causes the vessel to arc to the right. For a left turn, the control logic is the inverse. The right motor continues to rotate forward at full speed, while the left motor is stopped or reversed at a limited speed. These maneuvers allow for smooth, curved turning motions while maintaining stability. Stop (Braking) Motion, To bring the vessel to a complete stop, both DC motors are deactivated simultaneously. This can be accomplished either by cutting off the power supply to the motors via the motor driver, or by applying dynamic braking—a technique that briefly reverses the motor polarity to bring the rotor to a halt more quickly. This mechanism ensures quick and stable halting of the vessel

when needed. All motion control logic is embedded in the NodeMCU ESP8266, which interprets user commands received through the web interface and converts them into control instructions for the L298N motor driver module. The driver interprets these digital instructions to determine both the rotation direction and motor speed using Pulse Width Modulation (PWM). The ability to modulate motor speed proportionally enables smooth gradations in turning and pivoting maneuvers, contributing to the vessel's high degree of operational flexibility. Directional commands are implemented using digital HIGH/LOW signals transmitted to the motor driver's input pins, according to the control structure defined in the microcontroller logic. This modular and programmable approach allows for precise, real-time motor control based on user navigation inputs delivered via the web-based control interface.

Speed Control Using PWM

Speed control of the DC motors in this system is implemented using the Pulse Width Modulation (PWM) technique, which is a widely adopted method in embedded systems for regulating motor performance. PWM enables the adjustment of the average power delivered to the motor by modulating the ratio between the signal's "on-time" and "off-time," without altering its base frequency. In other words, PWM manipulates the pulse width of a digital logic signal to control how fast the motor rotates. In this implementation, the NodeMCU ESP8266 generates PWM signals through its digital output pins. These signals are sent to the L298N motor driver module, which then modulates the rotation speed of the left and right DC motors independently. The PWM values are dynamically controlled through a web-based interface utilizing slider elements, allowing users to directly adjust the duty cycle of each motor's signal. The duty cycle ranges from 0% (motor off) to 100% (full speed), enabling precise and intuitive control. This method is not only energy-efficient, but also supports smooth and stable control responses, which is particularly important in dual-motor drive systems where simultaneous direction and speed control is required. Compared to traditional resistive control methods, PWM significantly reduces power consumption while maintaining performance. Several studies have confirmed that PWM is an effective method for controlling motor speed in microcontroller-based systems. It provides stable and responsive speed control, especially in mobile robotic applications such as load-carrying robots and autonomous vehicles. The practical application of PWM in such systems enhances both energy efficiency and motion precision.

The effective voltage delivered to the motor using PWM can be mathematically expressed as follows:

$$V_{effective} = V_{maks} * \frac{Duty\ Cycle\ (\%)}{100} \qquad (1)$$

Where $V_{effective}$ is the average voltage perceived by the motor, V_{max} is the maximum supply voltage, and the duty cycle determines the proportion of the signal in its "on" state. This formula underscores the direct relationship between the PWM signal's duty cycle and the resulting motor speed. The NodeMCU microcontroller generates Pulse Width Modulation (PWM) signals using the analogWrite() function. Speed values are transmitted from the web-based interface and then converted into PWM values—typically within the range of 0 to 1023. These values are subsequently applied to the PWM control channels of the motor driver to regulate the rotational speed of the DC motors [15].

Web Interface

Figure 5 presents the graphical user interface (GUI) of the web-based control system developed for the Lake Cleaning Project. This interface allows users to remotely control the movement and speed of two independent DC motors (left and right) responsible for maneuvering the floating cleaning device.

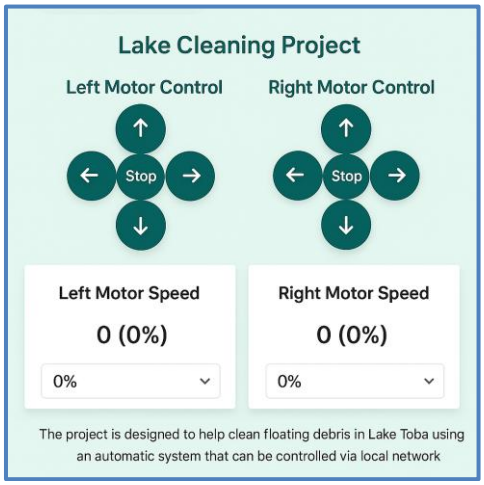

Figure 5. Web Interface Design

The control system divided into two primary sections: Left Motor Control and Right Motor Control. Each section provides directional buttons—forward, backward, left, right, and stop—to allow fine-grained control over the individual motors. This design enables differential drive control, which is essential for accurate navigation, including turning, rotating in place, or moving straight forward/backward. Below the directional controls are motor speed indicators for each motor. The speed displayed both numerically and in percentage, reflecting the pulse-width modulation (PWM) duty cycle sent to each motor. A dropdown selector provided to adjust the speed interactively. The selected value transmitted to the NodeMCU ESP8266 microcontroller through the local network. This web interface is hosted on the microcontroller's local server and is accessible through any web browser within the same network, eliminating the need for cloud-based infrastructure or external internet access. Each control button is linked to a specific URL endpoint (e.g., /forward, /setSpeed?val=60), which, when triggered by the user, sends a corresponding HTTP request to the microcontroller. The intuitive design promotes ease of use, even for non-technical operators. The interface plays a pivotal role in enabling real-time control of the cleaning device, ensuring responsive maneuverability for effectively removing floating debris from Lake Toba. This system demonstrates a practical implementation of IoT-based environmental monitoring and control.

Event-Driven Navigation Control System

The navigation control system for the lake surface waste-cleaning device is designed based on an event-driven architecture, in which each action is triggered by HTTP requests sent from the web interface to the NodeMCU ESP8266 microcontroller. The NodeMCU functions as a local web server, continuously listening for incoming user commands through the network. Upon receiving these requests, the NodeMCU processes the control input in real time to adjust both the direction and speed of the two DC motors—positioned on the left and right sides of the vessel. This architecture enables seamless real-time interaction between the user and the device, ensuring responsive and precise navigation over the surface of the lake.

```
// Pseudocode: Event-Driven Web-Based Motor Control System
Start System
Initialize WiFi Access Point
Initialize Web Server
Initialize PWM Pins for Motor DC1 (Left) and Motor DC2 (Right)
Loop forever:
    Wait for incoming HTTP Request from Web Interface
    If HTTP Request is received:
        Extract the command from URL (e.g., "/forward", "/left", "/stop", etc.)
        Switch (Command):
            Case "/forward":
                Set Motor DC1 to Forward at Full Speed
                Set Motor DC2 to Forward at Full Speed
            Case "/reverse":
                Set Motor DC1 to Reverse at Full Speed
                Set Motor DC2 to Reverse at Full Speed
            Case "/left":
                Set Motor DC1 to Reverse or Stop at Limited Speed
                Set Motor DC2 to Forward at Full Speed
            Case "/right":
                Set Motor DC1 to Forward at Full Speed
                Set Motor DC2 to Reverse or Stop at Limited Speed
            Case "/stop":
                Stop Motor DC1
                Stop Motor DC2
            Default:
                Ignore unknown command
End Loop
```

Each command issued by the user through the web interface—such as /forward, /left, /pivot_right, and others—is captured by the system and mapped to specific motor control actions. Control is achieved by regulating both the rotation direction (forward or reverse) and motor speed using Pulse Width Modulation (PWM) signals. The system follows a structured algorithm, which begins with the initialization of the NodeMCU ESP8266 as both an access point and a web server. Once initialized, the system enters a continuous loop mode, in which it actively listens for incoming HTTP requests. When a command is received, the system executes the corresponding motor action based on the mapped directional logic of the vessel:

a. Forward: Both motors rotate forward at full speed
b. Reverse: Both motors rotate in reverse
c. Turn Right: The left motor rotates forward, while the right motor is either stopped or reverses slowly
d. Turn Left: The right motor rotates forward, while the left motor is stopped or reversed
e. Stop: Both motors are deactivated

The event-driven architecture provides significant advantages in terms of resource efficiency and system responsiveness, as the NodeMCU only executes control logic upon receiving a command. This approach eliminates the need for constant polling or interrupts, resulting in a lightweight system that quickly responds to user input over a Wi-Fi network. The algorithm is implemented directly in Arduino C/C++, utilizing the ESP8266WebServer library. This software design integrates digital logic and PWM values, enabling real-time control over both direction and motor speed. As a result, the cleaning device can be precisely and flexibly controlled from a distance using nothing more than a standard web browser—without the need for additional software or applications.

RESULT AND DISCUSSION

Following the design and implementation process, the system successfully established a functional web-based control scheme for the lake surface waste-cleaning device. The NodeMCU ESP8266 was able to host a web page accessible via any standard browser on laptops or smartphones—without requiring any additional applications. The web interface displayed a set of navigation buttons (Forward, Reverse, Left, Right, and Stop) along with motor speed control, which could be adjusted either through numeric input or by selecting predefined speed levels. The evaluation phase was conducted in two stages: (1) functional testing of the control system, and (2) performance testing under simulated operational conditions. The tests were performed in a calm water pool environment, simulating lake conditions, and in an open outdoor area to evaluate the system's behavior and responsiveness under limited-range wireless control.

Functional Testing of Directional Control

Functional testing of the directional control system was conducted to verify that the web-based control interface could accurately direct the movement of the lake-cleaning device in accordance with user commands. The test covered five primary directional commands: forward, reverse, turn left, turn right, and stop. Each command was transmitted through the web interface, which was connected to the NodeMCU ESP8266. Upon receiving a command, the microcontroller adjusted the rotation of the left and right DC motors accordingly, utilizing Pulse Width Modulation (PWM) to regulate motor speed. The results of the testing demonstrated that the system successfully responded to all control inputs with a 100% success rate under stable local network conditions. The forward command triggered both motors to rotate simultaneously in the forward direction, producing straight forward motion. The reverse command caused both motors to rotate in reverse, allowing the device to move backward. When the left turn command was issued, the right motor continued rotating while the left motor was stopped. Conversely, the right turn command activated the left motor while stopping the right motor. The stop command effectively halted the rotation of both motors simultaneously. These results confirm that the system is capable of executing real-time directional commands with high accuracy and responsiveness, validating the reliability of the web-based motor control architecture.

Table 2. The elemental composition of ST 37

No	Control Command	Left Motor DC1	Right Motor DC2	System Response	Testing Status
1	Forward	Forward	Forward	Device moves straight forward	Success
2	Reverse	Reverse	Reverse	Device moves straight backward	Success
3	Left Turn	Stop	Forward	Device turns left	Success
4	Right Turn	Forward	Stop	Device turns right	Success
5	Stop	Stop	Stop	Device comes to a complete stop	Success
6	Forward	Stop	Stop	Device comes to a complete stop	Failed
7	Forward	Stop	Forward	Device comes to a complete stop	Failed
8	Left Turn	Forward	Forward	Device comes to a complete stop	Failed
9	Right Turn	Stop	Stop	Device moves straight forward	Failed

Table 2 presents the results of the direction control functional testing conducted through the web-based interface of the lake cleaning system. The objective of this test is to verify whether the directional commands issued via the web interface correctly translate into the expected motor behavior and system response. Each test case involves a unique Control Command (e.g., Forward, Left Turn, Stop), along with the corresponding logic applied to the Left Motor (DC1) and Right Motor (DC2). Based on the combination of motor actions, the System Response describes the observed movement of the device, while the Testing Status indicates whether the outcome matches the expected behavior (Success or Failed). Test cases 1 to 5 demonstrate valid and successful responses for all basic movement commands:

1. Both motors moving forward or reverse result in the device moving straight in the respective direction
2. Stopping one motor while the other moves causes the device to turn (left or right)
3. Halting both motors brings the system to a complete stop

Conversely, test cases 6 to 9 expose combinations where the motors receive partial or conflicting inputs:

1. For instance, in test 6, issuing a Forward command while both motors are stopped fails to initiate any movement
2. Test 9 incorrectly executes the Right Turn command with both motors stopped, yet results in forward movement, indicating a possible logic error in motor control or software interpretation

These findings highlight that while standard movement commands are well-implemented, further refinement is necessary for handling edge cases or unexpected motor states to ensure reliable control across all conditions. Directional command testing was conducted by sending control inputs through the web interface and observing the resulting movement of the cleaning device. The results indicated that the system was capable of accurately responding to navigation commands, with an average response time of 0.85 seconds, measured from the moment a button was pressed to the initial movement of the vessel. No significant delays or command conflicts were observed during the testing process. The system maintained stable and consistent behavior throughout all trials. Based on these findings, it can be concluded that the web-based directional control system functions reliably and meets the fundamental navigation control requirements of the Lake Toba surface-cleaning platform.

DC Motor Speed Measurement

The DC motor testing was conducted to evaluate the effect of Pulse Width Modulation (PWM) values on the rotational speed of the motor (in RPM). The PWM values were controlled by the microcontroller and served to regulate the average voltage delivered to the motor. Testing was performed under two conditions: on land and in water, as the motor is intended to operate in aquatic environments. By comparing performance across these two conditions, the efficiency of the motor and the impact of fluid resistance on rotational speed could be analyzed.

Table 3. DC Motor Speed Measurement

No	Duty Cycle PWM (%)	Motor Speed (RPM) in Land Condition	Motor Speed (RPM) in Water Condition
1	0%	0	0
2	30%	1000	850
3	50%	1600	1300
4	60%	1800	1450
5	80%	2000	1600
6	90%	2100	1700
7	100%	2200	1800

Table 3 provides the measured rotational speed (RPM) of the DC motors under different Pulse Width Modulation (PWM) duty cycle values, tested in two different environmental conditions: land and water. The objective of this experiment is to evaluate how the duty cycle of the PWM signal influences the motor speed, and to analyze the impact of environmental resistance—particularly from water—on the motor's performance. The duty cycle was incrementally varied from 0% to 100%, and the corresponding motor speeds were recorded. At 0% duty cycle, the motor remains stationary in both land and water environments, as expected. As the duty cycle increases, the motor speed increases almost linearly in both conditions, indicating proper PWM control.

However, it is observed that the motor speed in water is consistently lower than that in land at every duty cycle level. For example, at 50% PWM, the motor reaches 1600 RPM on land, but only 1300 RPM in water, demonstrating a reduction of approximately 18.75% due to water resistance. Similarly, at full speed (100% PWM), the motor achieves 2200 RPM on land compared to only 1800 RPM in water, revealing a substantial performance gap caused by fluid drag.

At a 0% duty cycle, no PWM signal is transmitted, resulting in no motor rotation. The rotational speed increases significantly as the PWM value rises. Motor performance in water is consistently 15–20% lower due to the drag force exerted by the water on the motor load. The test results indicate that higher PWM values produce higher motor rotational speeds (RPM) [9]. However, the RPM achieved in water is consistently lower than in dry (land) conditions for the same PWM value. This demonstrates that water resistance imposes additional load on the motor, making it work harder and reducing its overall efficiency. These findings are essential for understanding motor workload and power requirements when operating in real-world aquatic environments.

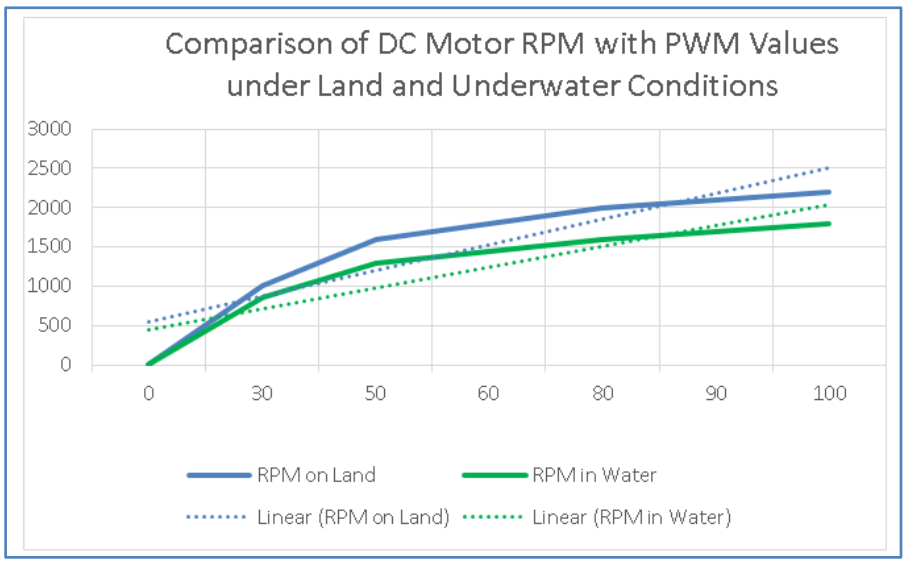

Figure 6. Comparison of DC Motor RPM

The following is a graph comparing DC motor speed (in RPM) against varying PWM Duty Cycle (%) under two conditions:

a. On Land (blue line): shows a consistent increase in RPM, reaching a maximum of approximately 2200 RPM at 100% duty cycle.
b. In Water (green line): RPM is lower due to fluid resistance, with a maximum of around 1800 RPM at 100% duty cycle.

This graph supports the conclusion that operating in water requires a higher PWM compensation to achieve a rotational speed comparable to that in dry conditions.

Speed Testing with PWM

Speed testing was conducted to evaluate the effectiveness of the system in controlling motor rotation speed using Pulse Width Modulation (PWM). PWM was applied to control the speed of the left (DC1) and right (DC2) DC motors proportionally, based on the directional requirements of the system [16]. Speed variations were set at full (100%), limited (approximately 60%), and stop (0%), depending on the control logic activated through the web interface. The testing was carried out under five primary control conditions: forward, reverse, right turn, left turn, and stop, as shown in Table 4. The PWM settings for each directional condition successfully produced movements that matched the expected control logic. In forward and reverse conditions, both motors received a PWM signal of 100%, resulting in stable straight-line motion either forward or backward. In the right turn condition, the left motor operated at 100% PWM, while the right motor was either stopped or received a limited PWM signal (60%), producing a smooth right turn. Conversely, in the left turn condition, the right motor continued at full speed, while the left motor received limited PWM or was stopped. For the stop command, both motors received no PWM signal (0%), causing the system to come to a complete halt.

Table 4. DC Motor Speed Test Results with PWM Based on Direction Control

No	Command Control	PWM Motor DC1	PWM Motor DC2	Outcome of System Movement
1	Forward	100% (Forward)	100% (Forward)	Moves Straight Forward
2	Reverse	100% (Reverse)	100% (Reverse)	Moves Straight Backward
3	Turn Right	100% (Forward)	60% (Reverse)	Turns to the Right
4	Turn Left	60% (Reverse)	100% (Forward)	Turns to the Left
5	Stop	0%	0%	Vessel Comes to a Complete Stop

Observations showed that the implementation of PWM provided effective and precise speed control over the system's directional movement. No voltage spikes or rotational imbalances were observed during the testing process. The delay caused by PWM transitions was also minimal, with an average speed adjustment latency of approximately 80–100 milliseconds, depending on the motor's initial condition. The strengths of this system lie in its simplicity of implementation, accessibility of the web interface, and flexibility in both directional and speed control. The system does not require a cloud server or additional software, making it well-suited for deployment in limited environments with local connectivity. However, some limitations were noted: Limited WiFi range (approximately 15 meters in open environments), System performance depends on the stability of the local WiFi connection, Lack of position feedback or onboard sensors, which means control remains entirely manual and

operator-dependent. For future development, the system could be enhanced by integrating a camera module (e.g., ESP32-CAM), distance sensors, and semi-autonomous or GPS-based control systems to expand its operational coverage and improve the device's autonomy.

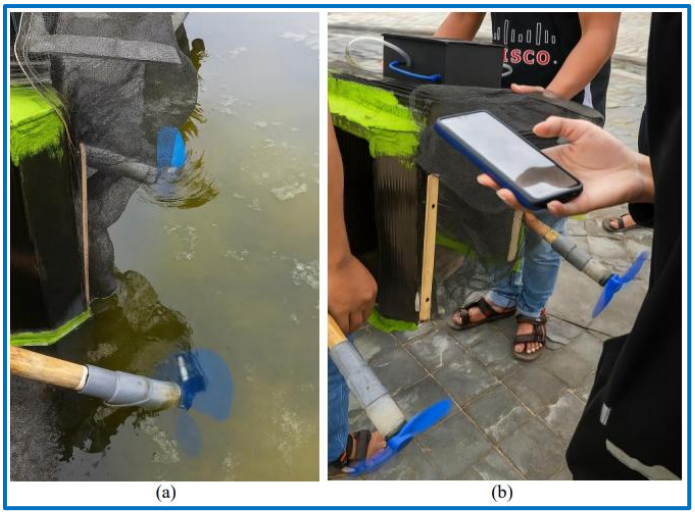

Figure 7. DC Motor Testing (a) Under Land and (b) Under Water Condition

Figure 7 presents the testing of a DC motor equipped with a propeller (fan), serving as the primary component of the propulsion system in the surface-cleaning device prototype. The testing was conducted under two different conditions to comprehensively evaluate the system's performance and stability. In the water-based test (Figure 7a), the DC motor was activated to drive the propeller while partially submerged in water. The aim of this test was to assess the thrust generated and the motor's efficiency under fluid load conditions. Observations focused on the device's stability, the strength of the thrust, and whether splashing or mechanical disturbances occurred within the propulsion system. In the land-based test (Figure 7b), the motor was tested without water load to directly observe the rotational speed of the propeller and to ensure that the power supply and control systems were functioning optimally. Testing on land also allowed for visual inspection of component integrity, including cable connections, motor alignment, and the structural stability of the propeller mount. Both tests were essential for comparing the performance of the DC motor under unloaded (free-air) and loaded (fluid resistance) conditions—critical factors for informing the final design of the propulsion system.

Battery Endurance Testing

Battery endurance testing was conducted to determine how long the system can operate based on the actual energy consumption of the DC motors under various duty cycle conditions and operating environments (on land and in water). For this approach, calculations were performed using the total battery energy (in Wh) as shown in Formula 2, and load power consumption (in Watts) as shown in Formula 3 [17]–[21].

$$Battery\ Energy\ (Wh) = \quad Battery\ Voltage\ (V) \times Battery\ Capacity\ (Ah) \tag{2}$$

$$Power\ Consumption\ (W) = \quad Voltage\ (V) \times CurrentDraw(A) \tag{3}$$

$$Operating\ Time\ (hours) = \frac{Battery\ Energy\ (Wh)}{Power\ Consumption\ (W)} \tag{4}$$

Using a 14.8V Li-Ion battery with a 2.2Ah capacity, the total available energy is 32.56 Wh. Based on the average current measurements across different test scenarios, the load power was calculated and used to estimate the system's theoretical operating time using Formula 4. Table 5 presents the results of the battery endurance test under two operating conditions: when the motors are running on land and when they are operating in water.

Table 5. DC Motor Speed Test Results with PWM Based on Direction Control

No	Motor Condition	PWM Duty Cycle	Average Current (A)	Load Power (W)	Theoretical Operating Time (Hours)	Actual Operating Time (Hours)
1	On Land	60%	1.0 A	14.8	2.20	3.0 hours
2	In Water	60%	1.3 A	19.24	1.69	2.1 hours
3	On Land	100%	1.5 A	22.2	1.47	2.1 hours
4	In Water	100%	1.9 A	28.12	1.16	1.4 hours

From Table 5, it can be observed that the actual operating time of the system is generally slightly longer than the theoretical calculation. This discrepancy is likely due to several factors: Load variation during testing, where the motor does not continuously operate at full capacity (e.g., during idle periods or brief stops). The efficiency of the motor driver and the power distribution system, which influences the actual current drawn. Tolerance in average current measurements, especially when using manual methods or non-datalogging multimeters. Nonetheless, a linear correlation between load power and operating time is clearly evident: the greater the load power, the shorter the operational duration. The energy and power-based approach offers a reasonably accurate estimation for predicting system runtime when designing and evaluating battery-powered embedded systems. Based on this test, it can be concluded that operating the DC motor at a 60% duty cycle results in more energy-efficient performance compared to full-speed operation (100%). Moreover, operating in water environments imposes greater load and higher current consumption compared to land conditions, thus requiring more careful power management in system design and deployment.

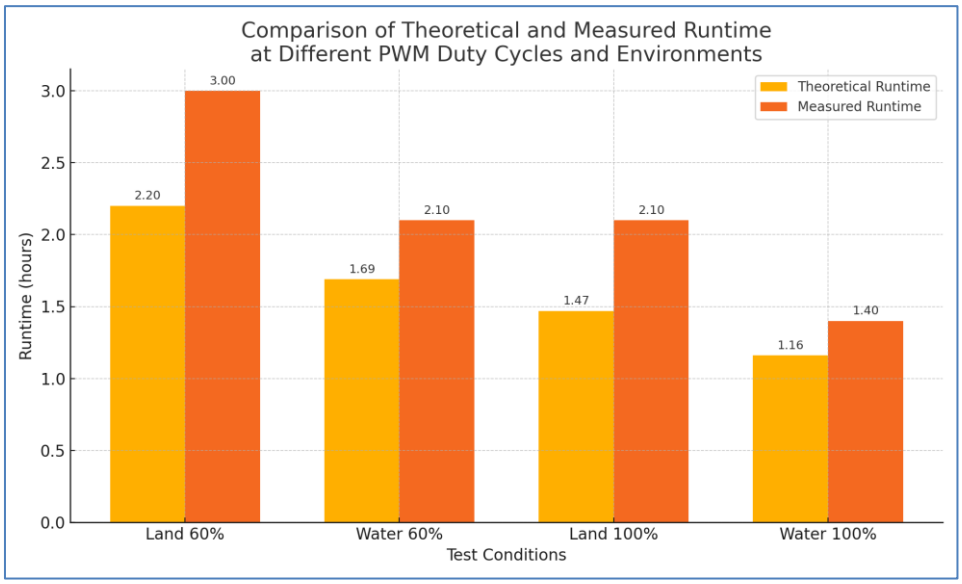

Figure 8. Comparative Analysis of Theoretical and Actual Operating Time in DC Motor System

Figure 8 presents a comparative graph between the theoretical operating time and the actual measured operating time, based on the testing conditions of the DC motor in two environments (land and water) and at two PWM duty cycle levels (60% and 100%). The graph shows a clear trend: operating time decreases as the PWM duty cycle increases, in both land and water environments. Additionally, operation in water results in shorter runtimes compared to land, indicating the presence of additional fluid resistance, which increases motor workload and current consumption. In general, a positive discrepancy is observed between theoretical and actual operating times. For example, at 60% PWM on land, the actual runtime was recorded at 3.0 hours, exceeding the theoretical estimate of 2.2 hours. This difference is likely due to the system not consistently operating under full load (i.e., intermittent operation), as well as higher motor control efficiency during non-continuous duty cycles. The graph further illustrates that the energy model based on Watt-hours provides a reasonably accurate prediction of power performance. However, it does not account for all system variables, such as motor efficiency, driver power losses, and dynamic conditions during operation.

CONCLUSIONS

This study aims to design and test a web-based control system for a surface waste-cleaning device on Lake Toba using the NodeMCU ESP8266, with direction and speed control of DC motors implemented through Pulse Width Modulation (PWM). The results of the implementation and testing show that the system can respond to navigation commands in real-time via a web interface without the need for additional applications. The system successfully controls directional movements (forward, reverse, turning, pivoting, and stopping) with a 100% success rate under a stable local network environment. DC motor testing demonstrated that PWM is effective in precisely controlling motor speed in both land and water conditions. However, the motor's rotational speed in water was observed to be approximately 15–20% lower than on land due to fluid resistance. These findings emphasize the importance of proper PWM tuning to ensure optimal system performance in aquatic environments. Furthermore, battery endurance testing revealed that the system's operating time on land is longer than in water. At a 60% duty cycle, the system could operate for approximately 3 hours on land and 2.1 hours in water. At a

100% duty cycle, the operating time decreased to about 2.1 hours on land and 1.4 hours in water. This confirms that power consumption in water is higher, due to the increased load on the motors caused by water resistance. These conclusions affirm that the developed system meets the basic functional requirements of a web-based navigational cleaning device and provide key insights into motor efficiency and power consumption across varying operational conditions. For future development, the system can be enhanced with the integration of distance sensors, a camera module (such as the ESP32-CAM), and GPS-based autonomous navigation to expand the cleaning coverage area and increase the device's operational autonomy. Additionally, the implementation of LoRa-based communication is suggested to extend control and monitoring capabilities.

REFERENCES

[1] B. Pratikno and P. Sidauruk, "Mempelajari Hubungan Air di Danau Toba dengan Air di Beberapa Sumber Mata Air Dekat Danau Toba," *J. Ilm. Apl. Isot. dan Radiasi*, vol. 11, no. 2, pp. 153–159, 2015, doi: 10.17146/jair.2015.11.2.2798.

[2] M. G. Saragih, E. D. Surya, and M. B, *Pariwisata Super Prioritas Danau Toba*. Medan: CV. Andalan Bintang Ghonim, 2021.

[3] D. J. P. P. dan K. Lingkungan, "Laporan Kinerja: Direktorat Pengendalian Pencemaran Air," Kementerian Lingkungan Hidup dan Kehutanan, Jakarta, 2022.

[4] A. Suwardono, F. E. Prahesti, E. M. Indrawati, and M. A. J. Ashofa, "IoT Based Catfish Farm Monitoring with ESP32 Microcontroller and DS18B20 Sensor," *JST (Jurnal Sains dan Teknol.*, vol. 13, no. 3, pp. 508–516, 2024, doi: 10.23887/jstundiksha.v13i3.85996.

[5] W. S. L. Nasution and P. Nusa, "Implementation of the Internet of Things (IoT) for Remote Light Control Using NodeMCU ESP8266 and Thingspeak Via Website-Based Internet," *J. Comput. Sci. Technol.*, vol. 3, no. 1, pp. 33–39, 2023, doi: 10.54840/jcstech.v3i1.100.

[6] S. Gunawan, A. H. Anshor, and Amali, "Sistem Monitoring dan Kontrol Taman Pintar Berbasis IoT (Internet of Things) dengan NodeMCU ESP8266," *Bull. Comput. Sci. Res.*, vol. 3, no. 4, pp. 283–288, 2023, doi: 10.47065/bulletincsr.v3i4.270.

[7] A. Winarno, Widodo, and M. K. Nurcahyo, "Smart Home Remote Control System Prototype Using Internet of Things (IoT) Based ESP8266 Microcontroller," *BEST J. Appl. Electr. Sci. Technol.*, vol. 5, no. 2, pp. 60–64, 2023, doi: 10.36456/best.vol5.no2.8063.

[8] I. H. Tambunan, B. A. Sihotang, D. Silaen, F. Michael, and K. G. Sitanggang, "Data Communication Between Wheeled Soccer Robots and Referee Box Using ESP8266 and Raspberry Pi 4B," *2023 29th Int. Conf. Telecommun.*, vol. 29th, pp. 1–5, 2023, doi: 10.1109/ICT60153.2023.10374059.

[9] E. Margirahayu, Junaidi, G. A. Pauzi, and S. W. Suciyati, "DC Motor Speed Control System with PWM (Pulse Width Modulation) Technique Based on Arduino For Centrifugation Equipment Application," *J. Energy, Mater. Instrum. Technol.*, vol. 3, no. 3, pp. 99–104, 2022, doi: 10.23960/jemit.v3i3.105.

[10] Pradeep, A. Ratnam, N. Saritha, I. G. Naidu, and G. Swapna, "Pulse Width Modulation Based DC Motor Closed Loop Speed Controller," *Tuijin Jishu/Journal Propuls. Technol.*, vol. 45, no. 02, pp. 4033–4038, 2024, doi: 10.52783/tjjpt.v45.i02.6587.

[11] B. Satria, H. Alam, M. E. Dalimunthe, M. Iqbal, and B. S., "Development of a DC Motor Speed Regulation System Using PWM for Two-Wheeled Electric Vehicles," *Pros. Semin. Nas. Dan Int. Fak. Tek. Dan Ilmu Komput. Univ. Dharmawangsa*, vol. 1, pp. 470–477, 2024.

[12] F. B. Setiawan, Y. Y. C. Wibowo, L. H. Pratomo, and S. Riyadi, "Perancangan Automated Guided Vehicle Menggunakan Penggerak Motor DC dan Motor Servo Berbasis Raspberry Pi 4," *J. Rekayasa Elektr.*, vol. 18, no. 2, pp. 94–101, 2022, doi: 10.17529/jre.v18i2.25863.

[13] A. E. Ramadhan, Djuniadi, and E. Apriaskar, "Sistem Pengaturan Pulse Width Modulation Motor Pada Robot Pembawa Makanan atau Minuman Menggunakan Joystick," *TELKA - Telekomun. Elektron. Komputasi dan Kontrol*, vol. 7, no. 2, pp. 134–143, 2021, doi: 10.15575/telka.v7n2.134-143.

[14] A. M. Ali, C. Shen, and H. A. Hashim, "A Linear MPC with Control Barrier Functions for Differential Drive Robots," *IET Control Theory Appl.*, vol. 18, no. 18, pp. 2693–2704, 2024, doi: 10.1049/cth2.12709.

[15] Q. I. Fatimah, R. Marselino, and Asnil, "Web-Based DC Motor Speed Design and Control," *Motiv. J. Mech. Electr. Ind. Eng.*, vol. 3, no. 3, pp. 101–112, 2021, doi: 10.46574/motivection.v3i3.99.

[16] Yogiswara, H. Y. Riskiawan, S. Anwar, and R. Ardiansyah, "Differential-Drive Wheeled Robot Controller using Pulse- Width modulation in disinfectant sprayer robot," *3rd Int. Conf. Food Agric.*, vol. 3, no. 1, pp. 151–157, 2021.

[17] A. R. Hambley, *Electrical Engineering: Principles & Applications*. New Jersey: Pearson, 2017.

[18] E. Hughes, *Electrical and Electronic Technology*. New Jersey: Prentice Hall, 2012.

[19] M. H. Rashid, N. Kumar, and A. R. Kulkarni, *Power Electronics: Devices, Circuits, and Applications: International Edition*, Fourth Edi. Harlow: Pearson, 2014.

[20] M. H. Rashid, *Power Electronics Handbook*. San Diego: Academic Press, 2001.

[21] A. R. Rey and R. A. Fatekha, "Analysis of Battery Energy Consumption in the Barelang V Base Robot with 4 Brushed DC Motors," in *Proceedings of the 7th International Conference on Applied Engineering (ICAE 2024)*, Atlantis Press, 2024, pp. 5–20. doi: 10.2991/978-94-6463-620-8_2.

PISTON
Journal of Technical Engineering:

Design of Helical Type Steam Generator for Experimental Power Reactor – Helium Side

Sunny Ineza Putri[1,a)], Mohammad Subekti[2], Awaludin Martin[1], Brian Agung Cahyo P[1], Jheri Hermanto[1], Ansor Salim Siregar[3]

[1]*Mechanical Engineering, Universitas Riau, Kampus Bina Widya KM. 12,5, Pekanbaru, Riau 28293, Indonesia*
[2]*Research Organization for Nuclear Energy (ORTN), National Research and Innovation Agency (BRIN), Jl. Lebak Bulus Raya No.49, RT.3/RW.2, South Jakarta, Jakarta 12440, Indonesia*
[3]*Mechanical Engineering, Politeknik Negeri Banyuwangi, Jl. Raya Jember No.KM13, Banyuwangi, East Java, 68461, Indonesia*

E-mail: [a)] sunnyinezap@lecturer.unri.ac.id

Received: July 10, 2025 *Revision: August 09, 2025* *Accepted: August 10, 2025*

Abstract: Previous research has not analyzed the helium temperature distribution in the RDE steam generator shell. This study aims to fill that gap by analyzing these thermal characteristics with empirical calculations and Ansys Fluent simulations. The validity of the RDE steam generator design is reaffirmed, having been successfully analyzed from both the water-flow perspective in previous research and the helium-side perspective in the present study. The analytical methods used herein showed strong consistency, with empirical and numerical simulation results differing by less than 10% across all parameters. Although the calculated shell height of 5.73 m exceeds the RDE design's 4.97 m, the overall design's validity is confirmed.

Keywords: HTGR, RDE, Steam Generator, Helium.

Abstrak: *Penelitian sebelumnya belum menganalisis distribusi temperatur helium pada bagian selubung (shell) steam generator RDE. Penelitian ini bertujuan untuk mengisi kekosongan tersebut dengan menganalisis karakteristik termal ini melalui perhitungan empiris dan simulasi Ansys Fluent. Validitas desain steam generator RDE ditegaskan kembali, setelah berhasil dianalisis baik dari perspektif aliran air pada penelitian sebelumnya maupun dari perspektif sisi helium pada penelitian ini. Metode analisis yang digunakan dalam penelitian ini menunjukkan konsistensi yang kuat, dengan hasil perhitungan empiris dan simulasi numerik memiliki perbedaan kurang dari 10% pada semua parameter. Meskipun tinggi selubung hasil perhitungan sebesar 5,73 m melebihi desain RDE sebesar 4,97 m, validitas desain secara keseluruhan tetap terkonfirmasi.*

Kata kunci: *HTGR, RDE, Pembangkit Uap, Helium.*

INTRODUCTION

The High Temperature Gas Reactor (HTGR) is a Generation IV nuclear reactor, distinguished by its high safety level. When the temperature increases suddenly, HTGR features negative temperature reactivity, the fission reaction will drop directly until the reactor temperature returns to its initial temperature. Many countries are considering HTGR since thermal efficiency is greater than PWR and BWR [1]. Development of High-Temperature Gas-cooled Reactor (HTGR) technology dates back to 1960. A key milestone was reached in 2000 when China built and operated the HTR-10, a 10 MW pilot plant designed to demonstrate the reactor's safety. This work culminated in the world's only commercially operating HTGR, the 210 MWth HTR-PM in China, which has been active since December 2023 [2]–[4].

Indonesia is preparing research on HTGR called the Experimental Power Reactor (RDE) with a capacity of 10 MW_{th} [5]. Helium and graphite function as coolants and moderators, with the inlet water coolant temperature

being 250°C and the outlet at 750°C [6]. The high critical working temperature of HTGR requires thermal-hydraulic analysis because very large temperature differences can damage components and shorten their service life. An uneven temperature distribution within a steam generator can lead to some tubes operating at dangerously high temperatures [7]. To forecast these thermal patterns, a coupled heat transfer analysis, which models the thermal interaction between the primary and secondary circuits, can be conducted using Ansys Fluent [8].

In previous research, the conceptual design of a steam generator on RDE has been studied from the perspective of a helical pipe where feed-water flows. The study obtained that the steam generator height is 4.97 m by empirical analysis methods and fluid simulations using Ansys Fluent. The boundary condition was the helium temperature used as heat flux to simulate the heat transfer [9]. Previous research on the RDE set the inlet water temperature at 418.15 K. In those studies, helium gas was introduced at a temperature of 973.15 K and a pressure of 34.2 bar, flowing at a rate of 4.27 kg/s. The helium then exited the system at a temperature of 511.42 K [10].

A gap exists in the current research, as the temperature profile of helium within the RDE steam generator shell has not been previously investigated. To address this, the present study analyzes the thermal characteristics on the helium side of the generator, using both empirical methods and numerical modeling with Ansys Fluent. Analyzing the helium temperature distribution is critically important because uneven heating directly impacts safety by causing component-damaging hot spots and compromises performance by lowering the reactor's overall thermal efficiency. This specific analysis represents a research gap because prior studies logically simplified the problem by focusing only on the water-side dynamics, treating the complex helium flow as a simple, uniform boundary condition rather than modeling its actual distribution. Conducting a comprehensive and realistic simulation of the steam generator—one that fully couples the heat transfer of both water and helium—is challenging due to technological resource limitations. As such, this research builds upon previous work by focusing exclusively on the helium simulation component.

METHODS

This research analyzes the thermal-hydraulic characteristics of helium gas within the RDE steam generator through a combination of simulation and empirical approaches. To facilitate the analysis, the steam generator's geometry, which consists of seven layers of helical pipes, is simplified into a model with a single helical pipe. This simplified representation assumes the pipe is positioned at the radial center, which results in a uniform temperature distribution. Furthermore, the heat transfer coefficient used in the model is set to the average value of the original seven-layer RDE design. In the RDE steam generator, the working fluid flows in the opposite direction. The water flows through the helical pipe from bottom to top, while the helium gas flows in the shell from top to bottom, similar to a counter-flow heat exchanger. Figure 1 illustrates a schematic diagram of the steam generator.

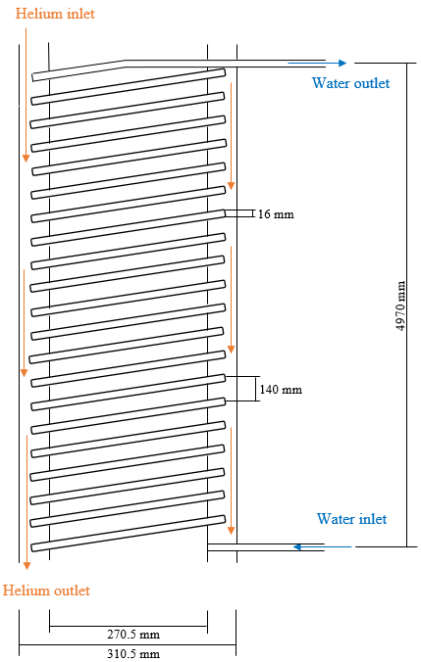

Figure 1. Schematic of Helical Pipe Steam Generator

The empirical analysis determines heat transfer throughout the system by calculating two key phenomena: convection in both the water and the helium, and conduction through the helical pipe's wall. For the helium side calculation, the flow is modeled as fully developed and turbulent within a smooth circular pipe. This assumption justifies using the classic Dittus-Boelter equation (1930), which is presented below:

$$Nu_D = 0.023 Re_D^{4/5} Pr^n \tag{1}$$

Where n = 0.4 for the heating process (Ts > Tm) and n = 0.3 for cooling (Ts < Tm), in the range:

$$\begin{bmatrix} 0.7 \leq Pr \leq 160 \\ Re_D \geq 10{,}000 \\ L/d \geq 10 \end{bmatrix} \tag{2}$$

The design and performance prediction of a heat exchanger requires the determination of several key parameters. These include the overall heat transfer coefficient (U), the total heat transfer surface area (A), and the fluid temperatures at both the inlet and outlet. These values are then used to establish the total rate of heat transfer (q), which is calculated with the equation that follows:

$$q = \dot{m}_h c_{p,h} (T_{h,i} - T_{h,o}) \tag{3}$$

$$q = \dot{m}_c c_{p,c} (T_{c,o} - T_{c,i}) \tag{4}$$

This analysis adapts Newton's Law of Cooling for the complex conditions within a heat exchanger. Specifically, the simple convection coefficient (h) is replaced by the overall heat transfer coefficient (U) to account for all thermal resistances (e.g., conduction through the wall and convection on both sides). Furthermore, the model acknowledges that the temperature difference (ΔT) between the fluids is not constant but varies at each position. Incorporating these modifications, the heat transfer rate is given by the following equation.

$$q = UA\Delta T_{lm} \tag{5}$$

For a counter-flow arrangement, where the two fluids flow in opposite directions, the Log Mean Temperature Difference (ΔT_{lm}) is given by the formula below:

$$\Delta T_{lm} = \frac{(T_{h,i} - T_{c,o}) - (T_{h,o} - T_{c,i})}{\ln[(T_{h,i} - T_{c,o})/(T_{h,o} - T_{c,i})]} \tag{6}$$

To calculate the pressure drop (Δp) across the system, the following formula is used [11]:

$$\Delta p = 4f \frac{L}{D_h} \frac{\rho u_m^2}{2} \tag{7}$$

For the purpose of this analysis, heat transfer to the surroundings, as well as any changes in kinetic and potential energy, are considered insignificant. The boundary conditions used are summarized in Table 1, where the inlet helium temperature is 973.15 K at a pressure of 3 MPa. In this study, the helium mass rate is 0.087 kg/s amid design simplifications that balance the actual design. Empirical calculations require fluid properties that are highly dependent on fluid temperature, so the CoolProp add-in in Microsoft Excel is used.

Table 1. Boundary Condition

Parameter	Symbol	Unit	Fluids	
			Water	Helium
Inlet temperature	T_{in}	°C	145.00	700.00
		K	418.15	973.15
Outlet temperature	T_{out}	°C	530.00	250.00
		K	803.15	523.15
Pressure	p	bar	60	30
		MPa	6	3
Mass flow rate	$\dot{m}$	kg/s		
1. RDE			3.57	4.27
2. This research			0.073	0.087

The empirical method was used to calculate several key parameters: the overall heat transfer coefficient (U), the total heat transfer area (A), the required height of the steam generator, and the pressure drop (Δp). The results are compared to previous research and shown in Table 2.

Table 2. Comparison of Results from the RDE (RELAP) Model and Empirical Analysis [9]

Parameter	RELAP	Empiric	Diff
$T_{h,i}$	700°C	702.8°C	+2.8
H	4.97 m	3.98 m	-0.99
A	1.60 m^2	1.32 m^2	-0.28
q	0.204 MW	0.205 MW	+0.001

The properties of helium gas in the simulation method in Ansys Fluent use a piecewise-linear setting with three temperature points for the properties of density, viscosity, conductivity, and specific heat. In the CFD case, the non-linear setting is converted into a linear form to ease the computational method [12]. Moreover, the heat transfer is more accurate to the actual property value. The simulation model was built using design dimensions and boundary conditions derived from the preceding empirical analysis. This included the setup for convection heat transfer, where the overall heat transfer coefficient (U) was based on the empirical results, and the free stream temperature was defined as the average water temperature in the helical pipe. Therefore, a schematic of the shell where the helium flows used in the simulation is presented in Figure 2.

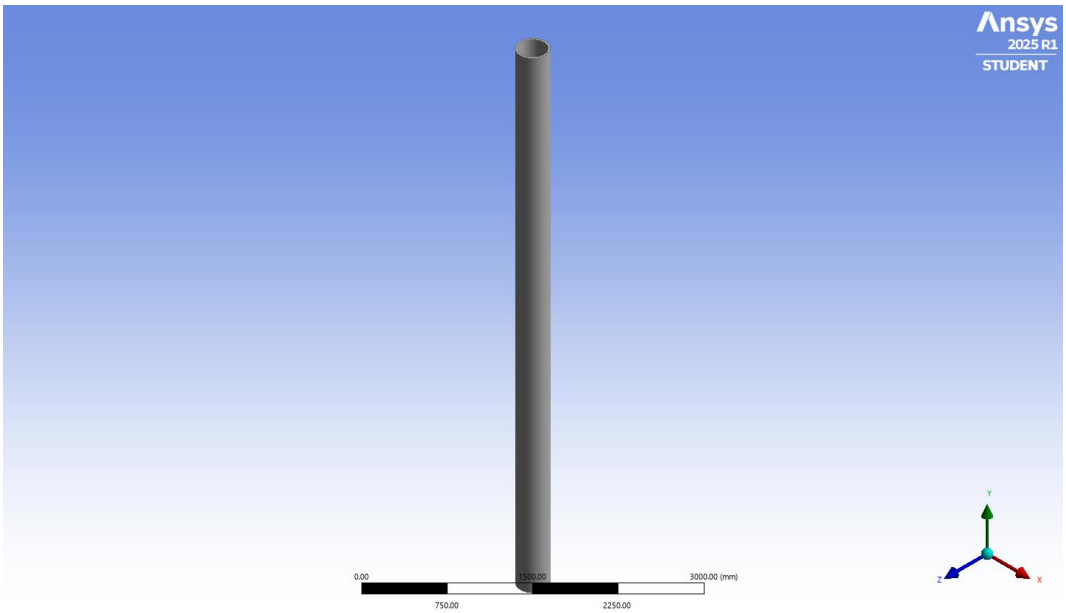

Figure 2. Design of Shell Steam Generator using Ansys DesignModeler

For the numerical simulation, the pressure-velocity coupling was handled using the Coupled algorithm, a method chosen for its suitability with the specified boundary conditions of a velocity-inlet and a pressure-outlet. To capture the effects of turbulence in the water flow, the realizable k-epsilon model was employed. High accuracy was sought by applying second-order discretization schemes; a second-order upwind scheme was used for the momentum, turbulent kinetic energy (k), turbulent dissipation rate (ϵ), and energy equations, while a standard second-order scheme was used for pressure. The solution was considered converged when residuals for continuity, velocity components, k, and ϵ dropped below 0.001, while the energy equation required a stricter convergence criterion of 1×10^{-6}. The simulation was configured with an operating pressure of 3 MPa and included a gravitational acceleration of -9.81 m/s^2 acting along the y-axis.

RESULT AND DISCUSSION

The analysis determined that the thermal power transferred from the helium is 0.203 MW. This was achieved with a calculated overall heat transfer coefficient of 794.076 W/(m^2·K) across a heat transfer surface area of 1.897 m^2, corresponding to a required steam generator shell height of 5.73 m Therefore, a summary of the empirical calculation results in comparison to previous research is shown in Table 3.

Table 3. Comparison of Results from the RDE (RELAP) Model and Empirical Analysis

Parameter	RELAP	Empiric[1)]	Empiric[2)]
$T_{h,o}$	523.15 K	523.15 K	523.15 K
H	4.97 m	3.98 m	5.73 m
A	1.60 m^2	1.32 m^2	1.90 m^2
q	0.204 MW	0.205 MW	0.203 MW

[1)] prior research
[2)] this research

The analysis reveals a notable discrepancy in the steam generator's physical dimensions, where the calculated shell height of 5.73 m exceeds the established RDE reference design of 4.97 m by 0.76 m. This variance, while significant, is not indicative of a design flaw but is rather a quantifiable outcome stemming from a complex interplay between fundamental design assumptions, particularly in material selection and flow configuration, when compared to the reference model. Primarily, the material selection differs, as this analysis assumes an aluminum pipe while the RDE design utilizes a different material. This variation in material directly influences the thermal conductivity, which in turn alters the calculation of the overall heat transfer coefficient (U). Furthermore, the flow arrangement modeled in this study is a counter-flow configuration, which contrasts with the cross-flow scheme employed in the RDE's RELAP-based design.

Interestingly, both of these primary modeling differences—the use of a higher-conductivity material and a more efficient flow configuration—would individually predict a design that is more compact than the reference. The fact that the calculated shell height is nonetheless greater suggests that these advantages are outweighed by other implicit parameters or more aggressive assumptions within the RDE (RELAP) reference model. These could include significantly higher prescribed convection coefficients, a different geometric packing density of the helical tubes, or different target temperature approaches that were not replicated in the present empirical model. It remains crucial, however, to acknowledge the foundational design choice. The inherent superiority of the helical heat exchanger configuration, where secondary flow induced by the pipe's curvature actively enhances the convective heat transfer rate, underpins the viability of both the present design and the RDE reference [13].

The results of the Ansys Fluent simulation were validated against empirical calculations, with the comparison detailed in Table 4. The numerical model is shown to be accurate, as the deviation between the simulated and empirical results is less than 10%.

Table 4. Comparison of Results from the Empirical Analysis and Simulation using Ansys Fluent

Parameter	Empiric	Ansys	Diff
$T_{h,i}$	973.15 K	970.35 K	0.28%
$T_{h,o}$	523.15 K	536.68 K	2.58%
$\dot{m}$	0.087 kg/s	0.087 kg/s	0%
Δp	0.0013 MPa	0.0014 MPa	7.69%

The spatial distribution of key thermohydraulic parameters, as obtained from the numerical simulation, is presented in Figures 3 and 4. The simulation predicts a helium outlet temperature of 536.68 K. This minor, yet notable, overprediction can be attributed to a key idealization in the current computational model: the omission of inter-pipe thermal contact. In the simulation, each helical tube is treated as a thermally isolated entity interacting only with the surrounding helium flow. In a physical assembly, however, the packed helical tubes will have numerous points of contact, creating conductive pathways or thermal bridges between adjacent tubes. These pathways would allow heat to conduct directly from hotter tubes to cooler ones, facilitating a more effective thermal homogenization across the entire tube bundle. This additional mode of heat rejection from the hotter fluid streams is not accounted for in the model, likely leading to the slightly elevated average outlet temperature observed. Consequently, it is postulated that the model's predictive accuracy could be significantly enhanced by incorporating contact thermal resistance in future iterations. This refinement would likely lower the predicted outlet temperature, thereby minimizing the deviation from the RDE benchmark data.

In summary, while the thermal model exhibits a minor, explainable deviation due to a specific modeling simplification, the hydrodynamic model is well-validated. This provides overall confidence in the simulation's utility as a predictive tool, coupled with a clear understanding of its current limitations and a direct path for future refinement.

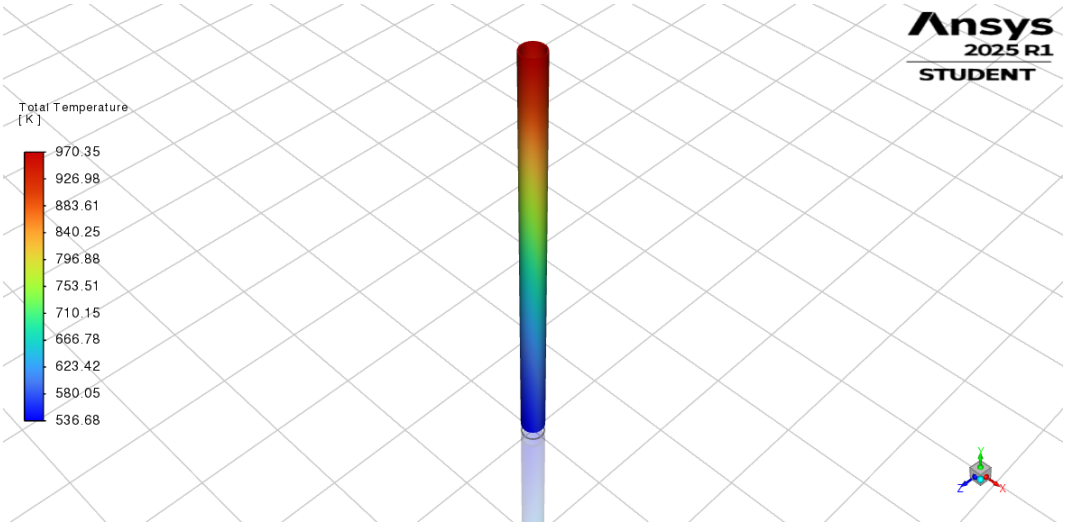

Figure 3. Temperature Distribution of Shell Steam Generator

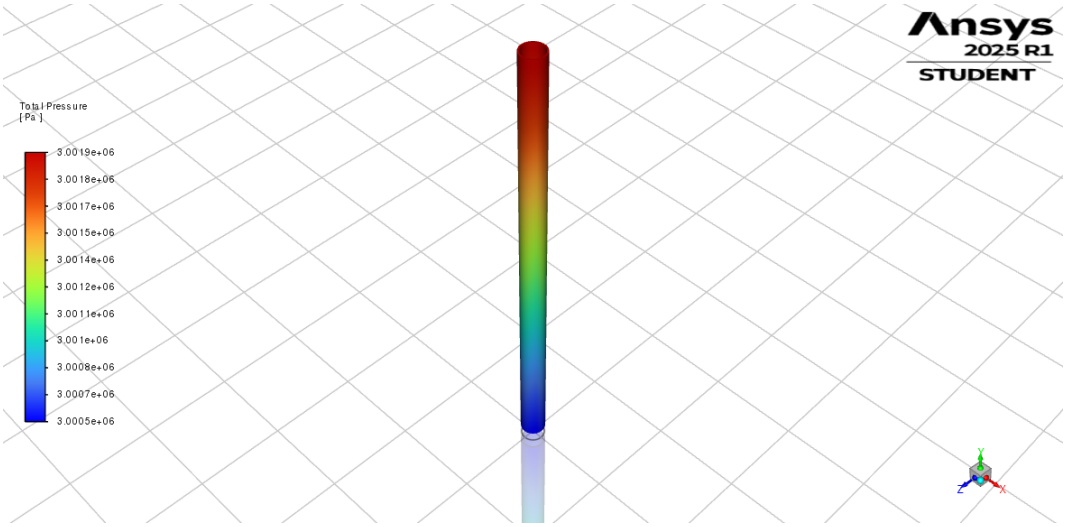

Figure 4. Pressure Distribution of Shell Steam Generator

CONCLUSIONS

In conclusion, the RDE design remains consistent within acceptable limits after empirical and numerical steam generator design studies from the water flow perspective in previous research and the helium perspective in this research. A key outcome of this work is the high degree of confidence in the analytical methods, established through a close agreement (<10% deviation) between empirical and numerical results. The analysis culminates in a design with a shell height of 5.73 m, a dimension understood to be influenced by the model's exclusion of inter-pipe contact heat transfer. Therefore, this research provides a reliable set of analytical tools and data that serve as a crucial consideration for future iterations and optimization of advanced steam generator designs.

ACKNOWLEDGEMENT

The authors would like to convey a great appreciation to Mechanical Engineering, Universitas Riau and Research Organization for Nuclear Energy (ORTN), National Research and Innovation Agency (BRIN) for supporting this research.

REFERENCES

[1] A. Waluyo and A. Khakim, "HTGR Thermohydraulic Study on Steady-State Conditions using ANSYS FLUENT," in *2020 Annual Nuclear Safety Seminar Proceeding: Innovations to Support Nuclear Safety and Security for*

Advanced Human Resources and Excellent Indonesia, Jakarta: Nuclear Energy Regulatory Agency, Oct. 2020.

[2] H. Li, "A Brief Review of the Development of High Temperature Gas Cooled Reactor," *IOP Conf. Ser. Earth Environ. Sci.*, vol. 631, no. 1, p. 12080, 2021, doi: 10.1088/1755-1315/631/1/012080.

[3] Y. Zheng, B. Xia, Z. Chen, H. Zhang, and J. Sun, "Preliminary Study on HTR-10 Operating in Higher Outlet Temperature," *J. Phys. Conf. Ser.*, vol. 2048, no. 1, p. 12035, 2021, doi: 10.1088/1742-6596/2048/1/012035.

[4] M. P. Dąbrowski *et al.*, "Concept of the polish high temperature gas-cooled reactor HTGR-POLA," *Nucl. Eng. Des.*, vol. 424, p. 113197, 2024, doi: 10.1016/j.nucengdes.2024.113197.

[5] G. R. Sunaryo, S. Bakhri, M. Subekti, T. Setiadipura, and D. S. Wisnubroto, "RDE Design Strategy for Indonesia Experimental NPP," *J. Phys. Conf. Ser.*, vol. 2048, no. 1, p. 12002, 2021, doi: 10.1088/1742-6596/2048/1/012002.

[6] D. S. Wisnubroto, G. R. Sunaryo, and Y. S. Budi Susilo, "Indonesia's RDE program: A multifaceted approach to nuclear energy development encompassing human Resource building, public acceptance, and technological innovation," *Nucl. Eng. Technol.*, vol. 57, no. 8, p. 103560, 2025, doi: 10.1016/j.net.2025.103560.

[7] X. Li, W. Gao, Y. Su, and X. Wu, "Thermal analysis of HTGR helical tube once through steam generators using 1D and 2D methods," *Nucl. Eng. Des.*, vol. 355, p. 110352, 2019, doi: https://doi.org/10.1016/j.nucengdes.2019.110352.

[8] W. Afsar, J. Cai, and S. S. Cui, "Thermo-Fluid-Solid Coupling Analysis in the Steam Generator of a High Temperature Gas Cooled Reactor," in *Proceedings of the International Workshop on Materials, Chemistry and Engineering - Volume 1: IWMCE*, INSTICC: SciTePress, 2018, pp. 236–242. doi: 10.5220/0007437002360242.

[9] S. I. Putri, P. S. Darmanto, and M. Subekti, "Design of Helical Type Steam Generator for Experimental Power Reactor," *J. Teknol. Reakt. Nukl. Tri Dasa Mega*, vol. 25, no. 1, pp. 1–8, Mar. 2023, doi: 10.55981/tdm.2023.6656.

[10] B. W. Riyandwita *et al.*, "Analytical Design of Helical Coil Steam Generator for Hot Temperature Gas Reactor," *J. Phys. Conf. Ser.*, vol. 1198, no. 4, p. 42014, 2019, doi: 10.1088/1742-6596/1198/4/042014.

[11] S. Kakaç, H. Liu, and A. Pramuanjaroenkij, *Heat Exchangers: Selection, Rating, and Thermal Design*, 2nd Edition. Boca Raton: CRC Press, 2002. doi: 10.1201/9781420053746.

[12] M. Asghari, A. M. Fathollahi-Fard, S. M. J. Mirzapour Al-e-hashem, and M. A. Dulebenets, "Transformation and Linearization Techniques in Optimization: A State-of-the-Art Survey," *Mathematics*, vol. 10, no. 2. p. 283, 2022. doi: 10.3390/math10020283.

[13] U. E. Inyang and I. J. Uwa, "Heat Transfer in Helical Coil Heat Exchanger," *Adv. Chem. Eng. Sci.*, vol. 12, no. 1, pp. 26–39, 2022, doi: 10.4236/aces.2022.121003.

PISTON
Journal of Technical Engineering:

System Circuit Analysis of Solar Panel Chicken Egg Incubator

Sulanjari[1,a)], Ilyas Rasyid Wicaksana[1,b)], Kiki Tristiawanti Simbolon[2], Agustina Dyah Setyowati[3], Nur Rohmat[1], Ade Irawan[1]

[1]*Department of Mechanical Engineering, Pamulang University, Jl. Surya Kencana No. 1, Tangerang Selatan, Banten, 15417, Indonesia*
[2]*Department of Informatics Engineering Education, STKIP Pangeran Antasari, Jl. Veteran No.1060/19, Deli Serdang, Sumatera Utara, 20116, Indonesia*
[3]*Department of Chemical Engineering, Pamulang University, Jl. Surya Kencana No. 1, Tangerang Selatan, Banten, 15417, Indonesia*

E-mail: [a)] dosen01182@unpam.ac.id
[b)] ilyasrasyidwicaksana@gmail.com

Received: June 30, 2025 *Revision: August 11, 2025* *Accepted: August 11, 2025*

Abstract: The chicken egg incubator is an innovation in the method of hatching chicken eggs that has higher efficiency and is up-to-date compared to using incubating hens. With this incubator machine, the incubation process of chicken eggs can be controlled and can reach the ideal temperature and humidity for the hatching process of chicken eggs. This research was conducted to find out how much power is used by this chicken egg incubator machine, as well as how long it takes for 300 Wp solar panels to charge a battery with a capacity of 12 V / 80 Ah. The research was conducted to find out the percentage of success of this egg hatching and to calculate how long it takes to reach the BEP (Break Even Point). This chicken egg incubator machine is powered by a 300 Wp solar panel with a 12 V / 80 Ah battery. In the incubator circuit there is a humidifier mist maker component to maintain the incubator humidity at 50%–60%. Lighting uses 2 incandescent lamps with a total power of 50 W, as well as a ventilation fan that turns on when the temperature in the incubator is excessive in order to keep the temperature at 36 ℃–38.5 ℃. The drive motor is set to move for 3 seconds every 3 hours. This chicken egg incubator has a power consumption of 74.55 W with an egg hatching success rate of 86%. This chicken egg incubator takes about 500 days or 1 year and 5 months to reach its BEP (Break Even Point).

Keywords: Solar Panel, Temperature, Humidity, Egg Hatching Machine, Break-Even Point.

Abstrak: *Inkubator telur ayam merupakan inovasi dalam metode penetasan telur ayam yang memiliki efisiensi lebih tinggi dan lebih modern dibandingkan menggunakan indukan ayam secara langsung. Dengan mesin inkubator ini, proses penetasan dapat dikendalikan sehingga dapat mencapai suhu dan kelembapan ideal untuk proses penetasan telur. Penelitian ini dilakukan untuk mengetahui berapa besar daya yang digunakan oleh mesin inkubator telur ayam ini, serta berapa lama waktu yang dibutuhkan oleh panel surya 300 Wp untuk mengisi baterai berkapasitas 12 V / 80 Ah. Penelitian ini juga bertujuan untuk mengetahui persentase keberhasilan penetasan telur serta menghitung waktu yang diperlukan untuk mencapai titik impas (Break Even Point). Mesin inkubator ini menggunakan sumber daya dari panel surya 300 Wp dengan baterai 12 V / 80 Ah. Pada rangkaian inkubator terdapat komponen humidifier mist maker untuk menjaga kelembapan pada kisaran 50%–60%. Pencahayaan menggunakan dua lampu pijar dengan total daya 50 W, serta kipas ventilasi yang menyala ketika suhu di dalam inkubator melebihi batas untuk menjaga suhu pada kisaran 36 ℃–38,5 ℃. Motor penggerak diatur untuk bergerak selama 3 detik setiap 3 jam. Inkubator telur ayam ini memiliki konsumsi daya sebesar 74,55 W dengan tingkat keberhasilan penetasan 86%. Waktu yang dibutuhkan untuk mencapai titik impas adalah sekitar 500 hari atau setara dengan 1 tahun 5 bulan.*

Kata kunci: *Panel Surya, Suhu, Kelembapan, Mesin Penetas Telur, Titik Impas.*

INTRODUCTION

In this modern era, the development of renewable technology is very rapid, especially in the poultry farming sector, and the demand for chicken meat supply is quite high in the market. While this will not be achieved just by waiting for brooding chickens to sit incubating eggs. So a more efficient and sophisticated egg hatching system is needed with the help of renewable technology, namely the "chicken egg incubator." The chicken egg incubator itself is a machined egg hatching system in which all egg hatching processes are controlled by the machine, starting from optimal and controlled temperature and humidity conditions to stimulate embryo growth until the eggs hatch. The temperature and relative humidity inside the incubator are controlled at 36–40 ℃ and 50–60% relative humidity [1].

A very abundant source of energy and a source of life on earth is the sun, which is very much needed for life, especially its use in engineering as a power plant. Solar energy is one form of utilization of renewable energy sources that are environmentally friendly [2]. In its development, Solar Power Plant technology is an alternative technology to meet human electricity needs. Solar power plants have three types of systems, namely on-grid, off-grid, and hybrid. The on-grid Solar Power Plant system is directly connected to the State Electricity Company's electricity network, while the off-grid Solar Power Plant system uses batteries to store energy so that it can still provide electricity and is not connected to the State Electricity Company's electricity network. As for the hybrid Solar Power Plant system, it combines the advantages of both on-grid and off-grid systems [3]. If the irradiation intensity does not reach its peak, the battery has to work harder when discharging. This condition usually occurs when it is not the maximum sunshine hour (Peak Sun Hour). Peak Sun Hour (PSH) is a parameter that indicates the duration of maximum solar irradiation each day in hours. However, the design of a typical Solar PV system already considers the accumulation of this time in the autonomous period (autonomous day) when it is built [4].

In previous research, the chicken egg incubator with energy resources from solar panels used 120 Wp solar panels, 12 V / 50 Ah batteries, 10 A solar charge controller, 500 W inverter, and 2 lamps (10 W). The incubator temperature is 37.5 ℃–39 ℃ and the humidity is about 52%–55%. The eggs used were 50 eggs. The research was conducted for 20–21 days until the eggs hatched; from the study, 90% of the eggs hatched and 10% failed to hatch [5]. In general, the hatching time of chicken eggs is in the range of 21 days at a temperature of 36–40 ℃ with humidity of 50%–60%, while for duck eggs it is in the range of 28 days at a temperature of 36–40 ℃ with humidity of 60%–70% [6].

Therefore, research will be carried out on an egg incubator system using solar panels. This tool has a temperature, humidity, and lighting control system with automatic sensors. Lighting and temperature are obtained from 50 W incandescent lamps (2 pieces). Temperature and humidity measurements use the Automatic Computer Control Incubator XM-18 Thermohygrostat tool. As for the power supply, the incubator uses 150 Wp solar panels, as many as 2 pieces, for charging a 12 V / 80 Ah battery, with an additional solar charge controller (20 A) and inverter (500 W). The research was conducted using chicken egg media to shorten data collection on the performance of solar panel chicken egg incubators from the beginning of the incubation period until the eggs hatch.

METHODS

This study uses a research method designed to systematically obtain accurate and relevant data and information in order to provide a clear and comprehensive understanding of the solar-powered egg incubator being analyzed. This research employs a qualitative descriptive method, which is used to systematically describe and interpret the observed data without conducting statistical hypothesis testing.

Data collection in this research is carried out through two main techniques: literature study and direct observation. The literature study involves reviewing relevant references such as journals, books, scientific articles, and other sources related to solar-powered incubator technology. The observation method is conducted by directly observing the operation and performance of the solar panel-based chicken egg incubator. The data obtained from these observations are used to analyze the effectiveness and reliability of the system.

The equipment used in this study includes a solar-powered incubator system composed of two 300 Wp solar panels, a 20 A solar charge controller, a 12 V / 80 Ah battery, a 1000 W inverter, an automatic transfer switch, an XM-18 automatic computer incubator controller, a rack drive motor, two 50 W incandescent lamps, a ventilation fan, and a mist maker humidifier. These components work together to create and maintain the necessary environment for egg incubation using solar energy. To support data measurement and monitoring, several measuring instruments are used, including a clamp meter, a multimeter, and a stopwatch. The experimental

materials used in this study consist of 15 free-range chicken eggs, which are incubated using the designed solar-powered incubator system.

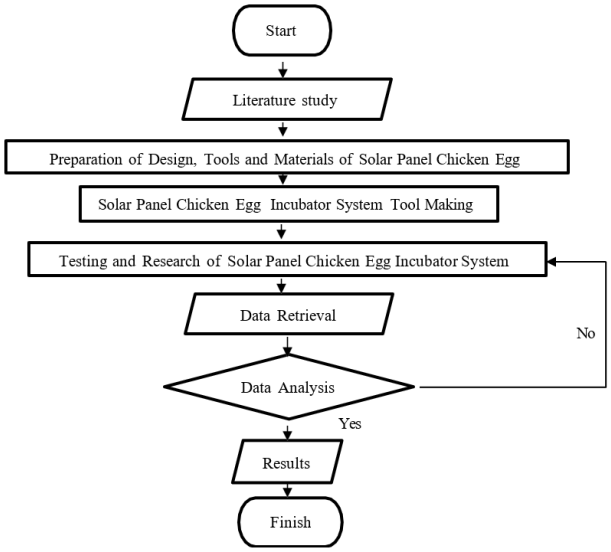

Figure 1. Schematic diagram of a solar-powered chicken egg incubator

Incubator Circuit Design

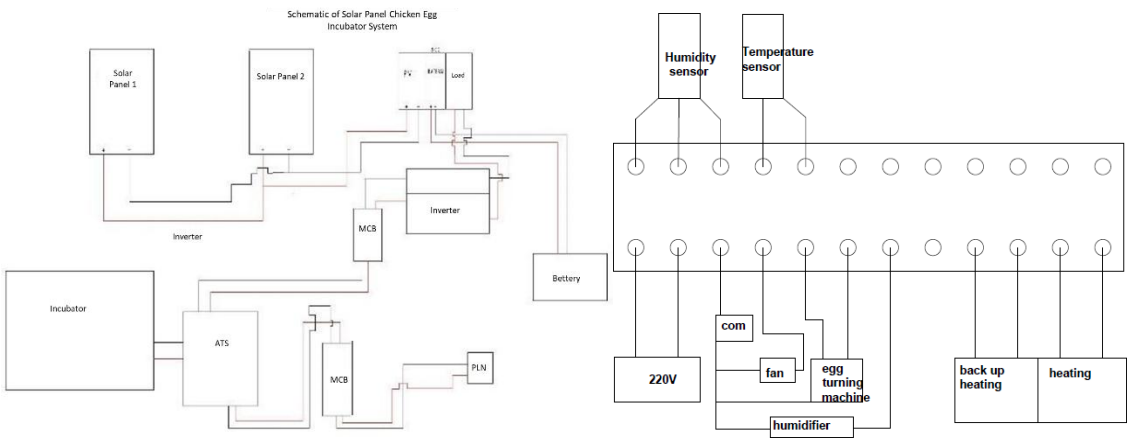

Figure 2. Electrical schematic drawings: (a) solar-powered chicken egg incubator circuit and (b) automatic incubator machine

Figure 3. (a) Incubator design drawing; (b) physical drawing of the electrical circuit and solar-powered chicken egg incubator

Investment Cost of Solar-Powered Chicken Egg Incubator

Table 1. Investment Cost

No	Item Name	Total	Item Price
1	Solar Panel 150 Wp	2	Rp2.420.000
2	Battery 12 V / 60 Ah	1	Rp1.020.000
3	Solar Charge Controller 20 A	1	Rp375.000
4	Inverter 500 W	1	Rp320.000
5	Automatic Transfer Switch 2P 125A 230V	1	Rp330.000
6	Transformer Box	1	Rp130.000
7	MCB	2	Rp60.000
8	AC Current Installation Cable (10 m)	1	Rp50.000
9	Automatic Computer Control Incubator XM-18	1	Rp320.000
10	DC Current Installation Cable (10 m)	1	Rp15.000
11	Iron Elbow (7 m)	4	Rp210.000
12	Plywood Board 6 mm (100 × 60 cm)	4	Rp155.000
13	Plywood Board 6 mm (60 × 60 cm)	2	Rp40.000
14	Egg Rack	1	Rp10.000
15	Mist Maker Humidity Ultrasonic	1	Rp110.000
16	Lamp (25 W)	2	Rp10.000
17	Motor Synchronous 50KTYZ	1	Rp90.000
18	Other costs		Rp335.000
	Total		**Rp6.000.000**

Calculation Design Basis

In the design of this solar panel chicken egg incubator machine, the production process is run by a battery as an energy source, where the battery function is very important in this tool. To find out the electrical power needed by the incubator, the following equation is used [7].

$$E = P \,.\, t \tag{1}$$

Description:

E = Electrical Energy (Watt-hours)
P = Electrical Power (Watt)
t = Time (Hours)

Input Power Calculation [8]:

$$P = V \,.\, I \tag{2}$$

Description:

P = Electrical Power (Watt)
V = Voltage (Volt)
I = Current (Ampere)

The calculation formula for battery charging time by solar panels is as follows [9]:

$$t = \frac{c}{i} \tag{3}$$

Description:

t = Charging Time (Hours)
c = Battery Capacity (Ah)
i = Battery Charging Current (Ampere)

For the formula to calculate BEP (Break Even Point), the following is used [10]:

$$BEP = \frac{FC}{P - VC} \tag{4}$$

Description:

BEP = Break Even Point
FC = Fixed Cost
P = Price per Unit
VC = Variable Cost per Unit

RESULT AND DISCUSSION

Battery Power Consumption

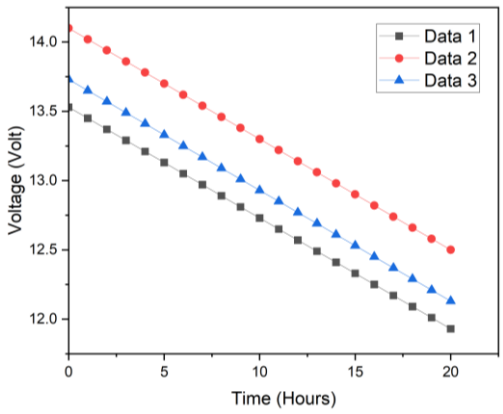

Figure 4. Battery power consumption

From the table and graph above, it can be seen that this solar panel chicken egg incubator works for 20 hours from 14.00 WIB to 10.00 WIB. The incubator power consumption obtained shows that every 1 hour the voltage drops by 0.08 V constantly. In three instances of taking data at the same time and in the same hot weather conditions, the three data sets have exactly the same voltage drop. From the formula calculation, it is found that when the incubator system turns on to increase the temperature in the incubator from 36 ℃ to 38.5 ℃, it takes 4 minutes with a current flow of 0.32 A and a voltage of 213 V. Meanwhile, when it reaches a temperature of 38.5 ℃, the system will turn off until the temperature drops to 36 ℃, which takes 4 minutes with a current flow of 0.003 A and a voltage of 213 V. So, the power required by this solar panel chicken egg incubator is 74.55 W. Then the total power required by this solar panel chicken egg incubator to work for 20 hours is 745.5 Wh.

Battery Charging Time

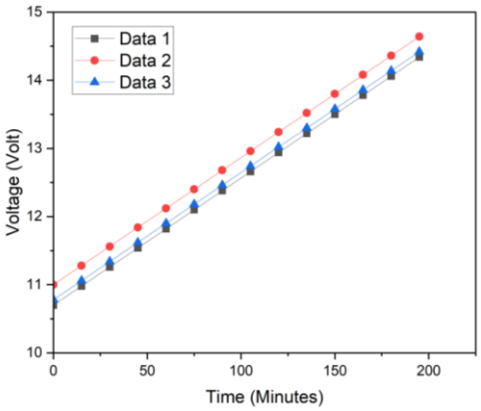

Figure 5. Battery charging time

Based on the table and graph above, it can be seen that battery charging is carried out from 10:30 WIB to 14:00 WIB. Every 15 minutes, the battery voltage (V) rises by 0.28 V constantly for 195 minutes or 3 hours 15 minutes. In the three instances of data collection, the exact same results were obtained because the data collection was carried out in a state of very hot sunlight during these three data collections. From the calculation of the formula carried out, it is found that the solar panel with a capacity of 300 Wp is able to charge the battery from a drop state, namely at 10.7 V to a full battery at a voltage of about 14.5 V, taking 3 hours 12 minutes.

BEP (Break Even Point)

In this experiment, 15 native chicken eggs were used for hatching trials. After incubating for about 20 days, 13 native chicks hatched and 2 native chicks failed to hatch, so it can be known that the success rate of this egg hatching machine is 86.6%. Before calculating the BEP (Break Even Point), it is necessary to know the age of use of this series of solar panel chicken egg incubators, which has a general life of 20 years. The percentage of success of the incubator machine in hatching eggs is 86%. The selling price of 1-week-old native chicks is generally Rp 10,000/head. The cost of 1 chicken egg and others is Rp 7,000.

Because the capacity of this chicken egg incubator machine is large, able to accommodate up to 100 native chicken eggs, it is assumed that if once incubating 100 native chicken eggs, the eggs that will hatch are as many as 86 chicks. One incubation takes 20 days. Then BEP can be achieved within 500 days or 1 year and 5 months.

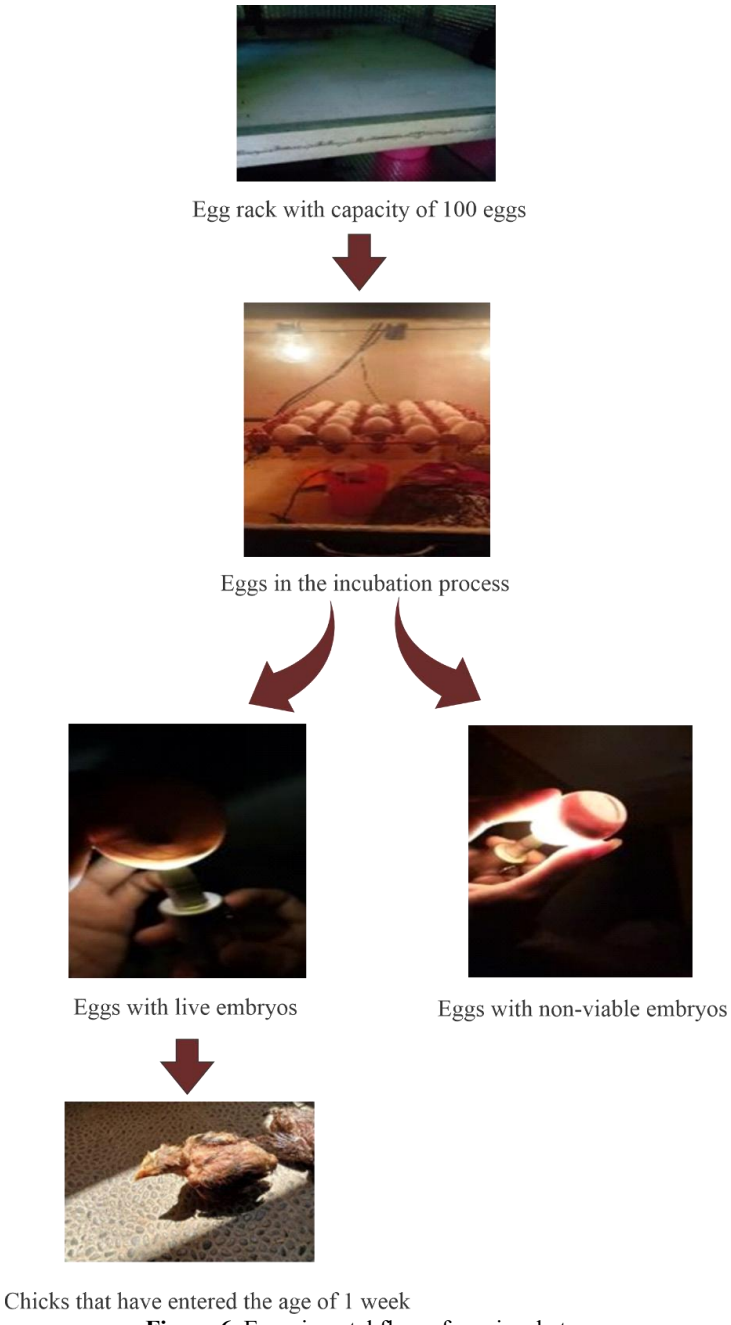

Figure 6. Experimental flow of egg incubator

CONCLUSIONS

From this study, it was found that the incubator power is 74.55 W, which works for 20 hours a day. The current flowing when the system is on is 0.32 A, and when the system is off, the current flow is 0.03 A, at a voltage of 213 V. With a battery capacity of 12 V / 80 Ah, the battery is only used for 20 hours a day and 4 hours using State Electricity Company electricity when charging the battery. For battery charging with 150 Wp solar panels, as many as 2 pieces in series to a total of 300 Wp, can charge the battery to 14.6 V in 3 hours 15 minutes. For the percentage of success of hatching chicken eggs from testing, the value is 86%. Therefore, in the calculation of BEP (Break Even Point) or break-even point, it can be achieved within 500 days or 1 year and 5 months in the incubation process carried out continuously.

REFERENCES

[1] J. Y. Muhammad *et al.*, "Development of Thermoelectrıc Egg Incubator Integrated wıth Thermal Energy Storage System," *J. Investig. Eng. Technol.*, vol. 4, no. 1, pp. 13–20, 2021.

[2] A. F. U Suduri, S. I. Haryudo, and M. Widyartono, "Rancang Bangun Pembangkit Listrik Tenaga Surya Kapasitas 80 WP Untuk Alat Penetas Telur Berbasis Internet of Things," *J. Tek. Elektro*, vol. 10, no. 3, pp. 587–596, Jul. 2021, doi: 10.26740/jte.v10n3.p587-596.

[3] G. Santoso, S. Hani, S. Abdullah, and Y. I. Pratama, "Pemanfaatan Pembangkit Listrik Tenaga Surya Sebagai Sumber Energi Listrik Cadangan Budidaya Burung Puyuh Dilengkapi Dengan Automatic Transfer Switch (ATS)," *J. Elektr.*, vol. 8, no. 2, pp. 45–52, 2021.

[4] H. R. Iskandar, C. B. Elysees, R. Ridwanulloh, A. Charisma, and H. Yuliana, "Analisis Performa Baterai Jenis Valve Regulated Lead Acid pada PLTS Off-grid 1 kWp," *J. Teknol.*, vol. 13, no. 2, pp. 129–140, Jul. 2021, doi: 10.24853/jurtek.13.2.129-140.

[5] A. Ridwan, A. Yanie, D. Sawitri, L. Adriana, and Y. Ananda, "Perancangan Alat Penetas Telur Unggas Dengan Energi Terbarukan Menggunakan Panel Surya," *RELE (Rekayasa Elektr. dan Energi) J. Tek. Elektro*, vol. 5, no. 2, pp. 124–128, 2023, doi: 10.30596/rele.v5i2.13090.

[6] M. Yasir, M. M, M. I. T. Ibrahim, and M. Faisal, "Uji Kinerja Alat Penetas Telur Dengan Kapasitas 30 Butir Telur Bebek," *J. Ristech (Jurnal Riset, Sains dan Teknol.*, vol. 4, no. 1, pp. 39–44, 2023.

[7] M. T. S. Isma, T. M. Purba, and J. Sinaga, "Rancang Bangun Mesin Penetas Telur Otomatis Kapasitas 50 Butir," *J. Teknol. Mesin Uda*, vol. 2, no. 2, pp. 67–75, 2021.

[8] R. Mulyadi, K. D. Artika, and M. Khalil, "Perancangan Sistem Kelistrikan Perangkat Elektronik pada Mobil Listrik," *Elem. J. Tek. Mesin*, vol. 6, no. 1, pp. 7–12, Jun. 2019, doi: 10.34128/je.v6i1.85.

[9] L. A. Gunawan, A. I. Agung, M. Widyartono, and S. I. Haryudo, "Rancang Bangun Pembangkit Listrik Tenaga Surya Portable," *J. Tek. Elektro*, vol. 10, no. 1, pp. 65–71, Aug. 2020, doi: 10.26740/jte.v10n1.p65-71.

[10] J. Firmansyah, Elvera, Febriyansyah, and R. Yudianto, "Analisis Break Even Point (BEP) Pada Usaha Penjualan Kerangka Mesin Huller Alat Pengupas Kulit Kopi Kering Bengkel Las Cahaya Abadi Kota Pagar Alam Tahun 2024," *J. Ekon. Bisnis, Manaj. dan Akunt.*, vol. 3, no. 3, pp. 839–852, Nov. 2024, doi: 10.61930/jebmak.v3i3.840.